

A Radio-selected Population of Dark, Long Gamma-ray Bursts: Comparison to the Long Gamma-ray Burst Population and Implications for Host Dust Distributions

GENEVIEVE SCHROEDER,¹ TANMOY LASKAR,² WEN-FAI FONG,¹ ANYA E. NUGENT,¹ EDO BERGER,³ RYAN CHORNOCK,⁴
KATE D. ALEXANDER,^{1,*} JENNIFER ANDREWS,⁵ R. SHANE BUSSMANN,⁶ ALBERTO J. CASTRO-TIRADO,⁷
ARMAAN V. GOYAL,⁸ CHARLES D. KILPATRICK,¹ MAURA LALLY,⁹ ADAM MILLER,¹ PETER MILNE,¹⁰ KERRY PATERSON,¹¹
ALICIA ROUCO ESCORIAL,¹ MICHAEL C. STROH,¹ GIACOMO TERRERAN,¹² AND BEVIN ASHLEY ZAUDERER¹³

¹Center for Interdisciplinary Exploration and Research in Astrophysics and Department of Physics and Astronomy, Northwestern University, 2145 Sheridan Road, Evanston, IL 60208-3112, USA

²Department of Astrophysics/IMAPP, Radboud University, PO Box 9010, 6500 GL, The Netherlands

³Center for Astrophysics | Harvard & Smithsonian, 60 Garden Street, Cambridge, MA 02138-1516, USA

⁴Department of Astronomy, University of California, Berkeley, CA 94720-3411, USA

⁵Steward Observatory, University of Arizona, 933 North Cherry Avenue, Tucson, AZ 85721-0065, USA

⁶Department of Astronomy, Space Science Building, Cornell University, Ithaca, NY 14853-6801, USA

⁷Instituto de Astrofísica de Andalucía (IAA-CSIC), Glorieta de la Astronomía s/n, E-18008, Granada, Spain

⁸Department of Astronomy, Indiana University, Bloomington, IN 47405, USA

⁹Department of Astronomy, Cornell University, Ithaca, NY 14853, USA

¹⁰University of Arizona, Steward Observatory, 933 N. Cherry Avenue, Tucson, AZ 85721, USA

¹¹Max-Planck-Institut für Astronomie (MPIA), Königstuhl 17, 69117 Heidelberg, Germany

¹²Las Cumbres Observatory, 6740 Cortona Drive, Suite 102, Goleta, CA 93117-5575, USA

¹³National Science Foundation, 2415 Eisenhower Avenue, Alexandria, Virginia 22314, USA

ABSTRACT

We present cm-band and mm-band afterglow observations of five long-duration γ -ray bursts (GRBs; GRB 130131A, 130420B, 130609A, 131229A, 140713A) with dust-obscured optical afterglow emission, known as “dark” GRBs. We detect the radio afterglow of two of the dark GRBs (GRB 130131A and 140713A), along with a tentative detection of a third (GRB 131229A) with the Karl G. Jansky Very Large Array (VLA). Supplemented by three additional VLA-detected dark GRBs from the literature, we present uniform modeling of their broadband afterglows. We derive high line-of-sight dust extinctions of $A_{V,GRB} \gtrsim 2.2 - 10.6$ mag. Additionally, we model the host galaxies of the six bursts in our sample, and derive host galaxy dust extinctions of $A_{V,Host} \approx 0.3 - 4.7$ mag. Across all tested γ -ray (fluence and duration) and afterglow properties (energy scales, geometries and circumburst densities), we find dark GRBs to be representative of more typical unobscured long GRBs, except in fluence, for which observational biases and inconsistent classification may influence the dark GRB distribution. Additionally, we find that $A_{V,GRB}$ is not related to a uniform distribution of dust throughout the host, nor to the extremely local environment of the burst, indicating that a larger scale patchy dust distribution is the cause of the high line-of-sight extinction. Since radio observations are invaluable to revealing heavily dust-obscured GRBs, we make predictions for the detection of radio emission from host star formation with the next generation VLA.

1. INTRODUCTION

Long duration γ -ray bursts (GRBs), the most luminous, energetic transients in the universe (e.g. [Racusin et al. 2008](#)), are associated with the death of massive stars ([MacFadyen & Woosley 1999](#)) and Type Ic supernovae (e.g. [Hjorth et al. 2003](#); [Woosley & Bloom 2006](#)). The relativistic shocks produced by these bursts interact with the surrounding medium, leading to the pro-

duction of broad-band synchrotron emission from radio to X-rays, known as the “afterglow”.

A subset of long GRBs have suppressed optical emission, earning them the moniker of optically “dark” GRBs, with the first documented dark GRB being GRB 970828 ([Groot et al. 1998](#)). It is estimated that $\sim 10\%$ - 50% of the long GRB population are among the dark GRB class ([Jakobsson et al. 2004](#); [Cenko et al. 2009](#); [Fynbo et al. 2009](#); [Greiner et al. 2011](#); [Melandri et al. 2012](#); [Perley et al. 2013](#)). One of the prominent causes of the darkness is attributed to dust extinction

* NASA Einstein Fellow

along the line-of-sight to the GRB, though other causes, such as intrinsically faint and rapidly fading bursts (e.g. Berger et al. 2002), or Ly α absorption from a high redshift ($z \gtrsim 6$) origin (Haislip et al. 2006; Salvaterra et al. 2009; Tanvir et al. 2009; Cucchiara et al. 2011) can also produce optically faint or undetectable afterglows. For the dust-extinguished population of dark GRBs, the amount of extinction ($A_{V,GRB}$) along the line-of-sight is of interest as it can provide insight on the amount of dust and distribution within their host galaxies (Greiner et al. 2011; Zafar et al. 2011; Krühler et al. 2011; Zauderer et al. 2013c; Perley et al. 2013). Typically, $A_{V,GRB}$ is estimated using simple power law arguments extending from the X-rays to the optical bands (e.g. Perley et al. 2013). However, the addition of a detected radio afterglow can allow for proper afterglow modeling and provide a robust measurement of $A_{V,GRB}$.

Since the first radio afterglow of a GRB was discovered in 1997 (GRB 970508, Frail et al. 1997), radio follow-up has been vital to our general understanding of GRB afterglow behavior, helping to constrain the energetics and environment of GRBs. A fairly comprehensive census of radio follow-up of 304 GRB afterglows found that only $\sim 30\%$ of GRB afterglows have radio detections (Chandra & Frail 2012). However, it was postulated that the low fraction of radio detections is likely attributed to the limited sensitivity of prior generations of radio telescopes (Chandra & Frail 2012; Osborne et al. 2021), and therefore more sensitive radio facilities could increase the fraction of detected radio afterglows of GRBs. The upgrade to the Karl G. Jansky Very Large Array (VLA), which concluded in 2012, increased the sensitivity of the radio array by a factor of ~ 10 (Perley et al. 2011), and has allowed for well-sampled, multi-band, follow-up of long GRB radio afterglows (including, but not limited to: Chandra & Frail 2012; Laskar et al. 2013c; Zauderer et al. 2013c; Laskar et al. 2014, 2015, 2016; Alexander et al. 2017; Laskar et al. 2018a,b,c). Radio observations of dust obscured dark GRBs are critical for properly modeling the afterglow of these bursts, especially when the optical afterglow is not detected (e.g. Jakobsson et al. 2005; Castro-Tirado et al. 2007; Rol et al. 2007; Zauderer et al. 2013c; van der Horst et al. 2015; Higgins et al. 2019; Kangas & Fruchter 2021), as the low-frequency afterglow can constrain burst energetics and environment density through determination of the synchrotron break frequencies (e.g. Sari et al. 1998; Granot & Sari 2002).

In addition to the properties of the afterglow of dark GRBs, there has been much interest in the host galaxies of dark GRBs and how they compare to the typical long GRB population (e.g. Krühler et al. 2011; Perley

et al. 2013). The *Swift* X-ray Telescope (*Swift*/XRT) typically provides afterglow positions of $\sim 2''$ (Evans et al. 2009), while the detection of a radio afterglow with the VLA can often provide unambiguous association to a host galaxy via sub-arcsecond precision, especially in the case of optically-faint or non-detected dark GRBs (e.g. Zauderer et al. 2013c). Previous studies based on small numbers have found that the hosts of dust-obscured bursts are overall more massive, more luminous, more star forming, and dustier than other long GRB hosts (i.e. Krühler et al. 2011; Perley et al. 2013). Long GRBs in general are already associated with star forming galaxies (i.e. Djorgovski et al. 1998; Christensen et al. 2004; Japelj et al. 2016; Palmerio et al. 2019), and the obscuration of dark GRBs may point to obscured star formation in their hosts (Blain & Natarajan 2000; Ramirez-Ruiz et al. 2002).

Here, we present the multi-wavelength observations for five dark GRBs, including VLA observations for all five bursts. We present the discovery of the VLA radio afterglow for one burst (GRB 130131A), present a nominal VLA radio detection for another burst (GRB 131229A), present new radio and millimeter detections for an additional event (GRB 140713A), and new upper limits for two events. For our three VLA detected/nominally detected dark GRBs, we uniformly model the afterglows and host galaxies, and include uniform models of the afterglow and host galaxies of three VLA detected dark bursts from the literature. We proceed to compare the afterglow and host properties of dark GRBs to the larger population of typical long GRBs that have not been classified as dark. In Section 2 we describe our sample and our criteria for classifying GRBs as dark. In Section 3 we describe our methods for self-consistent modeling of all available broadband afterglow data and we apply our afterglow modeling to the relevant bursts in our sample to extract their local environment, burst energetics and microphysical parameters. In Section 4 we present host galaxy modeling for the bursts with robust host galaxy associations and spectroscopic or photometric data. In Section 5 we compare our dark GRB sample to the broader population of long GRBs in terms of their γ -ray, afterglow, and host properties, and consider the detectability of obscured star formation in long GRB host galaxies. We conclude in Section 6. We present the details of the multi-wavelength observations and data reduction in Appendix A. In this paper, we employ the Λ CDM cosmological parameters of $H_0 = 68 \text{ km s}^{-1} \text{ Mpc}^{-1}$, $\Omega_M = 0.31$, $\Omega_\Lambda = 0.69$.

2. SAMPLE SELECTION AND CLASSIFICATION METHOD

Our primary goal is to uniformly model the afterglows and host galaxies of dark GRBs. We focus on dark GRBs with VLA observations taken after the upgrade (Perley et al. 2011), specifically those taken with our Programs 13A-046, 13A-541, and 14A-344 (PI: Berger)¹. This sample includes five dark GRBs, two of which have unambiguous radio afterglow detections, and one of which has a tentative radio afterglow detection. We supplement this sample with three other dark GRBs with VLA detections, GRB 110709B (Zauderer et al. 2013c), 111215A (Zauderer et al. 2013c; van der Horst et al. 2015)², and GRB 160509A (Laskar et al. 2016, classifying this latter burst as dark for the first time in Section A.6.3). As 14 dark GRBs have been observed by the VLA since its upgrade (Zauderer & Berger 2012; Zauderer et al. 2013c; Laskar et al. 2013a; Veres et al. 2015; Horesh et al. 2015; Laskar et al. 2016, the VLA Data Archive, This Work), our sample of 8 comprises over half of the known dark GRBs with upgraded VLA observations. The eight 8 dark GRBs featured in this paper are listed in Table 1.

Standard measures of classifying long GRBs as “dark” in the standard synchrotron model (Granot & Sari 2002 and Section 3), involve the optical-to-X-ray spectral index β_{OX} and the X-ray spectral index β_{X} . One such method of classification uses the expected spectral index between the optical and X-ray afterglow fluxes of $-p/2 < \beta_{\text{OX}} < (1-p)/2$, where p is the power-law index of the electron energy distribution, $F_{\nu} \propto \nu^{\beta}$, and the spectral index is dependent on the location of the cooling frequency (ν_c) in relation the optical and X-ray bands. As $p > 2$ is typically expected (e.g. Sari et al. 1998), the shallowest expected $\beta_{\text{OX}} = -0.5$, where $p = 2$. Therefore, if $\beta_{\text{OX}} > -0.5$, then the shallow spectral slope indicates the optical afterglow has been suppressed and the burst can be considered dark (Jakobsson et al. 2004). An alternate definition of afterglow darkness is $\beta_{\text{OX}} > \beta_{\text{X}} + 0.5$, corresponding to an optical flux that is even lower than the shallowest possible extrapolation from the X-rays, $\nu_c \approx \nu_{\text{X}}$, in the synchrotron framework (van der Horst et al. 2009). For the purposes of this paper, we will consider any burst “dark” if they meet the Jakobsson et al. (2004) criterion of $\beta_{\text{OX}} > -0.5$, though

we will note whether the bursts in our sample meet the van der Horst et al. (2009) classification criterion as well.

To determine β_{OX} , we interpolate the X-ray light curve to the times of the optical observations, using least squares fits to the X-ray light curves to calculate the X-ray temporal index α_{X} (where $F_{\nu} \propto t^{\alpha}$), and calculate β_{OX} , correcting the optical observations for Galactic extinction in the direction of the burst (Schlafly & Finkbeiner 2011). To determine β_{X} , we create time-sliced spectra from the *Swift* tool³, which calculates the photon index, Γ_{X} (Evans et al. 2009), from which we derive $\beta_{\text{X}} \equiv 1 - \Gamma_{\text{X}}$. On a per-burst basis, we exclude any times over which the X-ray light curve exhibits flaring activity super-imposed on the power-law afterglow, as this emission is not likely to originate from the external shock (Burrows et al. 2007; Margutti et al. 2010).

The full details of the X-ray, optical, near-infrared (NIR) and radio observations of the GRB afterglows and host galaxies, as well as their classifications as dark GRBs are presented in Appendix A. We show the fields and afterglow localizations of six dark GRBs in our sample in Figure 1, and their afterglow detectabilities, as well as whether we model their afterglows and host galaxies, are summarized in Table 1.

3. AFTERGLOW MODELING

We will consider the X-ray, optical, and radio afterglow light curves and spectral energy distributions (SEDs) of the GRBs in our sample in the context of synchrotron emission from the acceleration of electrons from a relativistic blast wave (i.e. Sari et al. 1998; Chevalier & Li 2000; Panaitescu & Kumar 2000; Granot & Sari 2002). These electrons are accelerated to a non-thermal power law distribution, $N(\gamma_e) \propto \gamma_e^{-p}$. The afterglow SEDs can be described by power law segments which connect at three break frequencies (the self absorption frequency, ν_a , the characteristic frequency, ν_m , and the cooling frequency, ν_c) and the characteristic flux, $F_{\nu,m}$ (Granot & Sari 2002). The SED and light curve temporal evolution are dependent on the following parameters: p , the isotropic-equivalent kinetic energy of the burst, $E_{K,\text{iso}}$, the density of the environment⁴, $\rho = Ar^{-k}$, and the fractional energy density imparted on the electrons, ϵ_e , and the magnetic field, ϵ_B .

¹ We exclude GRB 130606A as the darkness of this burst is likely attributed to its high redshift of $z \approx 5.91$ (Castro-Tirado et al. 2013; Chornock et al. 2013a; Littlejohns et al. 2015)

² While the upgrade to the VLA completed at the end of 2012, the C-band (4-8 GHz) and K-band (18-26.5 GHz) receivers were upgraded by 2011 (Perley et al. 2011). As the majority of the VLA observations of GRB 110709B and GRB 111215A were taken with these upgraded receivers, we include these bursts in our sample.

³ https://www.swift.ac.uk/user_objects/docs.php#specform

⁴ In a constant density interstellar medium (ISM) environment, $k = 0$ and $A = n_0 m_p$. In a wind environment, $k = 2$, $A = 5 \times 10^{11} \text{ gm cm}^{-1} A_*$, normalized to a progenitor mass-loss rate of $A_* = 10^{-5} M_{\odot} \text{ yr}^{-1}$ and wind velocity of 1000 km s^{-1} ; (Chevalier & Li 2000).

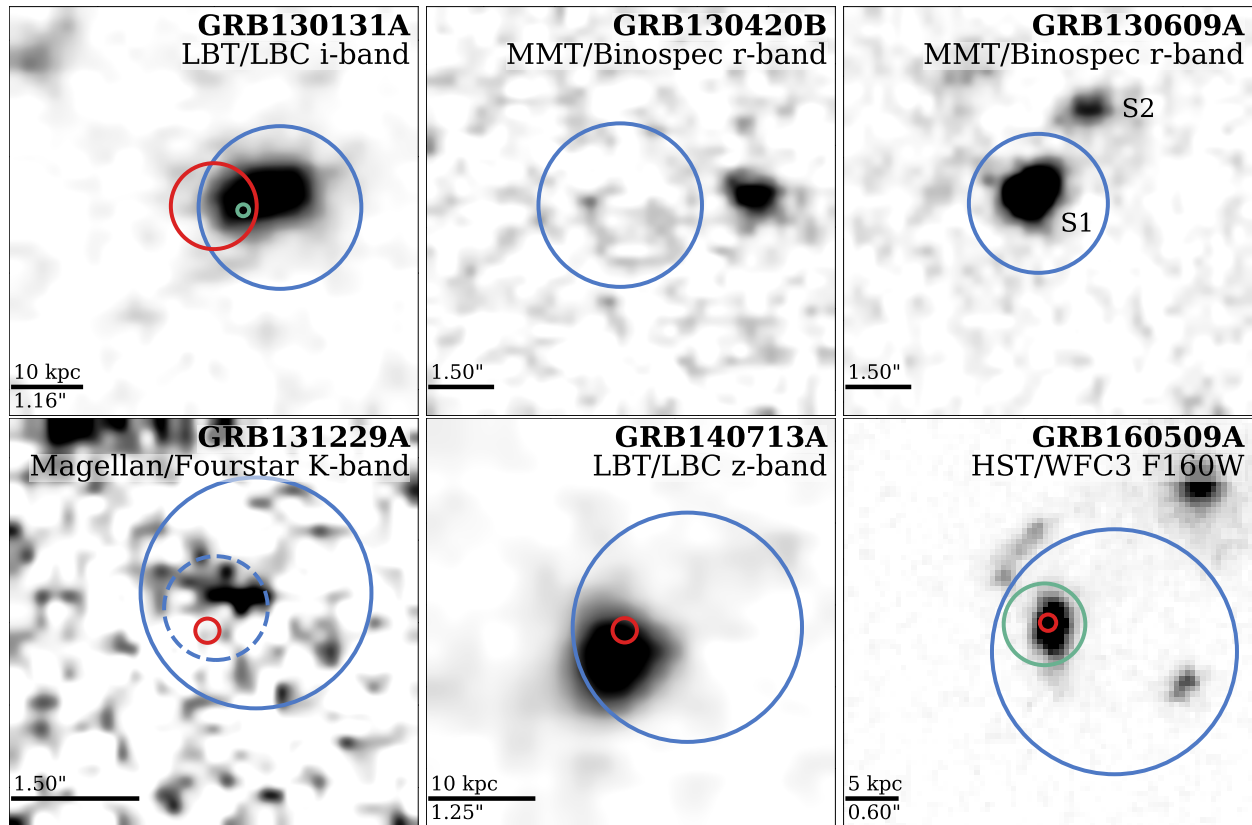


Figure 1. Deep optical or NIR observations of the fields of GRBs 130131A, 130420B, 130609A, 131229A, 140713A, and 160509A. In each panel, the blue solid-line circle indicates the XRT afterglow location (90% confidence). When available, the red circle indicates the radio afterglow location (1σ), the green circle denotes the optical or NIR position (1σ), and the dashed blue circle indicates the *CXO* position. Images have been smoothed with a 3-pixel Gaussian, and the orientation is North up and East to the left. An angular scale is provided in all images, in addition to a physical scale when the redshift is known. For GRBs 130420B and 130609A, we do not identify host galaxies.

In addition to the standard synchrotron frame work laid out in [Granot & Sari \(2002\)](#), we also consider the effects of beaming on the GRB afterglow light curves. Collimation is expected to manifest itself as a jet break, which occurs when the angular size of the relativistic beam of the GRB jet approaches the value of the true opening angle of the jet (θ_{jet}). At the time that this jet break occurs, t_{jet} , the observed light curve is predicted to steepen achromatically ([Rhoads 1999](#); [Sari et al. 1999](#)). Determining t_{jet} from a GRB afterglow can therefore provide us with the opening angle of the jet, which allows for the correction of the energetics for beaming and in turn, we can derive the true kinetic (E_K), γ -ray (E_γ), and total energies of the burst ($E_{\text{tot}} = E_K + E_\gamma$). Additionally, the evolution of the afterglow light curves at $\delta t > t_{\text{jet}}$ (where δt is the time after the *Swift*/Burst Alert Telescope trigger) is $F_\nu \propto t^{-p}$ when $\nu_{\text{obs}} \geq \nu_m$ ([Sari et al. 1999](#)), where ν_{obs} is the observing frequency. Thus, identifying a jet break in the afterglow and measuring the post-break light curve slope provides an additional constraint on the value of p .

To properly model the X-ray afterglow, we include the effects of inverse Compton (IC) cooling in our model, which can lower the location of ν_c (in comparison to the value predicted by a spherical blast-wave without IC cooling, e.g., [Granot & Sari 2002](#)) by a factor of $(1+Y)^2$, where Y is the Compton Y -parameter (for the detailed explanation see: [Sari & Esin 2001](#); [Laskar et al. 2015](#)).

Prior to performing a full fit to the broad-band data, we first examine the SEDs and light curves of our afterglow observations and fit them using either a single power law function or a smoothly broken power law, given by

$$F_\nu(t) = F_b \left[\frac{1}{2} \left(\frac{t}{t_b} \right)^{-s\alpha_1} + \frac{1}{2} \left(\frac{t}{t_b} \right)^{-s\alpha_2} \right]^{-1/s}, \quad (1)$$

$$F_\nu(\nu) = F_b \left[\frac{1}{2} \left(\frac{\nu}{\nu_b} \right)^{-s\beta_1} + \frac{1}{2} \left(\frac{\nu}{\nu_b} \right)^{-s\beta_2} \right]^{-1/s} \quad (2)$$

where F_b is the normalized flux of the break, ν_b and t_b are the break frequency and time, respectively, s is

Table 1. Observation Summary

GRB	Opt and/or NIR/Radio ^a	Modeled ^b	References
110709B	N/Y	Y	1, 2, 3
111215A	N/Y	Y	1, 4, 5
130131A	Y/Y	Y	5, 6
130420B	N/N	N	6
130609A	N/N	N	6
131229A	N/Y ^c	Y ^d	5, 6
140713A	N/Y	Y	6, 7
160509A	Y/Y	Y ^e	6, 8, 9

NOTE— ^a Whether or not the afterglow was detected in the optical/NIR or radio.

^b Whether or not we model the afterglow and host galaxy of the burst in this paper

^c We find a tentative 6.0 GHz detection for GRB 131229A (see Section A.4.2)

^d Due to the limited radio data, we present a simple analytical afterglow model for GRB 131229A in Section 3.4, and analytically derive afterglow properties. We model the host galaxy of GRB 131229A in this work.

^e The X-ray to radio afterglow of GRB 160509A was modeled within our modeling framework in Laskar et al. (2016). We model the host galaxy of GRB 160509A in this work.

References. (1) Zauderer et al. (2013c); (2) Perley et al. (2016a); (3) Selsing et al. (2019); (4) van der Horst et al. (2015); (5) Chrimes et al. (2019); (6) This Work; (7) Higgins et al. (2019); (8) Laskar et al. (2016); (9) Kangas et al. (2020)

the break smoothness⁵, and α_1 , α_2 and β_1 , β_2 are the temporal or spectral slopes of the fits, respectively. We use the convention $F_\nu \propto t^\alpha \nu^\beta$ throughout. Where data quality allows, we use Equation 1 for light curves and Equation 2 for SEDs. When necessary, we use temporal power law fits to interpolate the flux to common times for our SED fitting.

We use these basic broken power law considerations to place initial constraints on p , t_{jet} , the nature of the burst environment (i.e. ISM vs. wind), and the location of the break frequencies with respect to our observing bands, when possible. We then model the GRB with the Markov Chain Monte Carlo (MCMC) modeling framework laid out in Laskar et al. (2014), including IC effects. We also take into consideration the scattering effects of scintillation, which may cause variability

⁵ Larger values of s correspond to sharper breaks.

on short timescales at GHz frequencies (Rickett 1990). In the situations for which the burst environment cannot be constrained with initial considerations alone, we model the GRB afterglow with both an ISM and wind environment and choose the model that provides a better statistical fit.

To account for any potential systematic uncertainties in flux calibration for data taken across different facilities, we include an uncertainty floor of 10% on individual measurements prior to modeling. The free parameters for our model are p , $E_{K,\text{iso}}$, n_0 in an ISM environment or A_* for a wind environment, ϵ_e , ϵ_B , and t_{jet} . We fit each GRB with available broad-band afterglow data with the MCMC model, using 128 walkers for 10,000 steps, and discard the first $\sim 1\%$ of steps as “burn in”, where the average likelihood across the chains have yet to reach a stable value.

3.1. GRB 110709B

We compile all available radio data of GRB 110709B, along with optical upper limits and the *Swift* X-ray light curve (Section A.6.1), to model the afterglow. The data consists of a VLA 5.8 GHz light curve spanning $\delta t \approx 2.1 - 69.7$ days, a VLA 21.8 GHz upper limit at $\delta t \approx 12.1$ days, GROND optical/NIR ($g'r'i'z'JHK_s$) non-detections at $\delta t \approx 0.11$ days, and the *Swift* X-ray afterglow light curve spanning $\delta t \approx 10^{-3} - 10^2$ days.

The afterglow of GRB 110709B was previously modeled by Zauderer et al. (2013c), and then by Kangas & Fruchter (2021). Zauderer et al. (2013c) did not include IC effects in their modeling, while Kangas & Fruchter (2021) did include IC effects, though they did not fit for $A_{V,\text{GRB}}$, which is a key parameter of interest for our study. Here, we model GRB 110709B to ensure consistency across our sample and to determine $A_{V,\text{GRB}}$.

3.1.1. Basic Considerations

The X-ray afterglow light curve exhibits flaring activity until $\delta t \approx 0.02$ days, and we only consider these data over $\delta t \approx 0.06 - 116$ days for our modeling. We created a time-sliced spectra from the *Swift* online tool for the photon counting (PC) mode X-ray light curve, which found $\Gamma_X = 2.06_{-0.03}^{+0.04}$ (1σ , Evans et al. 2009), corresponding to $\beta_X = -1.06_{-0.03}^{+0.04}$. We fit the X-ray light curve with a broken power law (Section 3; Eq 1) characterized by $\alpha_{X,1} = -0.78 \pm 0.05$ ($\alpha_{X,1} = -0.86 \pm 0.03$) and $\alpha_{X,2} = -1.70 \pm 0.06$ ($\alpha_{X,2} = -1.58 \pm 0.04$), with the break occurring at $\delta t \approx 0.7$ days ($\delta t \approx 0.6$ days) for $s = 2$ ($s = 8$).

We first investigate the nature of the steepening in the X-ray light curve of GRB 110709B. Such steepenings are often explained by either the passage of ν_c through the band, or a jet break. For the passage of ν_c at $\delta t \approx$

Table 2. Forward Shock Parameters

GRB	110709B	111215A	130131A	131229A ^a	140713A
Env.	ISM	Wind	Wind	ISM	Wind
p	2.03 2.04 ^{+0.02} _{-0.02}	2.88 2.82 ^{+0.04} _{-0.06}	2.30 2.39 ^{+0.09} _{-0.07}	– 2.46 ^{+0.03} _{-0.03}	2.17 2.17 ^{+0.04} _{-0.03}
E_K (10^{52} erg)	1.69×10^{-1} $9.63^{+6.32}_{-4.5} \times 10^{-2}$	6.63×10^{-1} $4.99^{+0.94}_{-1.01} \times 10^{-1}$	2.25×10^{-3} $3.24^{+3.04}_{-1.26} \times 10^{-3}$	– –	6.99×10^{-3} $7.71^{+1.63}_{-1.06} \times 10^{-3}$
A_*/n_0 ($-\text{cm}^{-3}$)	3.85×10^{-3} $2.24^{+3.03}_{-1.28} \times 10^{-3}$	1.88×10^{-1} $1.55^{+0.19}_{-0.22} \times 10^{-1}$	4.0×10^{-2} $4.22^{+2.24}_{-1.22} \times 10^{-2}$	– $\gtrsim 1.72 \times 10^{-5} \epsilon_B^{-5/3}$	6.25×10^{-1} $7.33^{+2.09}_{-1.18} \times 10^{-1}$
ϵ_e	6.90×10^{-1} $3.77^{+3.12}_{-1.74} \times 10^{-1}$	1.04×10^{-1} $9.47^{+0.59}_{-0.65} \times 10^{-2}$	8.74×10^{-1} $7.75^{+1.23}_{-1.59} \times 10^{-1}$	– $\gtrsim 1.19 \times 10^{-2} \epsilon_B^{-1/3}$	7.24×10^{-1} $6.78^{+0.88}_{-0.89} \times 10^{-1}$
ϵ_B	1.26×10^{-3} $5.12^{+29.24}_{-3.91} \times 10^{-3}$	2.97×10^{-3} $6.11^{+4.81}_{-2.08} \times 10^{-3}$	1.25×10^{-1} $9.53^{+13.85}_{-6.98} \times 10^{-2}$	– –	2.76×10^{-1} $2.79^{+0.92}_{-0.85} \times 10^{-1}$
t_{jet} (day)	1.38 $1.39^{+0.11}_{-0.10}$	26.09 $25.36^{+4.04}_{-3.27}$	3.49 $4.89^{+8.04}_{-2.35}$	– $\gtrsim 1.3$	3.61 $3.4^{+0.52}_{-0.42}$
θ_{jet} (deg)	1.65 $1.68^{+0.22}_{-0.19}$	2.60 $2.68^{+0.13}_{-0.12}$	8.17 $8.46^{+2.39}_{-1.36}$	– $\gtrsim 1.32 \epsilon_B^{-1/4}$	21.27 $21.46^{+1.24}_{-1.07}$
$A_{V,\text{GRB}}$ (mag)	$\gtrsim 3.9$ $\gtrsim 3.8^b$	$\gtrsim 10.6$ $\gtrsim 10.6^b$	≈ 2.2 $2.3^{+0.1}_{-0.1}$	– $\gtrsim 9.6$	$\gtrsim 3.5$ $\gtrsim 3.5^b$

NOTE— The top row for each parameter corresponds to the best fit forward shock value from our MCMC modeling. The bottom row for each parameter corresponds to the summary statistics from the marginalized posterior density functions (medians and 68% credible intervals), except in the case of GRB 131229A (see ^a)

^a Values derived from analytical arguments (see Section 3.4)

^b $A_{V,\text{GRB}}$ value from afterglow model using median values

0.6 days, the expected change in temporal index is $\Delta\alpha = 0.25$, which is too shallow to explain the observed $\Delta\alpha \approx 0.7 - 0.9$. Thus, we attribute the steepening instead to a jet break.

We now use the X-ray spectral index and pre-break light curve to determine where ν_X lies in relation to ν_c . If $\nu_m < \nu_X < \nu_c$, the X-ray spectral index implies $p = 3.12 \pm 0.07$. However, we find that the measured value of $\alpha_{X,1}$ yields $p = 1.49 \pm 0.04$ in a wind environment or $p = 2.16 \pm 0.04$ in an ISM environment, neither of which are consistent with the value derived from β_X . On the other hand, for $\nu_m, \nu_c < \nu_X$, we require $p = 2.12 \pm 0.07$ to match the X-ray spectral index and $p = 1.82 \pm 0.04$ (in both the wind and ISM environment) to match the light curve. The values of p are in agreement to within 3σ , and we therefore conclude that $\nu_m, \nu_c < \nu_X$ and $p \approx 1.8 - 2.1$. In this regime, the X-ray observations cannot be used to discriminate between an ISM and wind environment.

The expected temporal decay after a jet break is $\alpha = -p$, and our post-break X-ray light curve slope of $-1.7 \lesssim \alpha_{X,2} \lesssim -1.6$ is shallower than the expected $-2.1 \lesssim \alpha \lesssim -1.8$. However, the break time and slope are degenerate with the smoothness of the break, and a later break time is consistent with a steeper post break decline. This suggests that the break in the X-ray light curve is due to a jet break, whose onset occurs at $\delta t \gtrsim 0.6$ days. Additionally, if $t_{\text{jet}} \approx 0.6$ days, then the 5.8 GHz light curve, which does not have any observations prior to t_{jet} , cannot be used to distinguish between the ISM and wind environment, as the behavior of the synchrotron model is the same regardless of environment after t_{jet} .

In conclusion, the X-ray afterglow of GRB 110709B is consistent with $\nu_m, \nu_c < \nu_X$, $p \approx 1.8 - 2.1$, and $t_{\text{jet}} \gtrsim 0.6$ days. Additionally, the X-ray and radio light curves cannot be used to distinguish between the ISM and wind environment.

3.1.2. MCMC Modeling

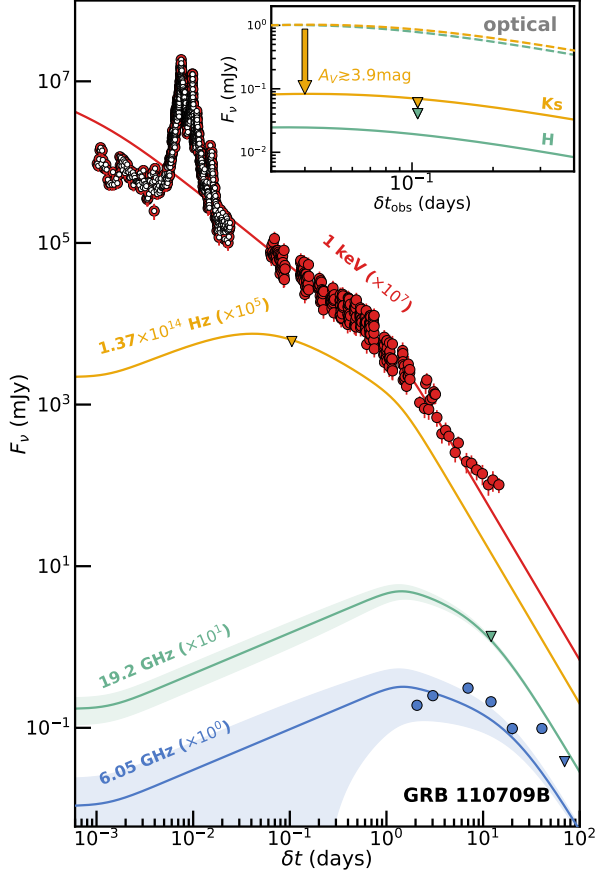


Figure 2. X-ray, optical, and radio afterglow light curves of GRB 110709B, together with the best-fit forward shock model in an ISM environment (lines). Circles represent detections, and triangles represent 3σ upper limits (Zauderer et al. 2013c). Open symbols indicate data that are not included in the fit, and shaded regions represent variability due to scintillation. The inset shows the model K_s -band and H -band light curves (solid lines) as well as the non-extinguished models (dashed lines), with $A_{V,GRB} \gtrsim 3.9$ mag necessary to be consistent with the upper limits.

As we can not distinguish between the wind and ISM environments using preliminary analytical arguments, we therefore fit the GRB 110709B afterglow data with both a wind and ISM environment, and choose the solution that provides a better statistical fit.

We find the ISM environment model is marginally preferred by the data, with $\chi^2/\text{d.o.f.} \approx 386/1289$ and likelihood (L) of ≈ 2092 , compared to the wind environment best fit model with $\chi^2/\text{d.o.f.} \approx 434/1289$ and a lower L of ≈ 2063 (see Appendix B.1 for wind model, provided for completeness). We present the best-fit (highest likelihood) ISM model in Figure 2 and list the parameters as well as the summary statistics from the marginalized posterior density functions (medians and 68% credible intervals) in Table 2.

We find that $p \approx 2.02$ and $t_{\text{jet}} \approx 1.4$ days (consistent with the arguments laid out in Section 3.1.1), resulting in $\theta_{\text{jet}} \approx 1.4^\circ$. The SED remains in the slow cooling phase with a break frequency ordering of $\nu_{\text{sa}} < \nu_{\text{m}} < \nu_{\text{c}}$ for the entirety of the afterglow observations considered. Our fit also confirms that $\nu_{\text{c}} < \nu_{\text{X}}$, as expected. For our best fit ISM model, the GROND optical/NIR limits imply $A_{V,GRB} \gtrsim 3.94$ mag.

We comment here on a few notable discrepancies between the data and model light curves. The 5.8 GHz model light curve under-predicts the last detection at $\delta t \approx 40$ days by $\approx 11.6\sigma$. This discrepancy is too large to be reconciled with scintillation effects alone. Moreover, the X-ray model light curve under-predicts the data at $\delta t \gtrsim 7.6$ days. This result is not unexpected, as we measure a shallower temporal index in the post-break X-ray light curve than would be expected for post jet-break behavior (see Section 3.1.1), and therefore we find an excess within our model. We first consider whether this excess flux in the X-ray afterglow is due to Klein Nishina (KN) effects. KN effects become important when $\hat{\nu}_m \leq \nu_{\text{obs}}$ (typically the ν_{obs} is the X-ray frequency), where $\hat{\nu}_m = \nu_m(\hat{\gamma}_m)$, and $\hat{\gamma}_m$ is the critical Lorentz factor (Nakar et al. 2009). Given our best fit parameters, we find that at $\delta t \approx 12.6$ days, $\nu_{\text{X}} \ll \hat{\nu}_m \approx 1.6 \times 10^{25}$ Hz. Therefore, we conclude that KN effects are not causing the excess flux in the X-ray afterglow. We next consider whether IC emission is the cause of the observed X-ray excess. We calculate the flux of the IC spectra at $\delta t \approx 12.6$ days and find that the IC flux at ν_{X} is $\approx 3.8 \times 10^{-10}$ mJy, which is a factor $\approx 10^4$ times lower than the X-ray flux at that time. Therefore, we also conclude that IC effects are not contributing to the excess flux.

Instead, the discrepancy between the X-ray and 5.8 GHz model light curves and observations could be reconciled with a slightly later jet break at $\delta t \approx 2.0$ days. However, this would violate the 22 GHz upper limit at $\delta t \approx 12.1$ days. In summary, there is not a natural explanation for the late-time excess emission in these bands, although fixing the time of the jet break to be later does not significantly affect the parameters of interest (E_{K} , n_0 , and $A_{V,GRB}$), and they remain consistent with the fit presented above within errors.

Both Zauderer et al. (2013c) and Kangas & Fruchter (2021) found the wind environment to best fit the afterglow of GRB 110709B, whereas we found the ISM environment to best fit the afterglow of GRB 110709B. The discussion of our wind environment model fit and comparison to the fits of Zauderer et al. (2013c) and Kangas & Fruchter (2021) can be found in Appendix B.1.

3.2. GRB 111215A

We compiled the radio and millimeter light curves of the afterglow of GRB 111215A, along with NIR/optical upper limits and the *Swift* X-ray light curve for our afterglow modeling (Section A.6.2). The radio afterglow of GRB 111215A is one of the best sampled of any dark GRB, with 1.4 GHz non-detections spanning $\delta t \approx 10 - 237$ days, 4.8, 4.9, and 6.7 GHz observations spanning $\delta t \approx 1.4 - 238$ days (all together C-band), 8.5 GHz observations spanning $\delta t \approx 15 - 88$ days (X-band), 15 GHz observations spanning $\delta t \approx 34 - 79$ days, 19.1 and 24.5 GHz observations spanning $\delta t \approx 3 - 88$ days (all together K-band), 86.7, 93, 93.7, and 94.5 GHz observations spanning $\delta t \approx 1 - 74$ days (all together 3mm), 104.7 GHz detection at $\delta t \approx 2.7$ days, and a 230 GHz upper limit at $\delta t \approx 17$ days. The deepest optical and NIR upperlimits of GRB 111215A span $\delta t \approx 0.2 - 0.3$ days. The *Swift* X-ray afterglow of GRB 111215A spans $\delta t \approx 4.9 \times 10^{-3} - 16.7$ days.

GRB 111215A has previously been modeled by Zauderer et al. (2013c) and van der Horst et al. (2015), though neither of them included IC effects. Additionally, Kangas & Fruchter (2021) modeled GRB 111215A with the inclusion of IC effects, but they chose not to fit for $A_{V,GRB}$. Like for GRB 110709B, we choose to model GRB 111215A in our modeling framework both for consistency across our sample, and to determine $A_{V,GRB}$.

3.2.1. Basic Considerations

We first consider the radio and millimeter light curves of GRB 111215A to determine the location of the radio observations in relation to ν_{sa} and ν_m . At $\delta t \approx 8.0$ days and $\delta t \approx 10.4$ days, the spectral index between the C-band and 3mm afterglow is $\beta \approx 0.37 - 0.39$, suggesting the spectral ordering of $\nu_{sa} < \text{C-band} < 3\text{mm} < \nu_m$ (expected $\beta = 1/3$). The 3mm light curve over $\delta t \approx 8.5 - 12.0$ days is roughly constant, with $F_{\nu,3\text{mm}} \approx 1.4$ mJy, implying the burst occurred in a wind environment (expected $\alpha = 0$). We find the same conclusion from the C-band light curve, where from $\delta t \approx 6.1 - 10.1$ days the afterglow flux matches $F_\nu \propto t^0$. Thus the radio and millimeter afterglow of GRB 111215A is consistent with a wind environment, and indicates $\nu_{sa} < \text{C-band} < 3\text{mm} < \nu_m$ at least from $\delta t \approx 8.0 - 12$ days.

We now turn our attention to an interesting spectral phenomena in our radio and millimeter afterglow observations. As discussed, the spectrum between C-band and 3mm at $\delta t \approx 8.0$ and 10.4 days indicates that $\nu_{sa} < \text{C-band} < 3\text{mm} < \nu_m$ in a wind environment. This conclusion appears to still hold true for the spectrum at $\delta t \approx 45.25$ days ($\beta \approx 0.12$), as the passage of ν_m through the millimeter and radio would result in a negative spec-

tral slope. However, between $\delta t \approx 11.8 - 26.5$ days, an additional bump in the spectrum peaking between X-band and K-band is inconsistent with the expected $\beta = 1/3$ (Figure 3). A possible explanation for this spectral feature is a reverse shock. However, the exploration of this possibility is outside the scope of this work.

We now consider the X-ray spectrum and light curve to determine the location of ν_c and p . The X-ray afterglow of GRB 111215A exhibits flaring until $\delta t \approx 0.02$ days (Figure 3). Thus, we only consider the X-ray afterglow for $\delta t \approx 0.02 - 16.7$ days, where we generate a PC-mode time-sliced spectra from the *Swift* online tool, which found $\Gamma_X = 2.11 \pm 0.06$ (1σ , Evans et al. 2009). The X-ray afterglow of GRB 111215A is characterized by a spectral index $\beta_X = -1.11 \pm 0.06$ and can be fit with a single temporal power law characterized by $\alpha_X = -1.43 \pm 0.02$ (Figure 3).

In a wind environment, the scenario of $\nu_m < \nu_X < \nu_c$ β_X implies $p = 3.22^{+0.12}_{-0.11}$, which is inconsistent with the α_X derived value of $p = 2.25 \pm 0.03$, and we therefore rule out this spectral frequency ordering. However, in the case of $\nu_m, \nu_c < \nu_X$, we require $p = 2.22 \pm 0.12$ to match the measured value of β_X , which is consistent within 3σ to the α_X derived value of $p = 2.58 \pm 0.03$. Therefore, we conclude that $\nu_m, \nu_c < \nu_X$ and $p \approx 2.2 - 2.6$. Moreover, the X-ray light curve does not exhibit any break to $\delta t \approx 17$ days, placing a lower limit on the time of the jet break to $t_{\text{jet}} \gtrsim 17$ days (Figure 3).

In conclusion, the radio afterglow of GRB 111215A is consistent with a wind environment where $\nu_{sa} < \text{C-band} < 3\text{mm} < \nu_m$. Additionally, the X-ray afterglow is consistent with $\nu_m, \nu_c < \nu_X$. We find a preliminary estimate of $p \approx 2.2 - 2.6$, and expect $t_{\text{jet}} \gtrsim 17$ days.

3.2.2. MCMC Modeling

We fit the afterglow data of GRB 111215A with a wind environment. We present the best fit parameters wind model in Figure 3 and list the parameters as well as the summary statistics from the marginalized posterior density functions (medians and 68% credible intervals) in Table 2.

For our best fit wind model, the optical/NIR limits imply $A_{V,GRB} \gtrsim 10.6$ mag. Our model parameters are $p \approx 2.88$ and $t_{\text{jet}} \approx 26.0$ days, resulting in a $\theta_{\text{jet}} \approx 2.6^\circ$. The value of p is higher than our initial prediction of $p \approx 2.2 - 2.6$ (see Section 3.2.1). We can reconcile the higher value of p found in the full modeling compared to the simplistic calculations performed earlier by investigating the IC cooling effects for our best fit parameters. We find that the Compton Y -parameter decreases from $Y \approx 6.4$ at the time of the fast-to-slow cooling transition

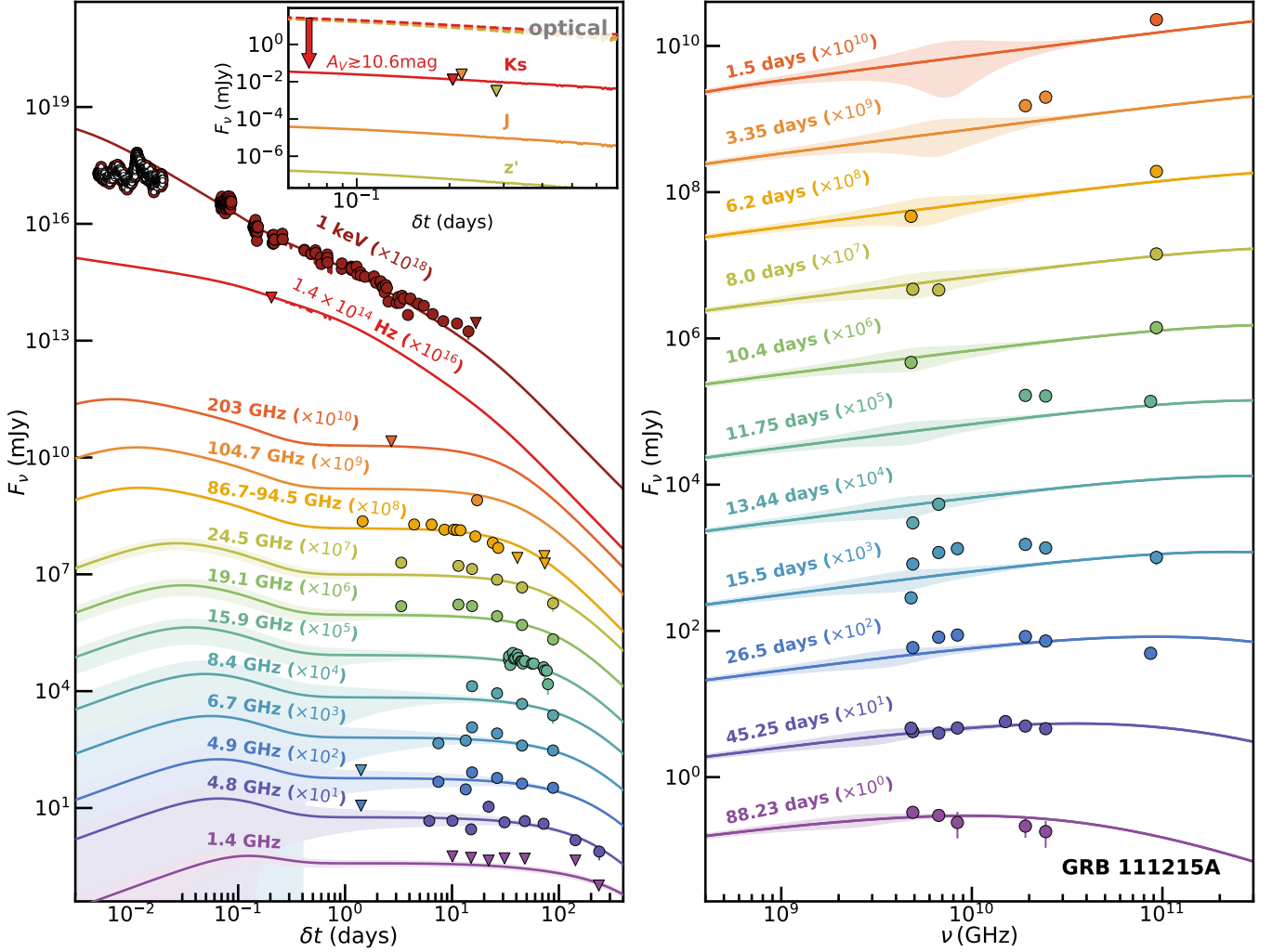


Figure 3. *Left:* X-ray, optical, millimeter and radio afterglow light curves of GRB 11215A, together with the best-fit forward shock model in a wind environment (lines). Circles represent literature data (Zauderer et al. 2013c; van der Horst et al. 2015), and triangles represent 3σ upper limits. Open symbols indicate data that are not included in the fit, and shaded regions represent variability due to scintillation. The inset shows the model z' -, J -, and Ks -band light curves (solid lines) as well as the non-extinguished models (dashed lines), indicating $A_{V,GRB} \gtrsim 10.6$ mag to explain the upper limits. *Right:* Radio and millimeter spectral energy distributions (SEDs) of the afterglow of GRB 11215A from $\delta t \approx 1.5$ –88.23 days, together with the best-fit forward shock model (lines). Overall the model provides a good match to the broad-band temporal and spectral evolution of the afterglow.

($\delta t \approx 0.2$ days) to $Y \approx 0.7$ at the time of the last X-ray detection ($\delta t \approx 14.3$ days). This decrease in Y results in a faster evolution of ν_c , and results in a shallower light curve at higher p .

Consistent with the likely existence of an additional component (Section 3.2.1), our FS model under-predicts the light curves of the X- and K-band afterglow at $\delta t \lesssim 45$ days, as well as the 3mm light curve at $\delta t \lesssim 8.0$ days.

Similar to the work presented here, Kangas & Fruchter (2021) modeled GRB 11215A in a wind environment with IC effects included, finding similar parameter values to us, though our model most disagrees with Kangas & Fruchter (2021) on the placement of t_{jet} , where they

found $t_{jet} \approx 10.8$ days, driven mainly by the fit to the early data.

3.3. GRB 130131A

We compiled the radio light curves (6.0 GHz, 19.2 GHz, and 24.5 GHz, spanning $\delta t \approx 0.7$ –13.9 days) and millimeter light curve (85.5 GHz, spanning $\delta t \approx 0.9$ –2.8 days) of the afterglow of GRB 130131A (Section A.1.2), along with the optical/NIR detections (RJK , spanning $\delta t \approx 0.04$ –0.67 days) and the *Swift* X-ray light curve spanning $\delta t \approx 7.5 \times 10^{-4}$ –4.7 days (Section A.1.1) for our afterglow modeling.

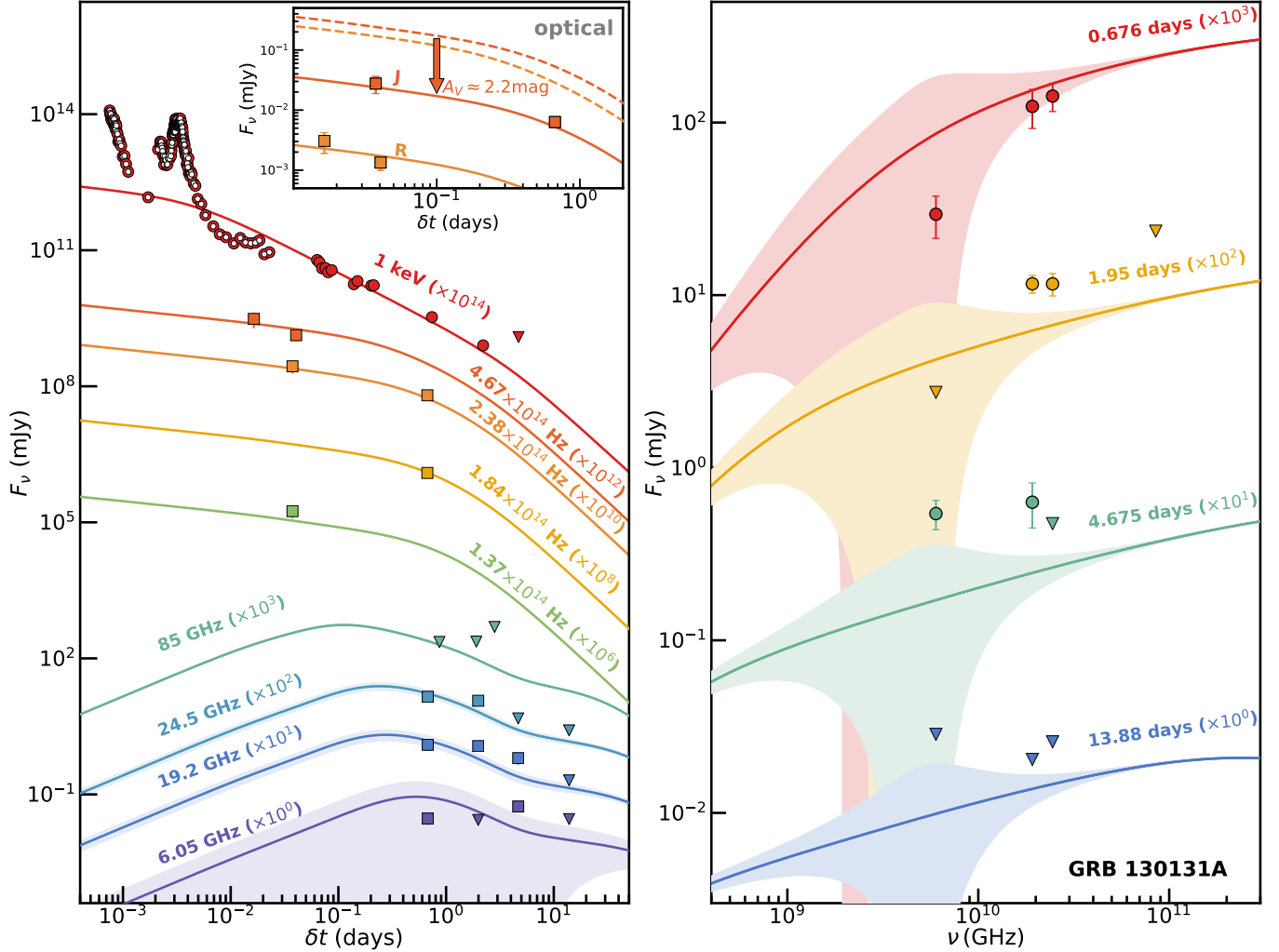


Figure 4. *Left:* X-ray, optical, NIR, millimeter and radio afterglow light curves of GRB 130131A, together with the best-fit forward shock model in a wind environment (lines). Squares represent data newly reported here, and triangles represent 3σ upper limits. Open symbols indicate data that are not included in the fit, and shaded regions represent variability due to scintillation. The inset shows the model *J*- and *R*-band light curves (solid lines) as well as the non-extinguished models (dashed lines), indicating $A_{V,GRB} \approx 2.2$ mag to explain the detections. *Right:* Radio and millimeter spectral energy distributions (SEDs) of the afterglow of GRB 130131A from $\delta t \approx 0.7$ - 13.9 days, together with the best-fit forward shock model (lines). Overall the model provides a good match to the broad-band temporal and spectral evolution of the afterglow.

3.3.1. Basic Considerations

To determine p and the location of ν_c , we turn our attention to the X-ray afterglow. We ignore the X-ray flaring activity of GRB 130131A ($\delta t \approx 0.08 - 2.28 \times 10^{-2}$ days, Figure 4), and only consider the X-ray light curve and spectra from $\delta t \approx 0.02 - 4.7$ days. We generate a PC-mode time-sliced spectra from the *Swift* online tool, which found $\Gamma_X = 2.4^{+0.3}_{-0.2}$ (1σ , Evans et al. 2009). The X-ray spectra for this time range can be characterized with $\beta_X = -1.4^{+0.3}_{-0.2}$ and the X-ray light curve for this time range can be fit with a single power law with $\alpha_X = -1.14 \pm 0.04$. We first consider the scenario in which $\nu_m < \nu_X < \nu_c$. In this regime, β_X would indi-

cate $p = 3.8 \pm 0.5$. However, the temporal decline of the X-ray light curve would indicate $p = 1.85 \pm 0.06$ in the wind environment and $p = 2.52 \pm 0.06$ in an ISM environment. While the values of p found for the ISM environment are consistent within 3σ , the nominal values of p for the spectral and light curve analysis differ by ≈ 1.3 . On the other hand, for the regime $\nu_m, \nu_c < \nu_X$, $\alpha_X = -1.14 \pm 0.04$ implies $p = 2.19 \pm 0.06$, and $\beta_X = -1.4^{+0.3}_{-0.2}$ implies $p = 2.8 \pm 0.5$. These values are more consistent (2σ), with a nominal value difference of only ≈ 0.6 . Therefore, the X-ray afterglow of GRB 130131A indicates $\nu_m, \nu_c < \nu_X$ and $p \approx 2.2 - 2.8$. Additionally, the X-ray light curve does not exhibit a break to $\delta t \approx 2.2$ days, placing a lower limit on any

jet break to $t_{\text{jet}} \gtrsim 2.2$ days. In this regime we cannot discriminate between the ISM and wind environments based on the X-ray afterglow alone.

We now consider whether the radio afterglow can provide additional constraints on the properties of GRB 130131A. The radio light curves of GRB 130131A are not well sampled, with only 4 epochs of observations (and 7 detections) between the 3 frequencies. Additionally, the 6.0 GHz light curve exhibits variability, with detections at $\delta t \approx 0.7$ and ≈ 4.7 days, interspersed with a non-detection at $\delta t \approx 2.0$ days. Variability on short time scales at $\nu_{\text{obs}} \lesssim 10$ GHz is likely attributable to scintillation (Rickett 1990), and we therefore ignore the 6.0 GHz light curve in our analytical arguments (but include it, along with the anticipated scintillation effects, in our MCMC modeling). Turning our attention to the 19.2 GHz and 24.5 GHz observations, we note that the observations have a positive spectral slope of $\beta \approx 0.6$ at $\delta t \approx 0.7$ days, and both the 19.2 GHz and 24.5 GHz light curves fade significantly at $\delta t > 2.0$ days, requiring $\alpha \gtrsim -0.7$ to be consistent with the later non-detections. These spectral and temporal indices can be consistent with either a wind environment pre-jet break if $\nu_{\text{sa}} < 19.2 - 24.5 \text{ GHz} < \nu_c < \nu_m$ (expected $\beta = 1/3$ and $\alpha = -2/3$), or an ISM or wind environment if $t_{\text{jet}} \approx 2.0$ days and $\nu_{\text{sa}} < 19.2 - 24.5 \text{ GHz} < \nu_m$ (expected $\beta = 1/3$ and $\alpha = -1/3$). Therefore, we are unable to discriminate between the ISM and wind environment with the 19.2 GHz and 24.5 GHz afterglow observations.

3.3.2. MCMC Modeling

As we cannot distinguish between the wind and ISM environments from our afterglow observations of GRB 130131A, we fit the data with both an ISM and wind environment. While the host galaxy of GRB 130131A does not have a spectroscopically determined redshift (see Section A.1.3), we assume a photometric redshift of $z = 1.55$ for both fits, based on host galaxy SED fitting (see Section 4). We find our wind environment model is marginally preferred by the data, providing a $\chi^2/d.o.f. \approx 25/187$ and $L \approx 137$, and we use this model for broader analysis in the rest of the paper. Comparatively, our ISM environment best fit model produced a $\chi^2/d.o.f. \approx 32/187$ and $L \approx 132$ (we provide the ISM fit in Appendix B.2 for completeness). We present the best fit wind model in Figure 4 and list the parameters as well as the summary statistics from the marginalized posterior density functions (medians and 68% credible intervals) in Table 2.

In confirmation of the arguments laid out in Section 3.3.1, we find $p \approx 2.3$, and $t_{\text{jet}} \approx 3.5$ days from our best

fit wind model. The spectrum remains in the fast cooling phase until $\delta t \approx 2.0$ days, and $\nu_m, \nu_c < \nu_X$ for the entirety of the X-ray afterglow that we consider. We find the optical/NIR afterglow detections are best fit with a line-of-sight extinction value of $A_{V,\text{GRB}} \approx 2.2$ mag.

The model matches the first epoch of 19.2 GHz and 24.5 GHz observations, but under-predicts the light curves at $\delta t \gtrsim 2.0$ days by $2 - 4\sigma$. This discrepancy can be reconciled somewhat by setting $t_{\text{jet}} \gtrsim 14$ days (past the time of all of our afterglow observations), but the model parameters of interest (E_K , n_0 , and $A_{V,\text{GRB}}$) are not significantly affected by this change. As suggested in Section 3.3.1, we expect strong scintillation at 6.0 GHz based on our model, consistent with the large variability observed in the 6.0 GHz light curve.

3.4. GRB 131229A

The radio and millimeter afterglow of GRB 131229A consists of single epoch observations at 6.0, 21.8, and 93 GHz, optical at $\delta t \approx 0.9 - 1.0$ days (Section A.4.2). The optical afterglow of GRB 131229A was not detected, with the deepest upper limits at $\delta t \approx 0.03$ days. The *Swift* X-ray afterglow spans $\delta t \approx 1.2 \times 10^{-3} - 1.3$ days (Section A.4.1).

We first investigate the X-ray light curve of GRB 131229A to determine p , the location of ν_c , and place limits on t_{jet} . The combined windowed timing (WT) mode and PC-mode X-ray light curve can be characterized by a broken power law (Equation 1), with $\alpha_1 \approx -1.0$ and $\alpha_2 \approx -1.4$. As the break in the light curve occurs between the WT-mode and PC-mode ($\delta t \approx 0.39 - 4.8 \times 10^{-2}$ days), we investigate each mode separately. The WT-mode X-ray light curve of GRB 131229A is characterized by a single power law of $\alpha_{\text{WT}} = -1.03 \pm 0.04$, where as the PC-mode X-ray light curve of GRB 131229A is characterized by a single power law of $\alpha_{\text{PC}} = -1.36 \pm 0.03$. The change in temporal index of $\Delta\alpha$ (see Section 3.1.1) is ≈ 0.34 , indicating this temporal break may be the passage of ν_c through the X-ray band (expected $\Delta\alpha = 0.25$).

If the break in the X-ray light curve is indeed the passage of ν_c , the derived p from the temporal and spectral indices should be consistent before and after the break. We create a WT-mode time-sliced spectra from the *Swift* online tool, and find the WT-mode ($\delta t \approx (1.2 - 3.9) \times 10^{-3}$ days) photon index to be $\Gamma_{\text{WT}} = 1.84^{+0.05}_{-0.05}$ (1σ , Evans et al. 2009), corresponding to a WT-mode spectral index of $\beta_{\text{WT}} = -0.84^{+0.05}_{-0.05}$. The hardness of this spectrum implies $\nu_m < \nu_X < \nu_c$, and we derive $p = 2.68^{+0.09}_{-0.09}$, assuming $\beta_{\text{WT}} = (1 - p)/2$. In a wind environment, the measured value of α_{WT} yields $p = 1.71^{+0.05}_{-0.05}$, which is inconsistent with our β_{WT} de-

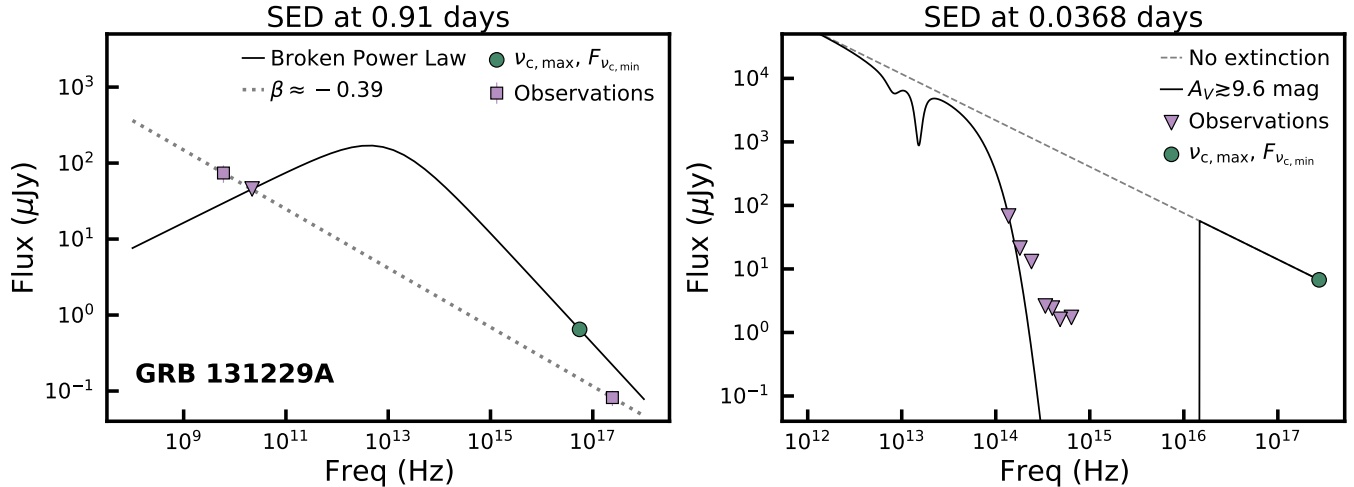


Figure 5. *Left:* Radio to X-ray SED of GRB 131229A at 0.91 days, with observations (purple) and estimated $F_{\nu_{c,\min}}$ at $\nu_{c,\max}$ (green). Black solid line indicates the broken power law fit between the 21.8 GHz upper limit and F_{ν_c} , where the break indicates $\nu_m \approx 10^{13}$ Hz. Dashed line indicates the extrapolation from $F_{\nu_{c,\min}}$ to radio frequencies. *Right:* Optical to X-ray SED of GRB 131229A at 0.0368 days, with optical/NIR upperlimits (purple) and estimated $F_{\nu_{c,\min}}$ at $\nu_{c,\max}$ (green). Dashed grey line represents the extrapolation from $F_{\nu_{c,\max}}$ assuming $\nu_m < \text{NIR/optical} < \nu_c$ with no extinction ($A_{V,\text{GRB}} = 0$ mag). Black solid line represents the extinction curve with the minimum extinction required to be consistent with the upper limits ($A_{V,\text{GRB}} \gtrsim 9.6$ mag).

rived p , and we therefore rule out a wind environment. On the other hand, in an ISM environment, the measured value of α_{WT} yields $p = 2.37_{-0.05}^{+0.05}$, which is consistent with the β_{WT} derived p within 3σ . We find a mean weighted WT-mode p of $p_{\text{WT}} = 2.44 \pm 0.04$. Past the break ($\delta t \approx 0.05 - 1.32$ days), we create a PC-mode time-sliced spectra from the *Swift* online tool, which finds the PC-mode photon index to be $\Gamma_{\text{PC}} = 2.14_{-0.10}^{+0.11}$ (1σ , Evans et al. 2009), corresponding to a PC-mode spectral index of $\beta_{\text{PC}} = -1.14_{-0.10}^{+0.11}$. Assuming $\nu_m, \nu_c < \nu_X$, we find β_{PC} yields $p = 2.28_{-0.20}^{+0.21}$, consistent with p_{WT} . Furthermore, α_{PC} yields $p = 2.49_{-0.04}^{+0.04}$, once again consistent with p_{WT} , and we find a mean weighted PC-mode p of $p_{\text{PC}} = 2.48 \pm 0.04$. We therefore conclude that an ISM environment is preferred for GRB 131229A, and that ν_c passes through the X-ray band between $\delta t \approx (0.39 - 4.8) \times 10^{-2}$ days, yielding an overall mean weighted p of $p = 2.46 \pm 0.03$. Furthermore, the X-ray light curve does not exhibit any additional steepening, placing a limit of $t_{\text{jet}} \gtrsim 1.3$ days.

We next examine the radio to X-ray SED at the time of the radio observations ($\delta t \approx 0.91$ days) to place constraints on the location of ν_m . The shallow radio to X-ray spectral index at $\delta t \approx 0.91$ days ($\beta_{\text{radio-X}} \approx -0.39$, dotted line, Figure 5) is inconsistent with a single, optically thin power law spectrum with index $\beta = (1 - p)/2 \approx -0.73$ extending from the radio to the X-rays, and instead requires a spectral peak in between.

In the regime of $6.0 \text{ GHz} < 21.8 \text{ GHz} < \nu_m < \nu_c$, we expect a positive spectral index of $\beta = 1/3$ for the radio

band. However, the observed limit of $\beta \lesssim -0.38$ between the 6.0 GHz and 21.8 GHz observations is inconsistent with this expectation. The discrepancy between the tentative detection at 6.0 GHz and the upper limit at 21.8 GHz may be explained by a variety of factors, such as the 6.0 GHz counterpart being unrelated to the FS afterglow of GRB 131229A, or due to scintillation effects which can cause variability on short timescales at $\nu_{\text{obs}} \lesssim 10$ GHz (Rickett 1990). We instead utilize the 21.8 GHz non-detection to place constraints on the FS emission.

We use the 21.8 GHz non-detection and the X-ray light curve to place constraints on the location of ν_c and ν_m . Based on our analytical arguments, the latest time ν_c can reasonably pass through the X-ray band is at the start of the PC-mode X-ray light curve ($\delta t \approx 4.8 \times 10^{-2}$ days), and therefore we assume $\nu_c \approx \nu_X$ at this time. Scaling ν_c to the time of the radio observations ($\nu_c \propto t^{-1/2}$), we find the maximum value of ν_c to be $\nu_{c,\max} \approx 5.5 \times 10^{16}$ Hz at $\delta t \approx 0.91$ days (resulting in $F_{\nu_{c,\min}} \approx 0.65 \mu\text{Jy}$). We fit a broken power law (Equation 2) with the 21.8 GHz non-detection and $F_{\nu_{c,\min}}$, fixing $\beta_1 = 1/3$, $\beta_2 = (1 - p)/2 \approx -0.73$, and $s = 1.84 - 0.40p \approx 0.856$. We find $\nu_m \gtrsim 10^{13}$ Hz (solid line, Figure 5).

Our X-ray analysis provides measured values of the synchrotron flux above ν_c , and our radio analysis provides a constraint on the synchrotron flux between ν_{sa} and ν_m (Table 1 in Granot & Sari 2002). Combined with our constraint on ν_c (Table 2 in Granot & Sari 2002),

we place limits on the energy, density, and microphysics of the system. Assuming a redshift of $z = 1.04$ (see Section 4), we find $E_{K,\text{iso}} \lesssim 3.21 \times 10^1 \epsilon_B^{1/3} 10^{52}$ erg, $n_0 \gtrsim 1.72 \times 10^{-5} \epsilon_B^{-5/3} \text{cm}^{-3}$, and $\epsilon_e \gtrsim 1.19 \times 10^{-2} \epsilon_B^{-1/3}$. Using these constraints, along with our constraint on t_{jet} , we place constraints on θ_{jet} and find $\theta_{\text{jet}} \gtrsim 1.32 \epsilon_B^{-1/4} (^\circ)$ (Sari et al. 1999).

We next place constraints on $A_{V,\text{GRB}}$ of GRB 131229A. Assuming $\nu_m < \text{NIR/optical} < \nu_c$, and using our assumption of $\nu_c \approx \nu_X$ at $\delta t \approx 4.8 \times 10^{-2}$ days, we interpolate the SED between ν_m and ν_c at the time of the most constraining optical/NIR upper-limits ($\delta t \approx 0.0368$ days). We find that the extinction necessary to be consistent with the optical/NIR upper limits is $A_{V,\text{GRB}} \gtrsim 9.6$ mag (see Figure 5).

In conclusion, we find for GRB 131229A $p = 2.46 \pm 0.03$, $t_{\text{jet}} \gtrsim 1.3$ days, and $A_{V,\text{GRB}} \gtrsim 9.6$ mag. We also place constraints on the isotropic energy and circumburst density of GRB 131229A of $E_{K,\text{iso}}/10^{52}$ erg $\lesssim 3.21 \times 10^1 \epsilon_B^{1/3}$ and $n_0 \gtrsim 1.72 \times 10^{-5} \epsilon_B^{-5/3}$, leading to further constraints on θ_{jet} . With limited radio observations, it is difficult to derive meaningful constraints on the afterglow properties of GRB 131229A within our MCMC modeling framework, and therefore we instead report our analytically derived values in Table 2.

3.5. GRB 140713A

We compiled the radio and millimeter light curves of the afterglow of GRB 140713A (Sec A.5.2), with WSRT and GMRT upper limits at 1.4 GHz spanning $\delta t \approx 11.1 - 25.1$ days, WSRT observations at 4.8 GHz spanning as well as VLA observations at 4.9 and 7.0 GHz $\delta t \approx 3.3 - 81.0$ days (all together, C-band), VLA observations at 13.4 and 15.9 GHz, as well as AMI observations at 15.7 GHz spanning $\delta t \approx 0.1 - 81.0$ days (all together, K_u -band), and CARMA observations at 85.5 GHz and PdBI observations at 86.7 GHz spanning $\delta t \approx 1.5 - 63.1$ days (all together, 3mm). In combination with the radio and millimeter light curves, we include the NOT optical limits at $\delta t \approx 0.2$ days and the *Swift* X-ray light curve spanning $\delta t \approx 1.5 \times 10^{-3} - 1.9$ days in our afterglow modelling (Sec A.5.1).

The afterglow of GRB 140713A has been previously modeled by Higgins et al. (2019), though they did not include IC effects. We choose to model GRB 140713A in our modeling framework both for consistency across the bursts in our sample, and because we are introducing new VLA and 3mm afterglow observations that have not previously been modeled.

3.5.1. Basic Considerations

We observe a steep decline in the 3mm light curve, with $\alpha \approx -2.2$ at $\delta t \gtrsim 12$ days. We cannot reconcile this steep decline with the standard synchrotron model of a spherical blast-wave, as the light curve slopes predicted by the standard model are too shallow. We therefore conclude that this decline is caused by a jet break, and that $t_{\text{jet}} \lesssim 12$ days. Furthermore, this decline indicates that $p \approx 2.2$, $\nu_m \approx 3\text{mm}$, and $F_{\nu,m} \approx 1.7$ mJy at $\delta t \approx 12$ days (see Section 3).

Assuming $\nu_m \approx 3\text{mm}$ at $\delta t \approx 12$ days, and evolving this break frequency and $F_{\nu,m}$ forward in time ($\nu_m \propto t^{-2}$, $F_{\nu,m} \propto t^{-1}$ post jet break, Sari et al. 1999) from 12 days, we find that $\nu_m \approx K_u$ -band at $\delta t \approx 28$ days, with a characteristic flux of $F_{\nu,m} \approx 0.76$ mJy. Indeed, we can fit the 15.7 GHz light curve with a steep power law of $\alpha \approx -2.0$ at $\delta t \gtrsim 27$ days, and find the flux at 27 days to be ≈ 0.78 mJy. Therefore, the K_u -band data corroborates that $t_{\text{jet}} \lesssim 12$ days, and we conclude that $p \approx 2.0 - 2.2$. With $t_{\text{jet}} \lesssim 12$ days, the majority of our radio and millimeter afterglow observations are taken at $\delta t \gtrsim t_{\text{jet}}$, and we are unable to discriminate between an ISM and wind environment using these observations.

We now determine the location of the X-rays in relation to ν_c . We ignore the X-ray flare ($\delta t \approx (0.15 - 1.9) \times 10^{-2}$ days, see Figure 6) of GRB 140713A, and as such we only consider the X-ray light curve and spectra from $\delta t \approx 0.06 - 1.88$ days in the synchrotron framework to determine the location of the X-rays in relation to ν_c . We create a time-sliced PC-mode spectra from the *Swift* online tool, which finds the X-ray photon index to be $\Gamma_X = 2.0 \pm 0.2$ (1σ , Evans et al. 2009). The X-ray spectra for this time range is characterized by $\beta_X = -1.0 \pm 0.2$ and the X-ray light curve for this time range can be fit with a single power law with $\alpha_X = -0.9 \pm 0.1$.

For $p \approx 2.1$, derived from the identification of a jet break in the radio afterglow, we would expect a spectral index of $\beta_X = (1 - p)/2 \approx -0.55$ if $\nu_m < \nu_X < \nu_c$ and $\beta_X = -p/2 \approx -1.05$ if $\nu_m, \nu_c < \nu_X$. The measured value of $\beta_X = -1.0 \pm 0.2$ is more consistent with the latter case, within 1σ , where as the former case is only consistent within 3σ . In the regime of $\nu_m, \nu_c < \nu_X$, we would expect $\alpha_X = (2 - 3p)/4 \approx -1.1$, consistent with our measured value of $\alpha_X \approx -0.9$ within 2σ . Therefore, we conclude $\nu_m, \nu_c < \nu_X$, and note that in this regime we can not discriminate between the ISM and wind environment with the X-ray light curve.

In conclusion, the radio and X-ray afterglow of GRB 140713A is consistent with $p \approx 2.0 - 2.2$, $t_{\text{jet}} \lesssim 12$ days, and $\nu_m, \nu_c < \nu_X$. Neither the radio nor X-ray observations allow us to analytically distinguish between the ISM and wind environment.

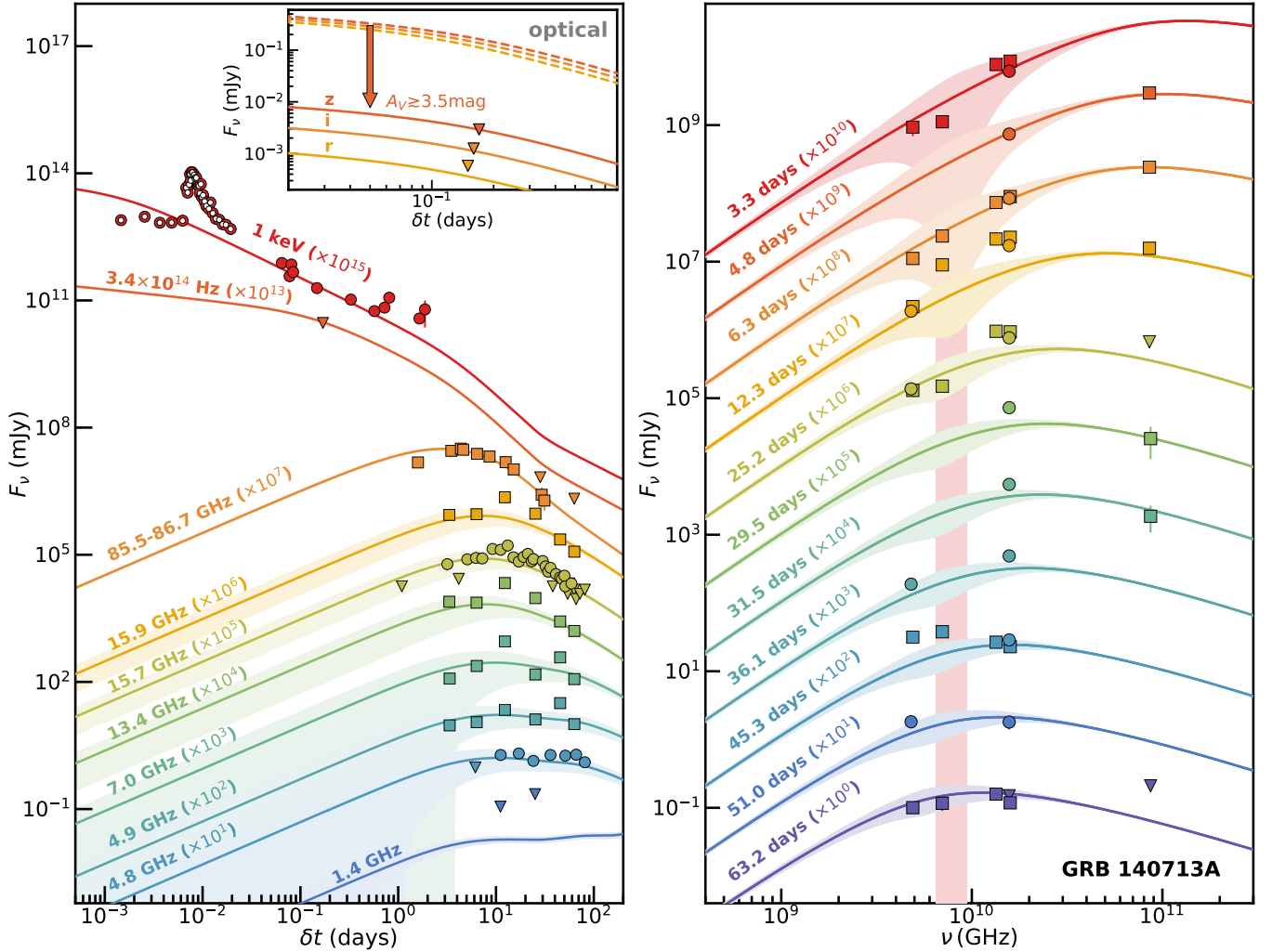


Figure 6. *Left:* X-ray, optical, millimeter and radio afterglow light curves of GRB 140713A, together with the best-fit forward shock model in a wind environment (lines). Squares represent data newly reported here, circles represent literature data (Higgins et al. (2019)), and triangles represent 3σ upper limits. Open symbols indicate data that are not included in the fit, and shaded regions represent variability due to scintillation. The inset shows the model r -, i -, and z -band light curves (solid lines) as well as the non-extinguished models (dashed lines), indicating $A_{V,\text{GRB}} \gtrsim 3.5$ mag to explain the upper limits. *Right:* Radio and millimeter spectral energy distributions (SEDs) of the afterglow of GRB 140713A from $\delta t \approx 3.0$ -31.5 days, together with the best-fit forward shock model (lines). Overall the model provides a good match to the broad-band temporal and spectral evolution of the afterglow.

3.5.2. MCMC Modeling

As we cannot distinguish between the wind and ISM environments from our afterglow observations of GRB 140713A, we fit the data with both an ISM and wind environment. We find that our wind environment model better fits the data, with the best fit model having a reduced $\chi^2 \approx 114/102$ and $L \approx 79$. Comparatively, our ISM environment best fit model produced a reduced $\chi^2 \approx 272/102$ and $L \approx 11$ (for completeness, we present the best fit ISM model in Appendix B.3). We present the best fit wind model in Figure 6 and list the parameters as well as the summary statistics from the

marginalized posterior density functions (medians and 68% credible intervals) in Table 2.

In confirmation of the arguments laid out in Section 3.5.1, the parameters of our best-fit model are $p \approx 2.17$ and $t_{\text{jet}} \approx 3.6$ days, resulting in a $\theta_{\text{jet}} \approx 21^\circ$. Additionally, the SED remains in the fast cooling phase until $\delta t \approx 35$ days, and the ordering of the break frequencies at $\delta t \approx 1.65$ days is $\nu_c < \nu_m < \nu_X$. For our best fit wind model, the NOT optical limits imply $A_{V,\text{GRB}} \gtrsim 3.52$ mag.

The X-ray model light curve under-predicts the data at $\delta t \gtrsim 0.7$ days. This is not unexpected, as we found in Section 3.5.1 that the X-ray temporal slope was shall-

Table 3. Host Galaxy Properties

GRB Name	z	$\log_{10}(M/M_{\odot})$	$\log_{10}(Z/Z_{\odot})$	SFR [M_{\odot}/yr]	t_m [Gyr]	A_V^{host} [mag]
110709B	2.109	$9.06^{+0.18}_{-0.29}$	$-0.63^{+0.33}_{-0.24}$	$2.73^{+2.07}_{-1.02}$	$0.40^{+0.45}_{-0.27}$	$0.61^{+0.23}_{-0.22}$
111215A	2.012	$9.98^{+0.30}_{-0.15}$	$0.15^{+0.03}_{-0.04}$	$50.83^{+18.27}_{-23.38}$	$0.20^{+0.60}_{-0.10}$	$0.83^{+0.09}_{-0.24}$
130131A	$1.55^{+0.02}_{-0.04}$	$9.62^{+0.20}_{-0.20}$	$0.10^{+0.06}_{-0.21}$	$78.74^{+34.44}_{-18.51}$	$0.05^{+0.06}_{-0.03}$	$1.08^{+0.05}_{-0.04}$
131229A	$1.04^{+0.32}_{-0.39}$	$9.50^{+0.27}_{-0.34}$	$-0.50^{+0.40}_{-0.30}$	$1.46^{+5.02}_{-1.45}$	$1.29^{+1.78}_{-0.87}$	$1.20^{+0.83}_{-0.66}$
140713A	0.935	$9.90^{+0.03}_{-0.04}$	$0.12^{+0.04}_{-0.05}$	$3.97^{+0.40}_{-0.46}$	$2.18^{+0.21}_{-0.29}$	$0.31^{+0.06}_{-0.06}$
160509A	1.17	10.30-10.86	-0.08-0.17	52.14-277.17	0.07-1.10	1.60-4.66

NOTE—Host galaxy properties derived by *Prospector*.

lower than the expected slope for $p \approx 2.1$. We first consider whether this excess flux in the X-ray light curve is due to KN effects, which become important when $\nu_X \geq \hat{\nu}_m$. Given our best fit parameters, we find that at $\delta t \approx 1.65$ days, $\hat{\nu}_m \approx 1.7 \times 10^{21}$ Hz $\gg \nu_X$. Therefore, we conclude that KN effects are not causing the excess flux in the X-ray light curve. We next consider whether IC effects are the cause of the excess flux in the X-ray light curve. We calculate the flux of the IC spectra at ν_X at $\delta t \approx 1.65$ days, and find that the IC flux at ν_X is $\approx 4.7 \times 10^{-7}$ mJy, ≈ 80 times smaller than the X-ray flux at that time. Therefore, IC effects cannot account for the excess X-ray flux, although we note that such excess emission has been seen in other events (Fong et al. 2014; Margutti et al. 2015; Laskar et al. 2018a, 2019).

Higgins et al. (2019) have previously modeled the afterglow of GRB 140713A. Their model allowed for $p < 2$, and they found a value of $p \approx 1.85$, smaller, but not far off from our value of $p \approx 2.17$. Their other parameters are also similar to ours, with the biggest difference in our model being that we identify a jet break in the 3mm light curve, and therefore find $t_{\text{jet}} \approx 3.61$ days, where as they predict $t_{\text{jet}} \approx 25 - 30$ days.

4. HOST GALAXY MODELING

To model the stellar population properties of the host galaxies, we use the stellar population inference code *Prospector* (Leja et al. 2017). *Prospector* determines properties such as total mass formed, age of the galaxy at the time of observation (t_{age}), optical depth of old and young stars, stellar metallicity (Z_*), the star formation history, and redshift using the available photometric and/or spectroscopic data for each host. We apply a nested sampling fitting routine with *dynesty* (Speagle 2020) to the observational data of each host to produce posterior distributions in each property. Model SEDs are built using *Python-fsps* (Flexible Stellar population synthesis; Conroy et al. 2009; Conroy & Gunn

2010). Unless the redshift of a host is known, we allow redshift to be a sampled parameter. For hosts with spectra, we fit their spectral continuum with a 10th order Chebyshev polynomial and add a gas-phase metallicity and gas ionization parameter to accurately fit the nebular emission lines. We also assume a Chabrier initial mass function (IMF) (Chabrier 2003), Milky-Way Dust Extinction Law (Cardelli et al. 1989), and a parametric delayed- τ SFH (SFH $\propto t * e^{-t/\tau}$), where the τ is a sampled parameter in the *Prospector* fitting. Furthermore, we apply the Gallazzi 2005 Mass-Metallicity relation (Gallazzi et al. 2005) and a 2:1 ratio in the dust attenuation between old and young stars respectively, as stellar populations are noticed to follow this trend (Calzetti et al. 2000; Price et al. 2014). The total dust attenuation in optical depth is converted to a V-band magnitude, and hence forth referred to as $A_{V,\text{Host}}$. We follow the methods in Nugent et al. (2020) to determine the mass-weighted age t_m , stellar mass (M_*), and star formation rate (SFR).

We model the host galaxy of GRB 110709B with photometry from Zauderer et al. (2013c) and Selsing et al. (2019) with a fixed $z = 2.109$ (Perley et al. 2016a; Selsing et al. 2019). We find that the stellar population has dust extinction $A_{V,\text{Host}} = 0.61^{+0.26}_{-0.25}$ mag (Table 3). Though the *Prospector* SED model fits the photometric data well, the model is based on only three detections and one limit (Figure 7).

We fit the host galaxy of GRB 111215A with photometry from van der Horst et al. (2015), corrected for Galactic extinction in the direction of the burst at a fixed the redshift of $z = 2.012$ (van der Horst et al. 2015; Chrimes et al. 2019). We find the host has dust attenuation $A_{V,\text{Host}} = 0.91^{+0.06}_{-0.08}$ mag. Our host galaxy properties are similar to those found by van der Horst et al. (2015).

For the host of GRB 130131A, the redshift is unknown, although the spectrum indicates $1.3 < z < 4$ (see Section

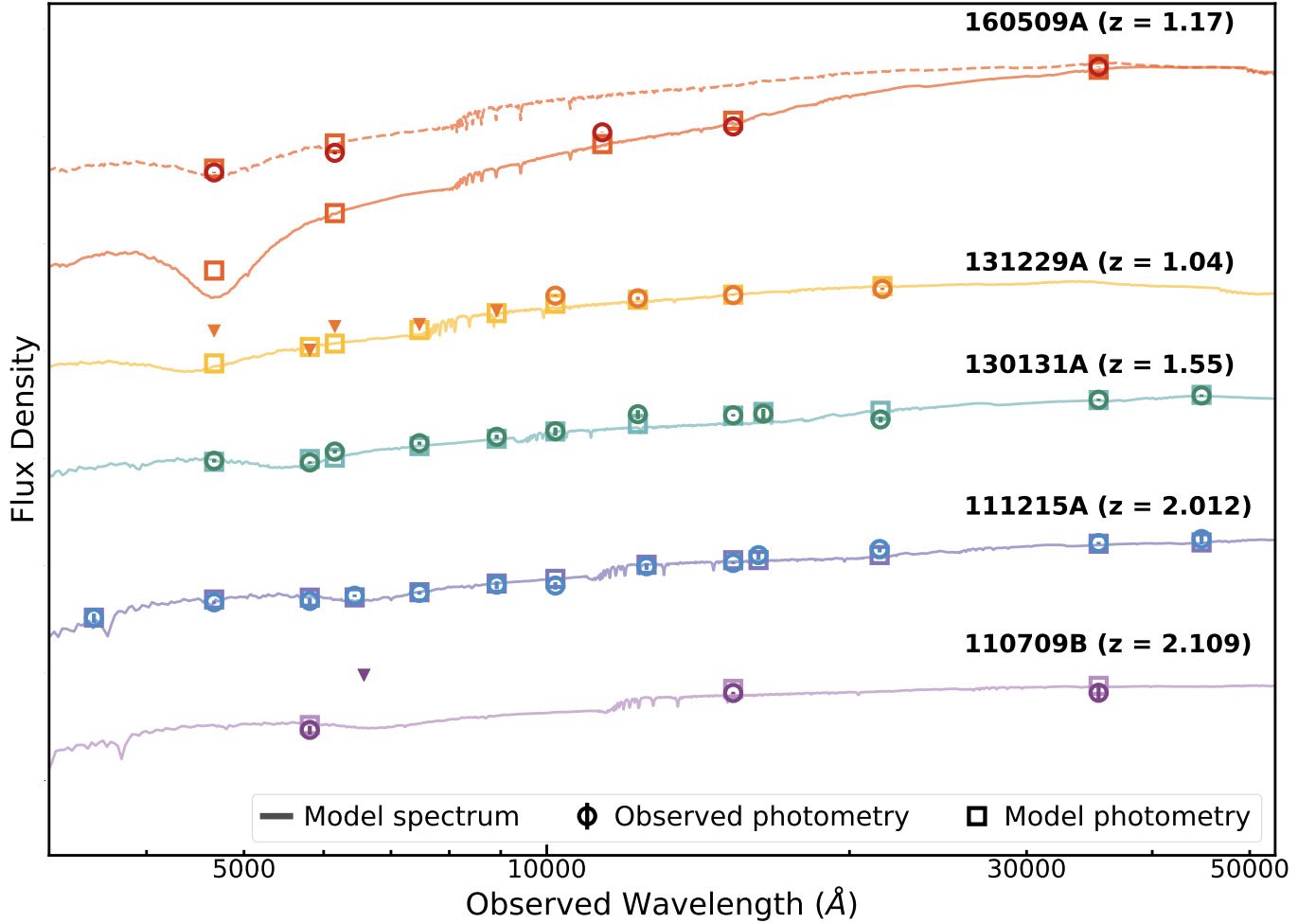


Figure 7. The observed host photometry (circles) of the dark GRBs modeled in this paper (GRBs 110709B, 111215A, 130131A, 131229A, and 160509A), as well as the *Prospector* model photometry (squares) and best-fit model spectrum (lines). For GRB 160509A, a second *Prospector* model is plotted that does not include the HST/WFC3 photometry of the host (dashed line, see Section 4 for details). The GRB SEDs are arbitrarily scaled in flux for clarity.

A.1.3). Thus, we leave redshift as a free parameter with a flat prior of $1.3 < z < 4$. We find a photometric redshift of $z = 1.55^{+0.01}_{-0.05}$, and $A_{V,\text{Host}} = 1.14^{+0.06}_{-0.04}$ mag.

For the host of GRB 131229A, the redshift is unknown, although the deep optical limits ($\gtrsim 23 - \gtrsim 26$ mag) indicates a redshift of $z \gtrsim 1 - 1.5$ (see Section A.4.3). Thus, we leave redshift as a free parameter with a flat prior of $0.1 < z < 3$. We find a photometric redshift of $z = 1.04^{+0.28}_{-0.36}$, and $A_{V,\text{Host}} = 1.17^{+0.72}_{-0.66}$ mag.

We jointly fit the photometric and spectroscopic data (Table A3) of the host of GRB 140713A. We find that the stellar population has a low $A_{V,\text{Host}} = 0.21^{+0.04}_{-0.04}$ mag. We also find that the photometry and spectrum of the host are overall well-fit by the *Prospector* SED model, especially the [OII] ($\lambda 3727\text{\AA}$) and $H\gamma$ spectral line strengths (Figure 8). Our host

galaxy properties are similar to those found by Higgins et al. (2019).

Finally, we fit the host galaxy of GRB 160509A, with a redshift of $z = 1.17$ (Laskar et al. 2016; Kangas et al. 2020). When we fit the full host galaxy SED of Keck/LRIS, HST/WFC3, and *Spitzer* photometry, our *Prospector* model over-predicts the Keck/LRIS photometry by an order of magnitude. This may indicate that the Keck/LRIS observations are dominated by afterglow contribution, in contradiction with Laskar et al. (2016). However, this *Prospector* model also finds a high $A_{V,\text{Host}}$ of ≈ 4.7 mag, much higher than what is expected for the normal dark GRB host population (i.e. Perley et al. 2013). This high value of $A_{V,\text{Host}}$ is driven by the color between the HST/WFC3 and *Spitzer* bands, and thus we also fit the host of GRB 160509A with only the Keck/LRIS and *Spitzer* photometry. This method

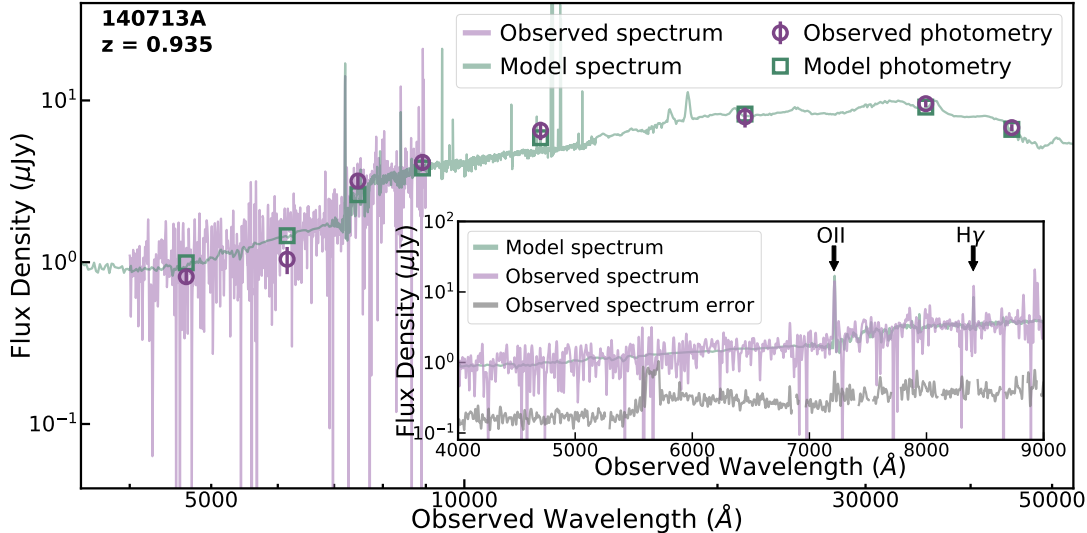


Figure 8. The *grizJK* and Spitzer photometry (purple circles) of GRB140713A compared to the *Prospector*-produced model spectrum (purple line) and photometry (green squares) at $z = 0.935$. The model is consistent with the observed photometry across the wide wavelength range. The inset shows a zoom-in of the observed LRIS spectrum (purple line), as well as the error spectrum (grey line), compared to the model spectrum.

results in a more expected $A_{V,Host} \approx 1.6$ mag, but the model under-predicts the HST/WFC3 photometry by a factor of ≈ 5 . Without further observations of the host galaxy of GRB 160509A, including re-observing at later times in g' - and r' -band, we cannot conclusively determine which fit is correct, and as such we quote the ranges for both fits in Table 3 and present both SEDs in Figure 7.

The full details of the best-fit properties for all of the host galaxies of our sample can be found in Table 3 and the model fits are displayed in Figure 7 and Figure 8.

5. DISCUSSION

We have presented multi-wavelength observations and modeling of the afterglows of five dark GRBs (GRBs 110709B, 111215A, 130131A, 131229A, 140713A), as well as SED modeling of the host galaxies of six dark GRBs with *Prospector* (GRBs 110709B, 111215A, 130131A, 131229A, 140713A, 160509A). We have classified two additional long GRBs as dark (GRBs 130420B, 130609A) and presented their radio and millimeter observations. However, for these two events, there is insufficient afterglow and host galaxy follow-up to allow for more in-depth modeling. For the purposes of this discussion, we group bursts that have been classified as dark (either explicitly, or satisfying $\beta_{OX} < 0.5$, i.e. Cenko et al. 2009; Melandri et al. 2012; Krühler et al. 2012; Rossi et al. 2012; Littlejohns et al. 2015) and/or “dusty” (i.e. Krühler et al. 2015; Perley et al. 2016a) and refer to both groups as “dark”. Equipped with this larger sample, including the new bursts presented here with particularly high extinction

site-lines, we now investigate whether dark GRBs differ from the broader long GRB population in terms of their γ -ray, afterglow, and host properties. In our comparisons we will refer to any long GRB not classified as dark as a “typical” GRB, for brevity.

5.1. The γ -ray and afterglow properties of Dark GRBs

To determine whether dark GRBs differ from the typical GRB population, we first examine their γ -ray properties: fluence (f_γ , 15-150 keV band) and duration (T_{90}), as even the dark GRBs with sparse afterglow data often have uniformly derived γ -ray properties from *Swift*/BAT. The exception to this is GRB 160509A, which was instead discovered by the *Fermi* Large Area Telescope (LAT; Longo et al. 2016). We plot these properties from the catalog in Lien et al. (2016) in Figure 9 for 103 dark GRBs (as classified by Jakobsson et al. 2004; Castro-Tirado et al. 2007; Cenko et al. 2009; van der Horst et al. 2009; Krühler et al. 2011, 2012; Zauderer et al. 2013c; Perley et al. 2013; Hunt et al. 2014; Chrimes et al. 2019, and This Work) as red points, and all other typical GRBs as blue points. We find that there is a notable lack of dark GRBs in the parameter space corresponding to low fluence ($f_\gamma \lesssim 2 \times 10^{-7}$ erg/cm²) and short duration ($2 \text{ s} < T_{90} \lesssim 5 \text{ s}$). For each parameter, we test the null hypothesis that the dark GRB population is drawn from the same distribution as the typical GRB population using a two-sample Kolmogorov-Smirnov (KS) test from the `scipy.stats` package, where a value of $p < 0.05$ rejects the null hypothesis. We obtain $p = 0.0001$ for the f_γ distribution and $p = 0.0503$ for the T_{90} distribution, implying that

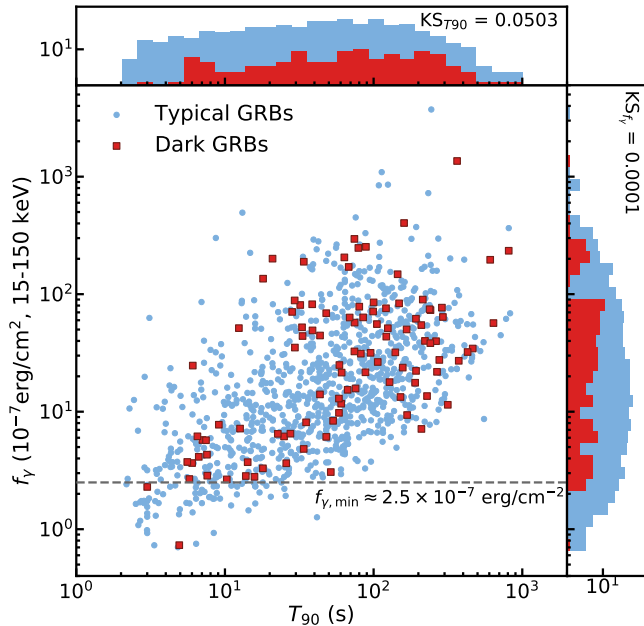


Figure 9. *Swift*/BAT fluence (f_γ) in the 15-150 keV band versus duration (T_{90}) of 976 long GRBs (blue points) and 103 dark GRBs (red squares), as derived by Lien et al. (2016). Dark GRB classification is based on the either explicit classification, or satisfying $\beta_{\text{OX}} < 0.5$ (Cenko et al. 2009; Krühler et al. 2011, 2012; Melandri et al. 2012; Rossi et al. 2012; Perley et al. 2013; Hunt et al. 2014; Schady et al. 2014; Jeong et al. 2014; Littlejohns et al. 2015; Perley et al. 2016a; Chrimes et al. 2019, This Work). The dashed horizontal line represents the theoretical minimum $f_{\gamma, \text{min}} \approx 2.5 \times 10^{-7}$ erg/cm², below which the X-ray (and therefore optical) afterglow is typically too faint to be classified as dark with ground based rapid optical follow-up that reaches limits of $R > 24$ mag. A simple 2 sample Kolmogorov-Smirnov (KS) test from the `scipy.stats` package which tests the null hypothesis that dark GRBs are drawn from the same population as the typical GRB population, finds $p = 0.0001$ for the f_γ distribution and $p = 0.0503$ for the T_{90} distribution, where a value of $p < 0.05$ rejects the null hypothesis.

dark GRBs are not drawn from the typical GRB population in terms of their fluence, but may be in terms of their duration.

One possible explanation for the lack of dark GRBs in the low f_γ and short T_{90} parameter space may be an observational bias in missing dark GRBs with low fluence⁶, as these bursts have been shown to have systematically fainter X-ray afterglows, and in turn fainter optical afterglows than the rest of the population (Gehrels et al. 2008). Thus, such bursts may have afterglows

which are fainter than the sensitivity threshold of optical afterglow searches, preventing accurate classification of these lower f_γ events as dark. To quantify this effect, we use the Jakobsson et al. (2004) darkness classification of $\beta_{\text{OX}} < 0.5$, and assume prompt optical observations ($\delta t \approx 0.1$ days) of $R > 24$ mag, which represents normal GRB follow-up capabilities. The minimum X-ray flux at 0.1 days needed to accurately classify a burst as dark is $F_{\text{X}, \text{min}} \approx 4.1 \times 10^{-2}$ μJy . We extrapolate $F_{\text{X}, \text{min}}$ to $\delta t = 11$ hr assuming $F_{\text{X}} \propto t^{-1}$ (see Nousek et al. 2006; Zhang et al. 2006; Evans et al. 2009), and use the derived $F_{\text{X}, 11 \text{ hr}} - f_\gamma$ relation of Gehrels et al. (2008) to calculate the minimum fluence of $f_{\gamma, \text{min}} \approx 2.5 \times 10^{-7}$ erg cm⁻² necessary to produce an X-ray afterglow bright enough to accurately classify a GRB as dark. This limit lies just below the majority of dark GRBs with the lowest f_γ (Figure 9). Therefore, it is plausible that the lack of low f_γ dark bursts is due to an observational bias, as opposed to an intrinsic effect. Additionally, as f_γ and T_{90} are correlated (Balázs et al. 2004), this also provides a natural explanation for the lack of observed dark bursts at $2 \text{ s} < T_{90} < 5 \text{ s}$. If we exclude bursts with $f_\gamma < 2.5 \times 10^{-7}$ erg cm⁻² then the dark GRB population does become more statistically similar to the long GRB population ($p = 0.0002$ for the f_γ distribution, $p = 0.0734$ for the T_{90} distribution). Finally, we note that there is not a complete catalogue of all dark GRBs, and we may be missing a significant fraction of the dark GRB population. This is made apparent when one considers that the estimated fraction of dark GRBs with respect to all long GRBs is 10-50% (Jakobsson et al. 2004; Cenko et al. 2009; Fynbo et al. 2009; Greiner et al. 2011; Melandri et al. 2012; Perley et al. 2013), whereas only $\sim 10\%$ of the long GRBs in Figure 9 have been classified as dark.

We next explore the dark GRB inferred burst explosion properties (e.g., kinetic energies and opening angles) to investigate whether dark GRBs differ from the typical population. As most dark GRBs do not have extensive broadband afterglow modeling, we focus on the six dark GRBs (GRBs 110709B, 111215A, 130131A, 131229A, 140713A, 160509A) in our sample which are uniformly modeled. We find that the dark GRB sample spans a wide range of beaming-corrected kinetic energies ($E_{\text{K}} \approx 0.01 - 6.6 \times 10^{51}$ erg). Compared to the values for other long GRBs with afterglow modeling (Panaitescu & Kumar 2002; Price et al. 2002; Yost et al. 2003; Frail et al. 2005; Chandra et al. 2008; Cenko et al. 2010, 2011; Laskar et al. 2013c, 2014, 2015; Alexander et al. 2017; Tanvir et al. 2018; Laskar et al. 2018a,b,c, 2019), we find that the kinetic energies of the dark GRB sample are consistent with those of the typical

⁶ f_γ and T_{90} are correlated ($f_\gamma \propto T_{90}^{-1.11}$; Balázs et al. 2004) (van der Horst et al. 2009). Therefore we focus our discussion on f_γ .

GRB sample, $E_K \approx 0.01 - 36.0 \times 10^{51}$ erg. Additionally, our dark GRB sample spans a wide range of jet opening angles ($\theta_{\text{jet}} \approx 1.6 - 21^\circ$), with a distribution again consistent with that of the typical GRB population ($\theta_{\text{jet}} \approx 1.1 - 50^\circ$). There is no clear evidence that dark GRBs are distinct from the typical GRB population in afterglow properties. Our conclusions do not change if we broaden our sample to include the small sample of long GRBs with $A_{V,\text{GRB}} > 1$ mag that have not been classified as dark (GRBs 980329 and 980703; Yost et al. 2003, and GRB 011121; Price et al. 2002).

5.2. The origin of the dust along the line-of-sight

We next consider whether our dark GRB sample has different environmental properties than typical GRBs. In practice, the higher line-of-sight extinctions derived for dark GRBs could be a result of local environment (probed by the afterglow), larger structures such as star-forming regions, global host galaxy dust distributions, or a combination of all three. An investigation into the global and local environmental properties of long GRBs will help determine the cause of the extinction of dark GRBs.

First, we investigate the global host properties of dark GRBs, to examine how their hosts differ from the typical GRB host population. We gather a sample of 150 GRB hosts that have inferred stellar mass measurements (M_*/M_\odot , Savaglio et al. 2009; Leibler & Berger 2010; Perley et al. 2013; Hunt et al. 2014; Piranomonte et al. 2015; Perley et al. 2016b; Japelj et al. 2016; Palmerio et al. 2019, This Work), and plot the $\log(M_*/M_\odot)$ distribution of the typical and dark GRB host populations in Figure 10. We find that the host galaxies of dark GRBs tend to be more massive (median $\log(M_*/M_\odot) \approx 9.9$) than typical GRB host galaxies (median $\log(M_*/M_\odot) \approx 9.2$), in alignment with previous results based on smaller samples (Krühler et al. 2011; Perley et al. 2013). Moreover, we find that only $\sim 16\%$ (12/82, excluding upper limits) of the hosts of the typical GRB population are more massive than the median host mass of the dark GRB population. A natural explanation could be that high-mass galaxies have a larger number of obscured sight lines as they overall have larger dust contents (e.g. Santini et al. 2014; Calura et al. 2017) which would result in high- A_V , dark GRBs in these types of hosts (Perley et al. 2013).

To further this point, we gather a sample of 152 GRBs that have inferred global host extinctions ($A_{V,\text{Host}}$, Savaglio et al. 2009; Perley et al. 2013; Hunt et al. 2014; Krühler et al. 2015; Piranomonte et al. 2015; Japelj et al. 2016, This Work), and plot the $A_{V,\text{Host}}$ distribution of the typical GRB population and the dark GRB

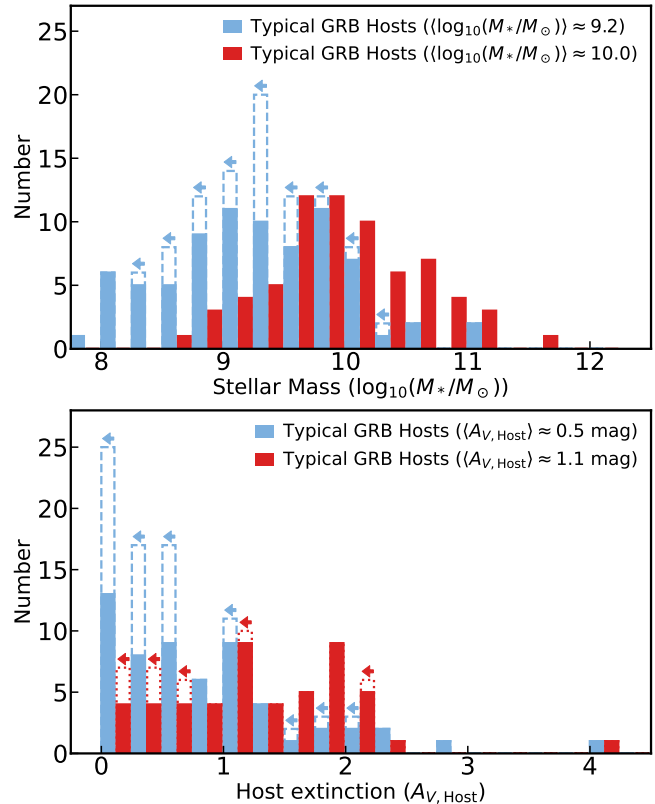


Figure 10. *Top:* Distribution of inferred stellar masses ($\log_{10}(M_*/M_\odot)$) of the hosts of 82 typical GRBs (blue) and the hosts of 68 dark GRBs (red), gathered from the literature (Savaglio et al. 2009; Leibler & Berger 2010; Perley et al. 2013; Hunt et al. 2014; Piranomonte et al. 2015; Perley et al. 2016b; Japelj et al. 2016; Palmerio et al. 2019, This Work). Available upper limits are denoted by dashed, unfilled distribution with leftward arrow. The hosts of the dark GRB population are generally more massive than the typical GRB population (median $\log_{10}(M_*/M_\odot) \approx 9.9$ for the hosts of dark GRB population, vs median $\log_{10}(M_*/M_\odot) \approx 9.2$ for the typical GRB population) *Bottom:* Distribution of extinction, $A_{V,\text{Host}}$, of 92 typical GRB hosts (blue) and 60 dark GRB hosts (red), gathered from the literature (Savaglio et al. 2009; Perley et al. 2013; Hunt et al. 2014; Krühler et al. 2015; Piranomonte et al. 2015; Japelj et al. 2016, This Work), where upper limits are denoted by dashed, unfilled distribution with leftward arrow. The hosts of the dark GRB population are generally more dusty than the typical GRB population (median $A_{V,\text{Host}} \approx 1.1$ mag for the hosts of dark GRB population, vs median $A_{V,\text{Host}} \approx 0.5$ mag for the typical GRB population)

population in Figure 10. Indeed, we find that dark GRBs typically occur in dustier host galaxies (median $A_{V,\text{Host}} \approx 1.1$ mag) compared to typical GRBs (median $A_{V,\text{Host}} \approx 0.5$ mag) (see also Perley et al. 2013). This trend, combined with the tendency of dark GRBs to occur in more massive galaxies, implies that the mass

of dark GRB host galaxies is linked to a dustier host galaxy overall. Indeed, there are known positive correlations between stellar mass and dust mass (e.g. Santini et al. 2014; Calura et al. 2017), that support this idea. The trend of dark GRBs originating in massive, dusty hosts indicates that the high line-of-sight extinction of dark GRBs is, at least in part, attributed to global host extinction.

We next investigate whether the dust extinction of dark GRBs as inferred from their afterglows is linked to the dust content of the host galaxy by determining whether $A_{V,GRB}$ is directly linked to the $A_{V,Host}$. Perley et al. (2013) suggested that the majority of long GRBs have $A_{V,GRB}$ values within a factor of $\sim 2 - 3$ of their host $A_{V,Host}$, following a near 1 : 1 relation between $A_{V,GRB}$ and $A_{V,Host}$. This correlation between $A_{V,GRB}$ and $A_{V,Host}$ could occur, for instance, if host galaxies of GRBs have uniform dust distributions, resulting in a homogenous screen of dust in the hosts' diffuse ISM (see Perley et al. 2013). To test this, we gather available $A_{V,GRB}$ measurements from the literature for typical (Kann et al. 2006, 2010; Liang & Li 2010; Covino et al. 2013; Zafar et al. 2011; Greiner et al. 2011; Littlejohns et al. 2015) and dark GRBs (Kann et al. 2010; Liang & Li 2010; Krühler et al. 2011; Greiner et al. 2011; Zafar et al. 2011; Perley et al. 2013; Covino et al. 2013; Littlejohns et al. 2015; Laskar et al. 2016, This Work) and compare them to their corresponding $A_{V,Host}$ (Cenko et al. 2009; Savaglio et al. 2009; Krühler et al. 2011; Perley et al. 2013, 2015; Krühler et al. 2015; Piranomonte et al. 2015; Vergani et al. 2015; Japelj et al. 2016, This Work). We plot the $A_{V,Host}$ - $A_{V,GRB}$ pairs in Figure 11, and find that the entire long GRB population spans a wide range of $A_{V,Host}$ ($\sim 0 - 4.7$ mag) and $A_{V,GRB}$ (~ 0 to $\gtrsim 12.3$ mag).

To test whether there is a relation between $A_{V,Host}$ and $A_{V,GRB}$, we randomly sample $A_{V,Host}$ - $A_{V,GRB}$ pairs from the long GRB sample for which there are published $A_{V,Host}$ and $A_{V,GRB}$ values, taking into account error bars and upper/lower limits,⁷ and fit a line to the randomly drawn sample using `curve_fit` from the `scipy`

package. We repeat this process 1000 times and produce a distribution of line slopes that are fit by the $A_{V,Host}$ - $A_{V,GRB}$ pairs. We find that our distribution of $A_{V,Host}$ - $A_{V,GRB}$ slopes has a median value of ≈ 0.05 , a nearly flat correlation instead of a 1 : 1 relation. Moreover, within the dark GRB sample alone, we also find only weak correlation between $A_{V,Host}$ - $A_{V,GRB}$ (median slope of ≈ 0.03). The weak correlation between $A_{V,Host}$ and $A_{V,GRB}$ could indicate that either that the high line-of-sight extinction is caused by dust extinction from the extremely local (\sim parsec) environment of the dark GRB, or that the host galaxies of long GRBs have patchy, rather than a uniform, dust distributions. In this latter case, the dust extinction driving the high $A_{V,GRB}$ is a geometrical line-of-sight effect that is probabilistic in nature.

To investigate the contribution of the extremely local environment of the GRB (within the blast wave radius $\sim 0.2 - 50$ parsec) to the high line-of-sight extinctions, we compare the circumburst densities as inferred from the afterglow. The naive expectation is that if the dust that is providing obscuration of the afterglow originates on \sim parsec scales, dark GRBs will trace environments with higher inferred densities. The sample of six dark GRBs we model in this paper spans a wide range of densities ($n_0 \sim 10^{-3} - 10^1 \text{ cm}^{-3}$; in the cases of wind environments we calculate n_0 at 10^{17} cm). Compared to typical long GRBs (Panaitescu & Kumar 2002; Price et al. 2002; Yost et al. 2003; Frail et al. 2005; Chandra et al. 2008; Cenko et al. 2010, 2011; Laskar et al. 2013c, 2014, 2015; Alexander et al. 2017; Tanvir et al. 2018; Laskar et al. 2018a,b,c, 2019), the densities of the dark GRBs in our sample fall well within the bounds of the typical GRB sample as a whole ($n_0 \sim 10^{-5} - 10^3 \text{ cm}^{-3}$). Additionally, we find that $A_{V,GRB}$ is not correlated with the circumburst density. Indeed, the long GRBs with the highest measured densities (GRBs 050904 and 120404A, $n_0 \sim 3.5 - 6.3 \times 10^2 \text{ cm}^{-3}$) have low inferred $A_{V,GRB}$ values ($\lesssim 0.05 - 0.13$ mag; Laskar et al. 2014, 2015). This implies that the higher inferred line-of-sight extinction for dark GRBs is not a result of the extremely local environment ($\sim 0.2 - 50 \text{ pc}$).

In summary, we find that dark GRBs tend to occur in more massive, dustier host galaxies than typical GRBs. Additionally, the observed dust obscuration of dark GRBs favors a patchy dust distribution over a uniform one in host galaxies, as $A_{V,GRB}$ is only weakly correlated to $A_{V,Host}$. Furthermore, the dust obscuration of dark GRBs is not purely a result of the extremely local (\sim parsec) environment of the GRB, as $A_{V,GRB}$ is not correlated to the circumburst density. The combination of high dust content and a patchy dust distribution

⁷ For cases in which there are quoted error bars for an A_V value (either $A_{V,Host}$ or $A_{V,GRB}$), we randomly sample using an asymmetric Gaussian, with the A_V value as the mean, μ , and the upper and lower errors on A_V as the standard deviation, σ , for either side of the Gaussian, respectively. For cases in which there is an upper limit quoted for an A_V value, we randomly sample using a tophat function from 0 to the A_V value. For GRB 160509A we assume a tophat function for $A_{V,Host}$ from 1.60-4.66 mag (See Section 4) Finally, for cases in which there is a lower limit quoted for an $A_{V,GRB}$ value, we randomly sample from a half Gaussian distribution with the $A_{V,GRB}$ lower limit as μ , and a 5σ maximum $A_{V,GRB}$ of 25 mag, such that $\sigma = (25 - \mu)/5$.

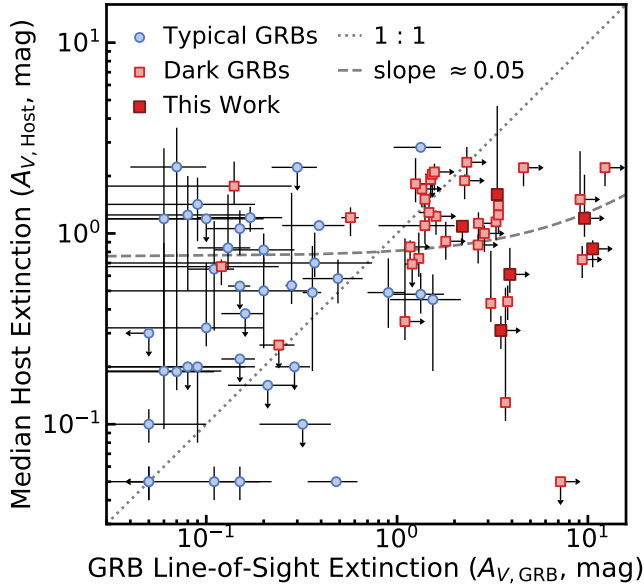


Figure 11. Median Host Extinction ($A_{V,\text{Host}}$) versus GRB line-of-sight extinction ($A_{V,\text{GRB}}$) for the dark (light red squares) and typical, optically-bright (blue circles) long GRB populations, with $A_{V,\text{GRB}}$ from Kann et al. (2006, 2010); Zafar et al. (2011); Greiner et al. (2011); Krühler et al. (2011); Perley et al. (2013) and $A_{V,\text{Host}}$ from Savaglio et al. (2009); Perley et al. (2013); Krühler et al. (2015); Japelj et al. (2016); Krühler et al. (2011); Perley et al. (2013). Our sample of six dark GRBs with $A_{V,\text{Host}}$ and $A_{V,\text{GRB}}$ measurements are represented by red squares with dark outlines. When necessary, we convert E_{B-V} values to $A_{V,\text{Host}}$ using the convention $R = E_{B-V}/A_V = 3.14$ (Schultz & Wiemer 1975). To be consistent with Figure 15 from Perley et al. (2013), for host galaxies with upper limits on their median host extinction, we plot the upper limit at the upper bound ($+1\sigma$) of the allowed $A_{V,\text{Host}}$ range. Additionally, we choose the $A_{V,\text{GRB}}$ derived from the SMC dust fit from Table 1 of Kann et al. (2006) and Table 3 of Kann et al. (2010), both to be consistent with Figure 15 from Perley et al. (2013) and to be consistent with our sample, for which we also use an SMC dust extinction law. For clarity, for GRBs with $A_{V,\text{Host}}$ or $A_{V,\text{GRB}} \approx 0.0$ mag, we plot their upper bounds at 0.05 mag. The dotted line denotes a 1 : 1 relation between median host extinction and GRB line-of-sight extinction. The dashed line denotes the correlation found between $A_{V,\text{Host}}-A_{V,\text{GRB}}$ pairs, with a slope of ≈ 0.05 (see Section 5.2). These lines are meant to guide the readers eye.

results in a higher probability of any given line-of-sight to intersect a patch of dust, leading to a high $A_{V,\text{GRB}}$ and dark GRB. The combination of high line-of-sight extinctions, patchy dust distributions, and association of long GRBs with star-forming galaxies, make dark GRBs exciting probes of obscured star formation.

5.3. SFR and Radio Limits

We next place limits on the amount of obscured star formation (SF) occurring in the host galaxies of the typical GRBs and dark GRBs. Long GRBs are inherently linked to SF due to their massive star progenitors and therefore their association with star-forming galaxies (Djorgovski et al. 1998; Christensen et al. 2004; Japelj et al. 2016; Palmerio et al. 2019). Additionally, massive, dusty, galaxies such as those that host dark GRBs often have higher SFRs (Santini et al. 2014; Calura et al. 2017), which has been corroborated by dark GRB host studies (e.g. Perley et al. 2013), and patchy dust distributions within dark GRB hosts may increase the probability of ongoing SF in the host to be obscured (Perley & Perley 2013). This obscured SF may result in radio bright host galaxies, as the dust becomes transparent at radio wavelengths and reveals the true SFR ($\text{SFR}_{\text{Radio}}$), whereas the SFR measured from UV/optical (e.g. emission line) diagnostics and from stellar population synthesis modeling of broad-band, galaxy-integrated photometry is only sensitive to the SFR unobscured by dust (Perley & Perley 2013). The search for radio emission from typical GRB host galaxies and dark GRB hosts is of interest as the results help answer the question of whether long GRBs are biased or unbiased tracers of SF across the universe (i.e. Perley & Perley 2013; Perley et al. 2015; Gatkine et al. 2020).

Several studies have been conducted to search for radio emission from long GRB host galaxies (Perley & Perley 2013; Stanway et al. 2014; Perley et al. 2015; Greiner et al. 2016; Perley et al. 2017; Gatkine et al. 2020; Eftekhari et al. 2021), with a handful (~ 10) of successful detections. These studies are not necessarily representative of the overall long GRB host population, as some focused exclusively on dark GRBs, some focused on typical GRBs at high redshift ($z > 2.5$), and few took an unbiased approach to all long GRB hosts. As there is no large, unbiased, survey of radio observations of long GRB host galaxies, we must rely on the these smaller studies, despite their potential biases in sample selection. We collect the radio fluxes from these studies to provide a broad view of the currently available observations, as well as to make comparisons to our sample of six dark GRBs. We calculate the $\text{SFR}_{\text{Radio}}$ of these observations using the relation in Greiner et al. (2016) (assuming a spectral index of -0.75), and plot them against the SED-derived SFR (SFR_{SED} , Perley et al. 2013, 2015, supplementing with UV-derived SFR or SFR tracers such as $\text{H}\alpha$, $\text{H}\beta$, and OII from Hunt et al. 2014; Krühler et al. 2015), in Figure 12. For comparison, we also plot a sample of star-forming field galaxies

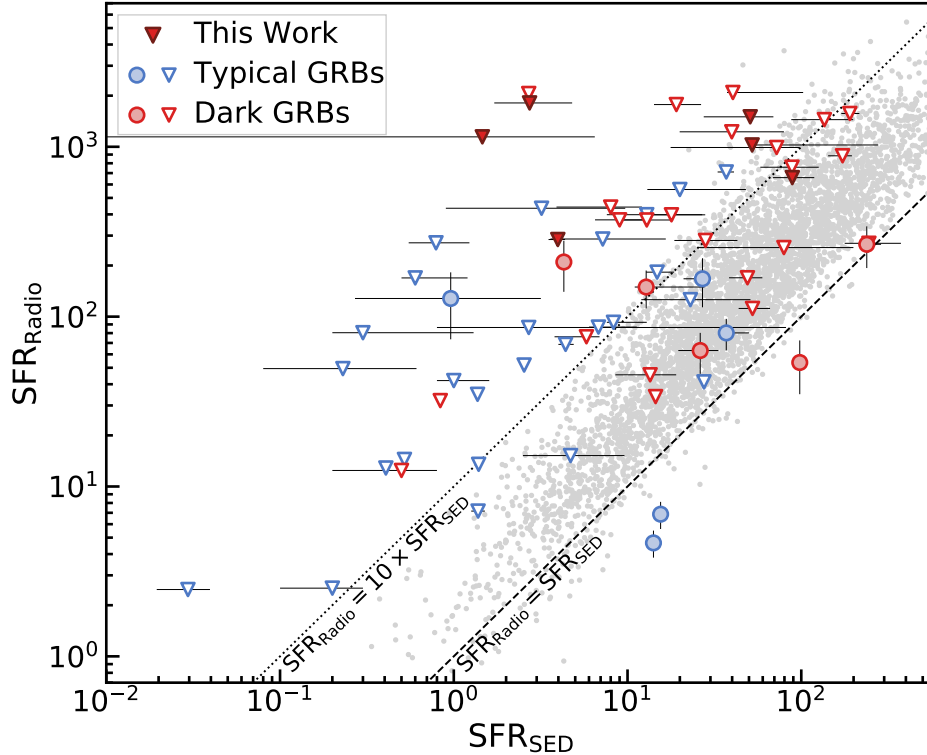


Figure 12. Radio SFR ($\text{SFR}_{\text{Radio}}$) versus SED derived SFR (SFR_{SED}) for typical GRB host galaxies (blue) and dark GRB host galaxies (red). Triangles correspond to radio upper limits. $\text{SFR}_{\text{Radio}}$ derived from radio observations in the literature (Perley & Perley 2013; Stanway et al. 2014; Perley et al. 2015; Greiner et al. 2016; Perley et al. 2017; Gatkine et al. 2020; Eftekhari et al. 2021) using the $\text{SFR}_{\text{Radio}}$ relation in Greiner et al. (2016) and assuming a spectral index of -0.75 . SFR_{SED} is taken from the literature (Perley et al. 2013, 2015) and supplemented with UV derived SFR or SFR tracers such as H_{α} (Hunt et al. 2014; Krühler et al. 2015). Our sample of 6 dark GRBs are shown as filled in red triangles, with $\text{SFR}_{\text{Radio}}$ from the most constraining radio afterglow upper limits and SFR_{SED} from our *Prospector* host galaxy modeling. Also shown are a sample of star forming galaxies for comparable redshifts $z \approx 0.03 - 3.4$ from the VLA-COSMOS source catalog (grey, Smolčić et al. 2017). The dashed and dotted line indicate $\text{SFR}_{\text{Radio}} = \text{SFR}_{\text{SED}}$ and $\text{SFR}_{\text{Radio}} = 10 \times \text{SFR}_{\text{SED}}$, respectively.

at comparable redshifts ($z \approx 0.03 - 3.4$) from the VLA-COSMOS source catalog (Smolčić et al. 2017).

The VLA-COSMOS sources typically have SFR ratios, $R_{\text{SFR}} = \text{SFR}_{\text{Radio}}/\text{SFR}_{\text{SED}}$, on the order of $\approx 1 - 10$. We define galaxies with “significant” obscured SF as galaxies that satisfy $R_{\text{SFR}} \gg 10$. Of the ~ 80 long GRB host galaxies that have been observed at radio wavelengths, only ~ 10 have unambiguous host detections (Perley & Perley 2013; Stanway et al. 2014; Perley et al. 2015, 2017). Of the ~ 10 detected long GRB host galaxies, only 3 display significant amounts of obscured SF, and the majority of radio detected long GRB hosts have R_{SFR} within the range we would expect compared to other star forming galaxies ($R_{\text{SFR}} \approx 1 - 10$, i.e. the VLA-COSMOS sources).

To assess the detectability of such obscured SF in the hosts of the six dark GRBs in our sample, we now place upper limits on the $\text{SFR}_{\text{radio}}$ of the host galaxies. We consider the most constraining afterglow upper limits of our sample (Zauderer et al. 2013c; van der Horst et al.

2015; Chandra & Nayana 2014a; Laskar et al. 2016, This Work), and we place limits of $R_{\text{SFR}} \lesssim 8 - 700$ (also plotted in Figure 12). With the afterglow radio limits, we are unable to rule out significant amounts of obscured SF for all bursts in our sample except GRB 130131A. We also searched the VLASS (Lacy et al. 2020) for radio emission at 3 GHz at the positions of the bursts, but found the non-detections to be less constraining than the radio afterglow upper limits; this holds true even for the projected total sensitivity of VLASS of the combined 3 epochs ($R_{\text{SFR}} \lesssim 30 - 2000$).

With the next generation VLA (ngVLA), we would be sensitive to radio emission at the level of $\sim 0.75 \mu\text{Jy}$ with one hour of observation at 2.4 GHz (Carilli et al. 2015)⁸. This radio flux would correspond to $\text{SFR}_{\text{Radio}} \gtrsim 0.02 - 16 M_{\odot}/\text{yr}$ for $z = 0.1 - 2.0$. With the ngVLA, we would be able to detect at least 5 of the 6 dark GRB hosts in

⁸ <https://ngvla.nrao.edu/page/performance>

our sample (with the exception of GRB 110709B, whose SFR_{SED} is $\approx 7\times$ lower than that of the ngVLA limit at the host redshift), assuming $R_{\text{SFR}} \approx 1$ (corresponding to unobscured SF). If we consider an unbiased sample of long GRBs, such as the *Swift*/BAT6 sample (Salvaterra et al. 2012), we can calculate the expected detection fraction of the long GRB host galaxies by the ngVLA. Of the 24 *Swift*/BAT6 host galaxies at $0.1 < z < 2$ with SFR_{SED} (or lower limits on SFR_{SED}) presented in Japelj et al. (2016) and Palmerio et al. (2019), we calculate a detection rate with the ngVLA of $\approx 50\%$, assuming $R_{\text{SFR}} \approx 1$. A detection rate much larger than these estimates would indicate that long GRB hosts have some amount of obscured star formation, and exact measurements of $\text{SFR}_{\text{Radio}}$ would determine the fraction of long GRB host galaxies that house significant obscured SF.

6. CONCLUSIONS

We have newly classified 2 long GRBs as dark (GRB 130420B and GRB 160509A) and presented VLA, CARMA, and PdBI afterglow observations of five dark GRBs (GRB 130131A, 130420B, 130609A, 131229A, and 140713A). We uniformly modeled the radio to X-ray afterglow of five dark GRBs with VLA detections (GRB 110709B, 111215A, 130131A, 131229A, and 140713A), using our afterglow modeling software that incorporates effects due to jet breaks, scintillation, and IC cooling, and include one dark GRB from the literature which was modeled using the same method and software. The radio detections allowed us to determine the environment and break frequencies of the synchrotron afterglow, in turn constraining the burst energetics, circumburst density, and geometries. Additionally, we fit the host galaxies of 6 dark GRBs (GRB 110709B, 111215A, 130131A, 131229A, 140713A and 160509A) using *Prospector*, and present photometric redshifts for 2 of the dark GRBs (GRB 130131A at $z \approx 1.55$ and GRB 131229A at $z \approx 1.04$). We come to the following conclusions:

- Dark GRBs are not distinct from typical long GRBs in terms of duration, burst kinetic energy, jet opening angle, or circumburst density. However, they are statistically distinct from typical long GRBs in terms of fluence, though this distinction may be attributed to observational biases and inconsistent classification of dark GRBs.
- Our sample of six uniformly modeled dark GRBs with VLA detections have line-of-sight extinction values of $A_{V,\text{GRB}} \approx 2.2 - \gtrsim 10.6$ mag, demonstrating the importance of radio observations in revealing GRBs with heavily dust-obscured sightlines.

These values are $\gtrsim 0.7$ to $\gtrsim 12.8$ times greater than their median host galaxy values $A_{V,\text{Host}} \approx 0.3 - 4.7$ mag.

- While dark GRBs do occur in dustier and more massive galaxies than typical long GRBs, the line-of-sight extinction is not strongly correlated to the median host extinction, nor to the circumburst density. This indicates that the origin of the dust along the line-of-sight is due to a clumpy, rather than uniform, dust distribution within the host galaxy. This also disfavors a dust origin from the extremely local (\sim parsec) environment of the burst.
- Targeted radio searches with $\sim \mu\text{Jy}$ sensitivity (e.g. the ngVLA) should be capable of detecting $\approx 50\%$ of long GRB host galaxies at $0.1 < z < 2$, where a higher detection rate and exact flux measurements will determine the amount of obscured SF within long GRB hosts.

Our work demonstrates the unique power of rapid-response radio observations with the VLA in uncovering the most obscured GRBs via their afterglows. This is especially important given that these events by definition have extinguished optical emission. Additionally, observations of dark GRB environments, from parsec to kiloparsec scales, lends insight on the distribution of dust and star formation in the galaxies which give rise to these relatively rare transients. Looking forward, next generation radio facilities, in conjunction with UV-optical observations, can be leveraged to determine the degree of obscured star formation for a large population of GRB environments across redshift.

7. ACKNOWLEDGEMENTS

G.S. acknowledges for this work was provided by the NSF through Student Observing Support award SOSP20B-001 from the NRAO. The Fong Group at Northwestern acknowledges support by the National Science Foundation under grant Nos. AST-1814782, AST-1909358 and CAREER grant No. AST-2047919. W.F. gratefully acknowledges support by the David and Lucile Packard Foundation. AJCT acknowledges support from the Spanish Ministry Project PID2020-118491GB-I00, Junta de Andalucía Project P20_01068 and the "Center of Excellence Severo Ochoa" award for the Instituto de Astrofísica de Andalucía (SEV-2017-0709)

The National Radio Astronomy Observatory is a facility of the National Science Foundation operated under cooperative agreement by Associated Universities, Inc. This work made use of data supplied by the UK Swift Science Data Centre at the University of Leicester. The

National Radio Astronomy Observatory is a facility of the National Science Foundation operated under cooperative agreement by Associated Universities, Inc. This work is based on observations carried out under project number S14DD004 with the IRAM NOEMA Interferometer. IRAM is supported by INSU/CNRS (France), MPG (Germany) and IGN (Spain). This research was supported in part through the computational resources and staff contributions provided for the Quest high performance computing facility at Northwestern University which is jointly supported by the Office of the Provost, the Office for Research, and Northwestern University Information Technology. W. M. Keck Observatory and MMT Observatory access was supported by Northwestern University and the Center for Interdisciplinary Exploration and Research in Astrophysics (CIERA). Some of the data presented herein were obtained at the W. M. Keck Observatory, which is operated as a scientific partnership among the California Institute of Technology, the University of California and the National Aeronautics and Space Administration. The Observatory was made possible by the generous financial support of the W. M. Keck Foundation. The authors wish to recognize and acknowledge the very significant cultural role and reverence that the summit of Maunakea has always had within the indigenous Hawaiian community. We are most fortunate to have the opportunity to conduct observations from this mountain. Some observations reported here were obtained at the MMT Observatory, a joint facility of the University of Arizona and the Smithsonian Institution. The United Kingdom Infrared Telescope (UKIRT) was supported by NASA and operated under an agreement among the University of Hawaii, the University of Arizona, and Lockheed Martin Advanced Technology Center; operations are enabled through the cooperation of the East Asian Observatory. We thank the Cambridge Astronomical Survey Unit (CASU) for processing the WFCAM data and the WFCAM Science Archive (WSA) for making the data available. This paper includes data gathered with the 6.5 meter Magellan Telescopes located at Las Campanas Observatory, Chile. The LBT is an international collaboration among institutions in the United States, Italy and Germany. The LBT Corporation partners are: The University of Arizona on behalf of the Arizona university system; Istituto Nazionale di Astrofisica, Italy; LBT Beteiligungsgesellschaft, Germany, representing the Max Planck Society, the Astrophysical Institute Potsdam, and Heidelberg University; The Ohio State University; The Research Corporation, on behalf of The University of Notre Dame, University of Minnesota and University of Virginia. IRAF is distributed by the National Optical As-

tronomy Observatory, which is operated by the Association of Universities for Research in Astronomy (AURA) under a cooperative agreement with the National Science Foundation. This publication makes use of data products from the Two Micron All Sky Survey, which is a joint project of the University of Massachusetts and the Infrared Processing and Analysis Center/California Institute of Technology, funded by the National Aeronautics and Space Administration and the National Science Foundation.

Facilities: VLA, CARMA, PdBI, Swift, Keck:LRIS, Keck:MOSFIRE, LBT:LBC, MMT:MMIRS, MMT:Binospic, UKIRT:WFCAM, Magellan:LDSS3, Magellan:Fourstar, Spitzer:IRAC

Software: CASA (McMullin et al. 2007), Miriad (Sault et al. 1995), pwkit (Williams et al. 2017a), scipy (Virtanen et al. 2020), matplotlib (Hunter 2007), pandas (Mckinney 2010), numpy (van der Walt et al. 2011), Prospector (Leja et al. 2017)

Table 1. *Swift*/XRT Properties

GRB	R.A. (J2000)	Dec. (J2000)	90% Error ($''$)	T_{90} (15-350 keV) (s)	f_{γ} (15-150 keV) ($\times 10^{-7}$ erg/cm 2)
130131A	11 ^h 24 ^m 30.31 ^s	+48°04′32.9 $''$	1.4	51.52	3.1 ± 0.6
130420B	12 ^h 12 ^m 30.79 ^s	+54°23′26.3 $''$	2.0	12.64	7.2 ± 0.5
130609A	10 ^h 10 ^m 40.44 ^s	+24°07′56.6 $''$	1.7	7.06	5.7 ± 0.4
131229A	05 ^h 40 ^m 55.62 ^s	−04°23′46.8 $''$	1.4	48.0	68.9 ± 1.5
140713A	18 ^h 44 ^m 25.41 ^s	+59°38′00.5 $''$	1.4	6.02	3.7 ± 0.3

NOTE—*Swift*/XRT Properties from Evans et al. (2009); Lien et al. (2016).

APPENDIX

A. OBSERVATIONS

Here we present the X-ray to radio afterglow observations of the 8 dark GRBs in our sample, as well as their host galaxy observations. For the five dark GRBs with no previously published VLA observations, we summarize the Neil Gehrels *Swift* Observatory (*Swift*) X-ray Telescope (XRT) properties in Table 1. Unless otherwise stated, all VLA data were manually reduced using standard procedures with the Common Astronomy Software Applications (CASA, McMullin et al. 2007), and all Combined Array for Research in Millimeter Astronomy (CARMA) data were manually reduced using standard procedures with the *Miriad* software package (Sault et al. 1995). For VLA and CARMA observations, we measure the flux density and position of the afterglow using the *imtool* program under the *pwkit* package, which fits the afterglow to a point source (Williams et al. 2017b). The radio observations, including the configuration, gain, bandpass, and flux, calibrators, are summarized in Table A2.

A.1. GRB 130131A

A.1.1. *Swift* and Optical Observations

GRB 130131A was discovered by the Burst Alert Telescope (BAT) on-board *Swift* on 2013 January 31.58 (Grupe et al. 2013). The XRT started observations of GRB 130131A at $\delta t = 58.5$ s (where δt is the time after BAT trigger), finding an uncatalogued X-ray source

within the BAT position (Grupe et al. 2013; Evans et al. 2013).

An uncatalogued, fading, optical/near-infrared (NIR) source was found within the XRT error circle at $\delta t \approx 0.02 - 0.04$ days in *R*-, *J*-, and *K*-band, and was determined to be the optical/NIR afterglow after the source faded by $\gtrsim 2$ mag in *K*-band by $\delta t \approx 0.85$ days (Volnova et al. 2013; Tanvir et al. 2013a,b). We initiated MMT SAO Widefield InfraRed Camera (SWIRC) observations at $\delta t \approx 0.67$ days in *J*- and *H*-band and detected a source coincident with the optical/NIR afterglow (Volnova et al. 2013; Tanvir et al. 2013a,b) in both bands. For photometric calibration, we use sources in the field in common with the 2MASS catalog, and perform aperture photometry using IRAF. We find afterglow magnitudes of 21.9 ± 0.1 mag in *J*-band and 21.2 ± 0.1 mag in *H*-band at a position of R.A.=11^h 24^m 30.35^s and Dec=+48°04′33.08 $''$ with a positional uncertainty of 0.10 $''$.

Interpolating the XRT light curve to the times of the *R*-band observations, we find $\beta_{\text{OX}} \approx -0.2$ at 0.016 days and 0.041 days, meeting the Jakobsson et al. (2004) criterion and confirming the darkness classification first asserted by Volnova et al. (2013). We find $\beta_{\text{X}} = -1.4_{-0.2}^{+0.3}$, and therefore, $\beta_{\text{OX}} - \beta_{\text{X}} > 0.5$ for the *R*-band detections, indicating that GRB 130131A also meets the van der Horst et al. (2009) darkness criterion.

A.1.2. Radio Afterglow Discovery

Table A2. Radio Afterglow Observations of Dark GRBs

GRB	Facility	Config.	Mid-time (UT)	δt (d)	Gain/Band-pass/Flux (Calibrators)	ν (GHz)	F_ν (μ Jy)
130131A	VLA	D	2013 Feb 1.27	0.68	J1146+3958/3C286/3C286	6.0	29.4 ± 8.1
					J1153+4931/3C286/3C286	19.2	124.0 ± 31.6
						24.5	142.3 ± 26.5
			2013 Feb 2.59	1.99	J1146+3958/3C286/3C286	6.0	$< 27.3^a$
					J1153+4931/3C286/3C286	19.2	116.3 ± 13.7
						24.5	116.2 ± 17.3
	2013 Feb 5.28	4.68	J1146+3958/3C286/3C286	6.0	54.2 ± 10.5		
			J1153+4931/3C286/3C286	19.2	63.1 ± 18.4		
				24.5	< 47.4		
	2013 Feb 14.47	13.88	J1146+3958/3C286/3C286	6.0	< 28.5		
			J1153+4931/3C286/3C286	19.2	< 20.4		
				24.5	< 25.8		
CARMA	B	2013 Feb 1.45	0.67	1153+495/0927+390/Jupiter	85.5	< 230	
		2013 Feb 2.49	1.91	1153+495/3C273/3C273	85.5	< 235	
		2013 Feb 3.40	2.82		85.5	< 491	
130420B	VLA	D	2013 Apr 23.32	2.78	J1219+4829/3C286/3C286	6.0	< 22.8
			2013 Apr 23.32	2.78		21.8	< 34.8
	CARMA	C	2013 Apr 23.14	2.60	1153+495/0927+39/3C84	85.5	< 436
130609A	VLA	C	2013 Jun 9.9	0.78	J0956+2515/3C147/3C147	6.0	< 28.5
			2013 Jun 9.9	0.78		21.8	< 38.4
	CARMA	D	2013 Jun 10.15	1.02	0956+252/0927+390/0854+201	85.5	< 341
131229A	VLA	B	2013 Dec 30.18	0.91	J0541-0541/J0541-0541/J0541-0541	6.0	74 ± 19
			2013 Dec 30.18	0.91		21.8	< 45.6
140713A	VLA	D	2014 Jul 17.12	3.34	J1927+6117/3C286/3C286	13.4	779.4 ± 35.2
						15.9	872.6 ± 37.3
			2014 Jul 17.14	3.36		4.9	94.3 ± 24.3
						7.0	119.5 ± 18.4
			2014 Jul 20.11	6.33		13.4	739.1 ± 47.0
						15.9	901.9 ± 73.3
			2014 Jul 20.13	6.35		4.9	111.8 ± 20.3
						7.0	237.5 ± 15.1
		2014 Jul 26.08	12.30		13.4	2149.6 ± 38.6	
					15.9	2274.0 ± 35.0	
		2014 Jul 26.1	12.32		4.9	219.5 ± 18.8	
					7.0	897.8 ± 21.9	

Table A2 *continued*

Table A2 (*continued*)

GRB	Facility	Config.	Mid-time (UT)	δt (d)	Gain/Band-pass/Flux (Calibrators)	ν (GHz)	F_ν (μJy)
			2014 Aug 8.05	25.27		13.4	950.3 ± 22.0
						15.9	931.5 ± 21.9
			2014 Aug 8.07	25.29		4.9	130.2 ± 27.9
						7.0	150.0 ± 15.2
			2014 Aug 28.04	45.26		13.4	267.0 ± 16.0
						15.9	229.6 ± 14.7
			2014 Aug 28.06	45.28		4.9	315.6 ± 14.2
						7.0	379.1 ± 39.7
			2014 Sep 14.97	63.19		13.4	159.1 ± 14.3
						15.9	118.2 ± 19.7
			2014 Sep 14.99	63.21		4.9	100.5 ± 13.1
						7.0	116.5 ± 26.8
	PdBI	D	2014 Jul 18.16	4.38	-/-/MWC349	86.7	3180.0 ± 90.0
			2014 Jul 28.97	15.19		86.7	1030.0 ± 110.0
			2014 Aug 12.08	29.3		86.7	260.0 ± 130.0
			2014 Aug 14.04	31.26		86.7	190.0 ± 80.0
			2014 Sep 14.85	63.07		86.7	< 210.0
	CARMA	E	2014 Jul 15.37	1.59	1849+670/1927+739/MWC349	85.5	1506.8 ± 255.0
			2014 Jul 17.28	3.50		85.5	3863.9 ± 297.2
			2014 Jul 18.41	4.63		85.5	3008.0 ± 302.3
			2014 Jul 20.18	6.40	1849+670/1512-090/MWC349	85.5	2396.6 ± 332.3
			2014 Jul 22.37	8.59	1849+670/1927+739/MWC349	85.5	2072.9 ± 215.0
			2014 Jul 26.32	12.54		85.5	1529.3 ± 198.6
			2014 Aug 11.14	28.36	1849+670/3C279/MWC349	85.5	< 670.2

NOTE—All listed data are new to this work. Our modeling is supplemented by radio data from [Perley \(2013\)](#); [Chandra & Nayana \(2014b\)](#); [Anderson et al. \(2018\)](#); [Higgins et al. \(2019\)](#)

^a Upper limits correspond to 3σ .

We initiated a series of four observations of GRB 130131A starting on 2013 February 1.28 UT with the VLA under Program 13A-046 (PI: E. Berger) at 6.0 GHz and 21.8 GHz (side-band frequencies of 19.2 GHz and 24.5 GHz). We detect a clear source within the XRT error circle with 3.6σ significance of $\approx 29.4 \mu\text{Jy}$ at 6.0 GHz (the information presented here supersedes the information from a preliminary reduction reported in [Laskar et al. 2013b](#)). We took further VLA 6.0 GHz and 21.8 GHz observations until 2013 February 14.47 UT. The first 3 epochs of observations were taken with 8-bit sampling, while we used 3-bit sampling for the

final 21.8 GHz observations to improve sensitivity. Due to the increased complexity of the 3-bit observations, we used the CASA VLA pipeline (version 2020.1.0.36) for the reduction ([McMullin et al. 2007](#)). The details of the VLA observations are listed in Table A2. Using the observation with the highest signal to noise (the second 21.8 GHz epoch), we derive a position for the radio afterglow of R.A.= $11^{\text{h}} 24^{\text{m}} 30.401^{\text{s}}$ ($\pm 0.739''$) and Dec= $+48^{\circ} 04' 33.15''$ ($\pm 0.357''$).

We initiated a series of three observations of GRB 130131A starting on 2013 February 1.45 UT using CARMA under program number c0999 (PI: A. Za-

uderer). We observed the field at a mean frequency of 85.5 GHz and do not detect a source to a 3σ limit of $\lesssim 230 \mu\text{Jy}$ (the information presented here supercedes the marginal detection reported in Zauderer et al. 2013a). We took further observations until 2013 February 3.40 UT, with no significant detection. The details of the CARMA observations are listed in Table A2.

A.1.3. Host Galaxy Observations

The faint host galaxy of GRB 130131A was first reported in Chrimes et al. (2019), within the XRT position (Evans et al. 2009). We initiated *griz*-band observations of the host galaxy on 2015 December 3 UT with the Large Binocular Camera (LBC) on the Large Binocular Telescope (LBT/LBC) atop Mount Graham, Arizona. We reduced these images using standard routines in the IRAF/ccdproc package (Tody 1986, 1993). We applied bias and flat-field corrections and co-added the dithered images in each filter. We performed absolute astrometry with IRAF/ccmap and ccsetwcs using sources in common with the SDSS DR12 catalog (Alam et al. 2015). Using SExtractor (Bertin & Arnouts 1996), we measure a position of the host: R.A.=11^h 24^m 30.317^s and Dec =+48°04′33.32″. The radio and NIR afterglows are at projected offsets of 0.857″ and 0.401″ from the host, respectively (Figure 1).

We initiated NIR *YJHK*-band observations of the host galaxy in 2016 March, 2020 December, and 2021 January using the Wide-field Camera (WFCAM; Casali et al. 2007) mounted on the 3.8-m United Kingdom Infrared Telescope (UKIRT) and the MMT and Magellan Infrared Spectrograph (MMIRS) on the MMT telescope. For UKIRT data, we obtained pre-processed images from the WFCAM Science Archive (Hamly et al. 2008), which are corrected for bias, flat-field, and dark current by the Cambridge Astronomical Survey Unit⁹. For each filter, we co-added the images and performed astrometry relative to 2MASS using a combination of tasks in Starlink¹⁰ and IRAF. For MMIRS data, we used a custom pipeline, POTPyRI¹¹, to perform bias, flat-fielding, dark corrections, sky subtraction, and co-addition.

The host galaxy is detected in all bands. We performed aperture photometry of the host using IRAF/phot with a source radius of $2.5 \times \theta_{\text{FWHM}}$ and a background annulus immediately surrounding the host. For photometric calibration, we use sources in the field in common with the SDSS DR12 and 2MASS catalogs

and employ the standard Vega to AB conversions as necessary. The host galaxy is faint, with $r \approx 23.6$ mag, but with red colors ($r - J \approx 1.7$ mag). Our full photometric results are listed in Table A3. Using the projected offset from the radio and optical afterglows and the *r*-band magnitude, we calculate a probability of chance coincidence (Bloom et al. 2002), $P_{cc} \approx 0.003 - 0.007$, establishing a robust association with GRB 130131A.

We obtained 2×1200 s of spectroscopy with the Multi-Object Double Spectrograph (MODS) mounted on the LBT on 2015 December 4 UT with the 200l grating, to cover a wavelength range of $\lambda \approx 3200 - 10000 \text{ \AA}$. The spectral continuum is weakly detected with an average $S/N \approx 1.2$. The spectrum does not exhibit any obvious features to $\lambda \approx 10000 \text{ \AA}$, yielding a tentative lower limit on the redshift of $z \gtrsim 1.3$ (due to the absence of [OII] $\lambda 3727$). This is consistent with the redshift upper limit of $z \lesssim 4$ from the detection of the host in the *HST* F160W and F606W bands (Chrimes et al. 2019).

The host galaxy is well detected in *Spitzer*/IRAC 3.6 μm and 4.5 μm observations taken on 2016 July 17 (PI: Perley). We downloaded the pipeline processed post-basic calibrated data (pbcd) mosaics and performed photometry using a 3″ aperture and 3″–7″ background annulus, masking nearby bright sources from the background region. We applied standard aperture corrections¹², and obtain host magnitudes of ≈ 21.2 mag and ≈ 21.0 mag at 3.6 μm and 4.5 μm , respectively.

A.2. GRB 130420B

A.2.1. Swift and Optical Observations

GRB 130420B was discovered by BAT on 2013 April 20.54 (Oates et al. 2013). The XRT started observations of GRB 130420B at $\delta t = 54.5$ s, finding an uncatalogued X-ray source within the BAT position (Oates et al. 2013). Ground-based follow-up at optical wavelengths to search for the optical afterglow of GRB 130420B reached limiting magnitudes of $R > 22.6$ mag at a mean time of $\delta t \approx 0.02$ days using the 2.4m Gao-Mei-Gu (GMG) telescope (Zhao et al. 2013). We interpolate the X-ray light curve to the time of the most constraining optical limit, and we calculate $\beta_{\text{OX}} \gtrsim -0.35$, meeting the criterion of a dark burst as determined by Jakobson et al. (2004). We find $\beta_{\text{X}} = -0.8 \pm 0.2$, leading to $\beta_{\text{OX}} - \beta_{\text{X}} \gtrsim 0.45$, which does not meet the darkness criteria of van der Horst et al. (2009), due to GRB 130420B’s shallow β_{X} .

⁹ <http://casu.ast.cam.ac.uk/>

¹⁰ <http://starlink.eao.hawaii.edu/starlink>

¹¹ <https://github.com/CIERA-Transients/POTPyRI>

¹² https://irsa.ipac.caltech.edu/data/SPITZER/docs/irac/calibrationfiles/ap_corr_warm/

Table A3. Host Galaxy Observations

GRB	Date (UT)	Telescope/Instrument	Filter	Exposure Time (s)	Magnitude (AB)	A_λ (AB)	Reference
130131A	2015-12-03	LBT/LBC	g	8×300	24.01 ± 0.076	0.052	This work
	2014-10-09	HST/WFC3	F606W	1101	24.089 ± 0.037	0.039	Chrimes et al. (2019)
	2015-12-03	LBT/LBC	r	6×300	23.58 ± 0.085	0.036	This Work
	2015-12-03	LBT/LBC	i	12×150	23.19 ± 0.075	0.027	
	2015-12-03	LBT/LBC	z	16×150	22.89 ± 0.097	0.020	
	2020-12-26	MMT/MMIRS	Y	20×60	22.633 ± 0.178	0.017	
	2016-03-18	UKIRT/WFCAM	J	36×60	21.839 ± 0.191	0.011	
	2016-03-18	UKIRT/WFCAM	H	36×60	21.817 ± 0.226	0.007	
	2021-01-08	MMT/MMIRS	K	20×60	22.0821 ± 0.130	0.005	
	2014-10-09	HST/WFC3	F160W	1059	21.889 ± 0.022	0.008	Chrimes et al. (2019)
	2016-07-17	Spitzer/IRAC	$3.6\mu\text{m}$	36×100	21.167 ± 0.01	0.002	This work
	2016-07-17	Spitzer/IRAC	$4.5\mu\text{m}$	36×100	20.968 ± 0.01	-	
130420B	2020-11-23	MMT/Binospec	r	12×120	> 24.2	0.038	This work
130609A	2020-11-20	MMT/Binospec	r	62×30	\dots †	0.074	This work
	2020-12-01	MMT/MMIRS	J	30×60	\dots †	0.023	
131229A	2014-10-22	LBT/LBC	g	2×300	> 24.9	0.892	This work
	2014-08-14	HST/WFC3	F606W	1125	> 25.8	0.672	Chrimes et al. (2019)
	2014-10-22	LBT/LBC	r	5×300	> 24.7	0.617	This Work
	2014-10-22	LBT/LBC	i	10×150	> 24.6	0.459	
	2014-10-22	LBT/LBC	z	4×150	> 23.2	0.341	
	2013-12-29	Magellan/LDSS3	z	7×180	> 23.96	0.341	Chornock et al. (2013b) ^a
	2020-01-08	MMT/MMIRS	Y	90×60	23.260 ± 0.192	0.294	This Work
	2015-03-29	Magellan/Fourstar	J	22×61	23.382 ± 0.381	0.191	
	2014-08-14	HST/WFC3	F160W	1209	23.235 ± 0.077	0.138	Chrimes et al. (2019)
2015-03-30	Magellan/Fourstar	K_s	198×11.6	22.949 ± 0.285	0.082	This work	
140713A	2014-10-23	LBT/LBC	g	300×3	24.12 ± 0.09	0.16	This work
	2014-10-23	LBT/LBC	r	300×4	23.85 ± 0.19	0.11	
	2014-10-23	LBT/LBC	i	150×8	22.65 ± 0.09	0.08	
	2014-10-23	LBT/LBC	z	150×6	22.36 ± 0.12	0.06	
	2018-10-18	Keck/MOSFIRE	J	60×27	21.93 ± 0.16	0.04	
	2018-10-18	Keck/MOSFIRE	K_s	60×29	21.69 ± 0.18	0.02	
	2016-11-08	Spitzer/IRAC	$3.6\mu\text{m}$	36×100	21.45 ± 0.05	0.01	Higgins et al. (2019)
	2016-11-08	Spitzer/IRAC	$4.5\mu\text{m}$	36×100	21.82 ± 0.05	-	
160509A	2016-06-07	Keck/LRIS	g'	3×330	24.434 ± 0.12	0.956	Laskar et al. (2016)
	2016-06-07	Keck/LRIS	r'	3×300	23.519 ± 0.35	0.661	
	2017-07-05	HST/WFC3	F110W	2697	22.565 ± 0.03	0.255	This Work
	2017-07-05	HST/WFC3	F160W	2797	22.292 ± 0.03	0.148	
	2017-11-05	Spitzer/IRAC	$3.6\mu\text{m}$	32×93.6	19.5172 ± 0.041	0.047	

NOTE—All values are in AB magnitudes and are corrected for the Galactic extinction, A_λ , in the direction of the burst (Schlafly & Finkbeiner 2011).

^a We use this z -band limit in our host galaxy modeling as it is the most constraining for this burst (see Section 4) † No host identified.

A.2.2. Radio and Millimeter Observations

We initiated observations of GRB 130420B on 2013 April 23.14 ($\delta t \approx 2.60$ days) with CARMA under program number c0999 (PI: A. Zauderer) at a mean frequency of 85.5 GHz. We do not detect any source within the XRT error circle to a 3σ limit of $< 436 \mu\text{Jy}$ (the information presented here supercedes the information from a preliminary reduction reported in Zauderer & Berger 2013).

We initiated observations of GRB 130420B on 2013 April 23.32 ($\delta t \approx 2.78$ days) with the VLA under program 13A-046 (PI: E. Berger) at 6.0 GHz and 21.8 GHz. We do not detect a source within the XRT error circle to a 3σ limit of $< 22.8 \mu\text{Jy}$ at 6.0 GHz and $< 34.8 \mu\text{Jy}$ at 21.8 GHz (the information presented here supercedes the information from a preliminary reduction reported in Zauderer & Berger 2013).

A.2.3. Host Galaxy Search

We obtained MMT/Binospec r -band observations of the field of GRB 130420B in Nov 2020. While there is a point source directly to the west of the XRT position (Evans et al. 2009), we do not detect any source within the XRT position (90% confidence) to a 3σ limit of $r \gtrsim 24.2$ mag. The Binospec image is shown in Figure 1.

A.3. GRB 130609A

A.3.1. Swift and Optical Observations

GRB 130609A was discovered by BAT (Cummings et al. 2013). XRT started observations at $\delta t = 66.8$ s, finding an uncatalogued X-ray source within the BAT position (Cummings et al. 2013). Deep optical and NIR observations to search for the afterglow of GRB 130609A were taken at a mean time of $\delta t \approx 0.07$ days, using the Reionization and Transients Infrared Camera (RATIR) in the $r'i'ZYJH$ -bands, reaching limits of > 23.34 mag to > 21.06 mag in r' - and H -band, respectively (Butler et al. 2013). We interpolate the X-ray light curve to the time of the most constraining optical limit ($i' > 23.27$ mag at $\delta t \approx 0.07$ days), and we calculate $\beta_{\text{OX}} \gtrsim 0.49$, meeting the criterion of a dark burst as determined by Jakobsson et al. (2004), and confirming the classification suggested by Perley & Cenko (2013). We find $\beta_{\text{X}} = -1.5 \pm 0.2$, leading to $\beta_{\text{OX}} - \beta_{\text{X}} \gtrsim 1.00$, confirming GRB 130609A is also dark according to the criterion of van der Horst et al. (2009).

A.3.2. Radio and Millimeter Observations

We initiated observations of GRB 130609A on 2013 June 9.9 UT ($\delta t \approx 0.78$ days) with the VLA under program 13A-046 (PI: E. Berger) at 6.0 GHz and 21.8 GHz. We do not detect a source within the XRT error circle

to a 3σ limit of $< 28.5 \mu\text{Jy}$ at 6.0 GHz and $< 38.4 \mu\text{Jy}$ at 21.8 GHz (Zauderer et al. 2013b).

We initiated observations of GRB 130609A on 2013 June 10.15 ($\delta t \approx 1.02$ days) with CARMA under program number c0999 (PI: A. Zauderer) at a mean frequency of 85.5 GHz. We do not detect any source within the XRT error circle to a 3σ limit of $< 341 \mu\text{Jy}$ (the information presented here supercedes the information from a preliminary reduction reported in Zauderer et al. 2013b).

A.3.3. Host Galaxy Search

We obtained deep MMT/Binospec r -band and MMIRS J -band observations of the field of GRB 130609A in Nov and Dec 2020 to search for a host galaxy. The r -band imaging reveals a source within the XRT position (Evans et al. 2009) with $r = 23.29 \pm 0.11$ mag; this source is also weakly detected in J -band (labeled “S1” in Figure 1). However, this source has a PSF consistent with being point-like, indicating that it is a foreground star. We identify a second, fainter source to the northwest of the XRT position (labeled “S2” in Figure 1) with $r = 24.48 \pm 0.14$ mag that is more clearly extended and is a potential host of GRB 130609A. Thus, it is difficult to draw any strong conclusions regarding the origin or redshift of GRB 130609A.

A.4. GRB 131229A

A.4.1. X-ray and Optical Observations

GRB 131229A was discovered by BAT on 2013 December 29.28 (Page et al. 2013). The XRT started observations of GRB 131229A at $\delta t = 93.8$ s, finding an uncatalogued X-ray source within the BAT position (Page et al. 2013). We initiated deep optical ground-based observations to search for the optical afterglow of GRB 131229A with the 6.5 m Magellan Clay telescope in $r'i'z'$ -bands at a mean time of $\delta t \approx 0.03$ days, reaching $z' > 24.3$ mag (Chornock et al. 2013b). We interpolate the X-ray light curve to the time of the most constraining optical limit, and we calculate $\beta_{\text{OX}} \gtrsim 0.24$, meeting the criterion of a dark burst as determined by Jakobsson et al. (2004), and confirming the classification of Chrimes et al. (2019). We find $\beta_{\text{X}} = -1.2 \pm 0.1$, leading to $\beta_{\text{OX}} - \beta_{\text{X}} \gtrsim 1.41$, confirming GRB 131229A is also dark according to the criterion of van der Horst et al. (2009).

Chandra observations of GRB 131229A (PI: Levan, ObsID 15195) were initiated at a midtime of 2014 Jan 06.12 ($\delta t = 7.84$ days) with a total effective exposure time of 15.05 ks. The X-ray afterglow was detected with a count rate of $(1.06 \pm 0.15) \times 10^{-3} \text{ s}^{-1}$ (Chrimes et al. 2019).

A.4.2. Radio and Millimeter Observations

We initiated observations of GRB 131229A on 2013 December 30.18 ($\delta t \approx 0.91$ days) with the VLA under program 13A-541 (PI: E. Berger) at 6.0 GHz and 21.8 GHz. We do not detect a source within the XRT error circle at 21.8 GHz to a 3σ limit of $< 45.6 \mu\text{Jy}$. We detect a clear source within the XRT error circle of 3.9σ significance of $74 \mu\text{Jy}$ at 6.0 GHz at a position of R.A.= $05^{\text{h}} 40^{\text{m}} 55.649^{\text{s}}$ ($\pm 0.093''$) and Dec= $-04^{\circ} 23' 47.098''$ ($\pm 0.115''$). We did not re-observe the field, and thus the variability of the source could not be determined, therefore we cannot definitively claim this source as the radio afterglow of GRB 131229A. To place limits on the presence of a background radio source, we searched the VLA Sky Survey (VLASS, Lacy et al. 2020), and found no source within the XRT localization to a limit of $\lesssim 420 \mu\text{Jy}$ at 3.0 GHz (with observations taken $\delta t \approx 3.9$ yr).

GRB 131229A was observed with CARMA at 93.0 GHz at a mean time of $\delta t \approx 1.00$ days after the burst. No millimeter afterglow emission was found within the XRT error circle to a limit of $\lesssim 0.6$ mJy (Perley 2013).

A.4.3. Host Galaxy Observations

The faint host galaxy of GRB 131229A was first reported in Chrimes et al. (2019) from *HST*/F160W imaging, and it is the only detected object within the 90% XRT position (Figure 1, Evans et al. 2009). We obtained observations of the field with LBT/LBC (*griz*-bands), MMT/MMIRS (*Y*-band), and Magellan/Fourstar (*JK*-bands). We reduced and co-added the data in a similar manner as described before. The host galaxy is not detected in any of our optical imaging to deep limits of $\gtrsim 23.2 - 24.9$ mag, and is weakly detected in our *Y*, *J* and *K*-band imaging with $K = 22.95 \pm 0.29$ mag. Overall, the host is red, with $r - K \gtrsim 1.8$ mag, is at a $0.41''$ offset from the VLA position and has a $P_{cc} = 1.5 \times 10^{-3}$. Our full photometric results are listed in Table A3. From the *K*-band image, we measure a position for the host of R.A.= $5^{\text{h}} 40^{\text{m}} 55.632^{\text{s}}$ and Dec= $-4^{\circ} 23' 46.77''$. The deep non-detection of the host in the *i*-band, coupled with a brightness at *Y*-band that is $\gtrsim 1.3$ mag brighter, suggest a 4000\AA break in this wavelength regime, with a redshift of $z \gtrsim 1 - 1.5$.

To place the *Chandra* afterglow on the host galaxy image, we perform relative astrometry using three common sources between *Chandra* and Magellan *K*-band. We obtained the *Chandra* observation from the archive (PI: Levan; ObsID 15195). We find a tie uncertainty of $\sigma_{\text{Magellan} \rightarrow \text{Chandra}} = 0.13''$. The corrected position is R.A. = $05^{\text{h}} 40^{\text{m}} 55.64^{\text{s}}$ and Dec. = $-04^{\circ} 23' 46.824''$ with

a positional uncertainty of $0.63''$ (including the uncertainty in the astrometric tie, the positional uncertainty, and the absolute astrometric uncertainty of $0.6''$). Our *Chandra* afterglow position is consistent with the VLA C-band afterglow position and intersects the host galaxy of GRB 131229A (Figure 1).

A.5. GRB 140713A

A.5.1. Swift and Optical Observations

GRB 140713A was discovered by BAT on 2014 July 13.78 (Mangano et al. 2014). The XRT began observations starting at $\delta t = 72.8$ s, detecting an uncatalogued X-ray source within the BAT position (Mangano et al. 2014; Beardmore et al. 2014). Deep optical observations to search for the optical afterglow using the ALFOSC instrument on the 2.5-m Nordic Optical Telescope (NOT) were taken at $\delta t \approx 0.14 - 0.17$ days, resulting in 3σ upper limits on the afterglow flux of $r \gtrsim 24.30$ mag, $i \gtrsim 23.50$ mag, and $z \gtrsim 22.60$ mag (Cano et al. 2014; Higgins et al. 2019). We interpolate the X-ray light curve to the time of the deepest optical limit ($r > 24.30$ mag at $\delta t \approx 0.15$ days), and we calculate $\beta_{\text{OX}} \gtrsim -0.26$, meeting the criterion of a dark burst as determined by Jakobsson et al. (2004), and confirming the classification of Higgins et al. (2019). We find $\beta_{\text{X}} = -1.0 \pm 0.2$, leading to $\beta_{\text{OX}} - \beta_{\text{X}} \gtrsim 0.73$, indicating GRB 140713A also meets the darkness criterion of van der Horst et al. (2009).

A.5.2. Radio and Millimeter Observations

We initiated a series of seven observations of GRB 140713A starting on 2014 July 15.37 UT ($\delta t \approx 1.59$ days) until 2014 August 11.14 UT ($\delta t \approx 28.36$ days) with CARMA under program number c0999 (PI: A. Zauderer) at a mean frequency of 85.5 GHz. In the first observation, we detect a clear source within the XRT error circle of 5σ significance of ≈ 1.5 mJy; the information presented here supercedes the information from a preliminary reduction reported in Zauderer et al. (2014). We report the CARMA afterglow flux densities in Table A2. We obtain a position for the millimeter afterglow of GRB 140713A of R.A.= $18^{\text{h}} 44^{\text{m}} 25.403^{\text{s}}$ ($\pm 1.489''$) and Dec= $+59^{\circ} 38' 00.97''$ ($\pm 0.781''$).

We initiated a series of six observations of GRB 140713A from 2014 July 17.08 UT ($\delta t \approx 3.36$ days) to 2014 September 15.00 UT ($\delta t \approx 63.21$ days), with the VLA (Program number 14A-344, PI: Berger) at 6.0 GHz (side-band frequencies of 4.9 GHz and 7.0 GHz) and 14.7 GHz (side-band frequencies of 13.4 GHz and 15.9 GHz) for all observations. In the first observation, we detected a source within the XRT error circle, and consistent with the CARMA position, with $F_{\nu} \approx 0.10$ mJy

at 6.0 GHz and $F_\nu \approx 0.82$ mJy at 14.7 GHz. Using the observation with the highest signal to noise (the third 14.7 GHz epoch), we derive a position for the radio afterglow of R.A.=18^h 44^m 25.481^s ($\pm 0.149''$) and Dec=+59°38'00.69'' ($\pm 0.052''$), an improvement on our CARMA position.

In addition, we initiated observations of GRB 1407134A with the Plateau deBure Interferometer (PdBI) at 86.7 GHz as part of a long-term ToO program (Program number S14DD004, PI: A. Castro-Tirado). The PdBI observed the source at six separate epochs across 2014 Jul 18-Sep 14 UT ($\delta t \approx 4.4 - 63.1$ days). We reduced the data with the standard CLIC and MAPPING software distributed by the Grenoble GILDAS group¹³, and use the carbon star MWC349 as the flux calibrator. We detect a source in all epochs except the final epoch, at a position consistent with the millimeter and radio afterglows. The flux measurements of these observations are listed in Table A2.

To supplement our CARMA, VLA, and PdBI data, we include literature data in our subsequent analysis from the Arcminute Microkelvin Imager (AMI) Large Array (mean frequency of 15.7 GHz) (Anderson et al. 2014, 2018), 1.4 GHz and 4.8 GHz observations from the Westerbork Synthesis Radio Telescope (WSRT) (Higgins et al. 2019), and 1.4 GHz upper limits from the Giant Metrewave Radio Telescope (GMRT) (Chandra & Nayana 2014b). The AMI and WSRT afterglow observations, along with the NOT optical upper limits, were previously modeled alongside the *Swift* X-ray light curve in Higgins et al. (2019), but the VLA, CARMA, and PdBI observations are presented and modeled for the first time in this work.

A.5.3. Host Galaxy Observations

Observations by the 10.4m Gran Telescopio CANARIAS (GTC) telescope at $\delta t \approx 3.1$ days revealed a faint, $r \approx 24$ mag source as the candidate host galaxy (Castro-Tirado et al. 2014). Identification and further analysis of this source was also provided in Higgins et al. (2019). We initiated *griz*-band observations of the host galaxy with the Large Binocular Camera (LBC) on the Large Binocular Telescope (LBT/LBC) on 2014 Oct 23 UT. We reduced and co-added the data in a similar manner as described before. We calibrated the absolute astrometry using sources in common with the Pan-STARRS1 catalog (Chambers et al. 2016) using IRAF/*ccmap* and *ccsetwcs*. We performed aperture photometry on these images using IRAF/*phot* using a source radius of $2.5 \times \theta_{\text{FWHM}}$ and a background annulus

at the host position. For photometric calibration, we use standard stars from PAN-STARRS1 in the field (Chambers et al. 2016), and then convert to the SDSS system using standard transformations Tonry et al. (2012). We find a host magnitude of $r = 23.8 \pm 0.2$ mag, and the host galaxy photometry in all bands is listed in Table A3.

In addition, we initiated *J* and *K_s*-band NIR observations of the host galaxy in Oct 2018 using the Multi-Object Spectrometer for Infra-Red Exploration (MOS-FIRE) instrument mounted on the Keck I telescope (PI: Fong). We used POTPyRI¹⁴ to perform bias, flat-fielding, dark corrections, sky subtraction, and co-addition. We calibrated the absolute astrometry to 2MASS using IRAF/*ccmap* and *ccsetwcs*. The host galaxy is well detected in each of the NIR bands. We calibrated to 2MASS, and converted to the AB system (Blanton & Roweis 2007); The magnitude values are listed in Table A3.

We obtained 3×1800 s of host galaxy spectroscopy using the Low Resolution Imaging Spectrometer (LRIS) mounted on the 10m Keck I telescope on 2018 October 6 UT. We used the 400/3400 grism and 400/8500 grating in combination with the D560 dichroic for an effective wavelength range of $\sim 3200\text{-}10100\text{\AA}$. The raw frames were corrected for bias from the overscan region, flattened, and stitched together using custom methods implemented in *pyraf*¹⁵. We then extracted one-dimensional spectra of the host galaxy and applied a dispersion correction derived from arc-lamp spectra. Finally, we applied an atmospheric absorption correction and flux calibration derived from a spectrum of the spectrophotometric standard GD71 obtained on the same night. We detect a faint continuum ($S/N \sim 10$) with several clear emission features. We identify [OII] $\lambda 3727$, $H\beta\lambda 4861$, and [OIII] $\lambda 5007$ at a common redshift of $z = 0.935 \pm 0.002$. The spectrum is shown in Figure 8.

To supplement our optical and NIR host galaxy observations, we include 3.6 and 4.5 μm observations from *Spitzer*/IRAC photometry, published in Higgins et al. (2019) (Table A3). Our *grizJHK_s* data, as well as the available *Spitzer* photometry are subsequently used in our host galaxy modeling.

A.6. Literature Bursts

A.6.1. GRB 110709B

We gather radio and optical afterglow observations of GRB 110709B from Zauderer et al. (2013c) and X-ray afterglow observations from *Swift*. GRB 110709B has been

¹³ <https://www.iram.fr/IRAMFR/GILDAS>

¹⁴ <https://github.com/CIERA-Transients/POTPyRI>

¹⁵ https://github.com/msiebert1/UCSC_spectral_pipeline

previously been determined to be a dark burst through the $\beta_{\text{OX}} > -0.5$ criterion (Jakobsson et al. 2004) in Zauderer et al. (2013c). We gather host galaxy observations of GRB 110709B from Zauderer et al. (2013c), Perley et al. (2016a), and Selsing et al. (2019).

A.6.2. GRB 111215A

We gather radio and optical afterglow observations of GRB 111215A from Zauderer et al. (2013c) and van der Horst et al. (2015), and X-ray afterglow observations from *Swift*. GRB 111215A has previously been determined to be a dark burst through the $\beta_{\text{OX}} > -0.5$ criterion (Jakobsson et al. 2004) in Zauderer et al. (2013c). We gather host galaxy observations of GRB 111215A from van der Horst et al. (2015), and assume a redshift of $z = 2.012$ (van der Horst et al. 2015; Chrimes et al. 2019).

A.6.3. GRB 160509A

The radio, optical, and X-ray afterglow of GRB 160509A has previously been modeled with our modeling framework in Laskar et al. (2016), and we utilize the afterglow parameters within for our discussion (Section 5). The optical afterglow of GRB 160509A was heavily obscured, with a line-of-sight extinction of $A_{V,\text{GRB}} \approx 3.4$ mag, indicating it is likely a dark burst. Using the optical afterglow detections in r' -band at $\delta t \approx 0.25$ days (Laskar et al. 2016), we calculate $\beta_{\text{OX}} \approx 0.03$, meeting the darkness criterion of Jakobsson et al. (2004), and classifying GRB 160509A as a dark burst. Additionally, we find $\beta_{\text{X}} = -1.0 \pm 0.1$, leading to $\beta_{\text{OX}} - \beta_{\text{X}} \approx 0.98$. Thus, GRB 160509A is also classified as a dark burst according to the van der Horst et al. (2009) criterion.

The host galaxy of GRB 160509A was previously observed with *HST*/WFC3 in the F110W and F160W filters on 2017 July 5 (PI: Kangas) (Kangas et al. 2020). We retrieved, aligned, and drizzled the individual exposures for each band using the *HST* reduction pipeline `hst123` (Kilpatrick et al. 2022; Kilpatrick 2021). We also included a sky subtraction step as part of `astrodrizzle` (Hack et al. 2021) to remove large-scale background emission near the host galaxy. Using an elliptical aperture and the tabulated *HST* zeropoints, we calculated the F110W and F160W brightness of the host galaxy (Table A3 and Figure 1).

The host galaxy is also clearly detected in *Spitzer*/IRAC 3.6 μm observations taken on 2017 Nov 05 (PI: Perley). We downloaded and reduced the individual basic calibrated data frames (i.e., `cbcd`) using `photpipe` (Rest et al. 2005; Kilpatrick et al. 2018), including alignment, flux calibration, and optimal stacking to a pixel scale of $0.3''/\text{pix}$. We performed final PSF

photometry in the stacked frames using a custom version of `DoPhot` (Schechter et al. 1993). The host galaxy appears point-like in the stacked IRAC frames and is clearly separated from a nearby galaxy of similar brightness seen in the *HST* frames (Figure 1). Therefore, we use the `DoPhot` photometry calibrated using the appropriate warm *Spitzer* sensitivity function for IRAC and obtain a magnitude of ≈ 19.6 mag at 3.6 μm (Table A3).

We supplement these host galaxy observations with the Keck/LRIS g' - and r' -band measurements taken at $\delta t \approx 28.2$ days, where afterglow modeling found the host galaxy to dominate the flux (Laskar et al. 2016; Table A3).

B. ALTERNATIVE MCMC AFTERGLOW MODELS

Here we present the alternative MCMC afterglow models for the bursts whose afterglow observations did not distinguish between a wind or ISM environment through preliminary analytical arguments (GRB 110709B, 130131A, and 140713A).

B.1. GRB 110709B

We present the best fit (highest likelihood) wind environment model for GRB 110709B in Figure B1 and list the model parameters as well as the summary statistics from the marginalized posterior density functions (medians and 68% credible intervals) in Table 2 in Table A4.

Our best fit wind model for GRB 110709B finds a later $t_{\text{jet}} \approx 2.4$ days compared to our ISM model (Section 3.1.2). While the wind model better fits the X-ray light curve at $\delta t \gtrsim 5$ days, the marginal statistical preference for the ISM model is a result of the ISM model better matching the X-ray light curve at $\delta t \lesssim 5$ days, where the majority of the X-ray data exist. The best fit parameters for our wind model are the same as Kangas & Fruchter (2021) within 2σ , though our E_{K} and A_* are orders of magnitude different than those found by Zauderer et al. (2013c), likely due to the inclusion of IC effects in our model. Our best fit wind model requires $A_{V,\text{GRB}} \gtrsim 5.01$ mag to match the GROND optical/NIR afterglow upper limits.

B.2. GRB 130131A

We present the best fit wind environment for GRB 130131A model in Figure B2 and list the model parameters as well as the summary statistics from the marginalized posterior density functions (medians and 68% credible intervals) in Table A4.

Our ISM model of GRB 130131A finds an earlier jet break time of $t_{\text{jet}} \approx 0.8$ days compared to our wind model. As a consequence, while the radio afterglow of GRB 130131A is better fit by the ISM model, the X-ray light curve is under-predicted by the ISM model at

Table A4. Forward Shock Parameters

GRB	110709B	130131A	140713A
Env.	Wind	ISM	ISM
p	2.01	2.67	2.02
	$2.02^{+0.01}_{-0.01}$	$2.45^{+0.15}_{-0.11}$	$2.02^{+0.01}_{-0.01}$
E_K (10^{52} erg)	2.91×10^{-2}	1.02×10^{-1}	8.75×10^{-2}
	$4.33^{+3.17}_{-1.64} \times 10^{-2}$	$5.74^{+3.32}_{-3.28} \times 10^{-2}$	$9.19^{+1.37}_{-1.05} \times 10^{-2}$
A_*/n_0 ($-/\text{cm}^{-3}$)	1.45×10^{-2}	7.83×10^{-1}	1.91×10^0
	$2.65^{+2.46}_{-1.25} \times 10^{-2}$	$1.29^{+0.82}_{-0.59} \times 10^0$	$2.24^{+0.79}_{-0.49} \times 10^0$
ϵ_e	4.77×10^{-1}	4.64×10^{-1}	1.04×10^{-1}
	$3.75^{+1.78}_{-1.21} \times 10^{-1}$	$5.49^{+2.12}_{-1.7} \times 10^{-1}$	$8.81^{+4.03}_{-2.62} \times 10^{-2}$
ϵ_B	1.66×10^{-1}	1.33×10^{-5}	5.57×10^{-1}
	$4.0^{+14.26}_{-3.27} \times 10^{-2}$	$5.55^{+52.57}_{-3.97} \times 10^{-5}$	$4.4^{+2.28}_{-1.69} \times 10^{-1}$
t_{jet} (day)	2.38	0.79	9.51
	$2.44^{+0.21}_{-0.19}$	$0.86^{+0.24}_{-0.18}$	$9.4^{+0.71}_{-0.71}$
θ_{jet} (deg)	1.02	3.65	17.25
	$1.14^{+0.13}_{-0.12}$	$4.67^{+0.67}_{-0.62}$	$17.49^{+0.52}_{-0.48}$
$A_{V,\text{GRB}}$ (mag)	$\gtrsim 5.0$	≈ 2.4	$\gtrsim 3.1$
	$\gtrsim 5.1^a$	$2.3^{+0.1}_{-0.1}$	$\gtrsim 3.1^a$

NOTE— The top row for each parameter corresponds to the best fit forward shock value from our MCMC modeling. The bottom row for each parameter corresponds to the summary statistics from the marginalized posterior density functions (medians and 68% credible intervals)

^a $A_{V,\text{GRB}}$ value from afterglow model using median values

$\delta t \gtrsim 1$ day, resulting in the statistical preference for the wind model of GRB 130131A. Our ISM model finds that the extinction required to match the optical and NIR observations is $A_{V,\text{GRB}} \approx 2.41$ mag.

B.3. GRB 140713A

We present the best fit ISM environment model for GRB 140713A in Figure B3 and list the model parameters as well as the summary statistics from the marginalized posterior density functions (medians and 68% credible intervals) in Table 2 in Table A4.

Similar to the wind environment model (Section 3.5.2), the X-ray light curve for the ISM model of GRB 140713A is under-predicted at $\delta t \gtrsim 0.7$ days. While the K_u -band observations are better fit by the ISM model, the significant statistical preference for the wind model is attributed to the better fit C-band and 3mm observations light curves. Our ISM model for GRB 140713A requires $A_{V,\text{GRB}} \gtrsim 3.12$ mag necessary

to match the optical limits. This limit is the same as that derived by Higgins et al. (2019) for an SMC-like galactic extinction model.

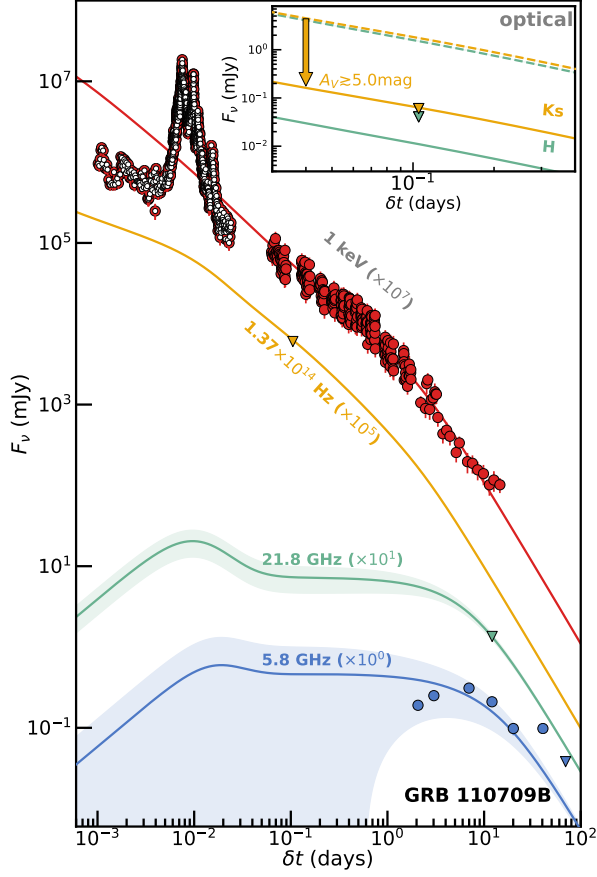


Figure B1. X-ray, optical, radio afterglow light curves of GRB 110709B, together with the best-fit forward shock model in an wind environment (lines). Circles represent literature data (Zauderer et al. 2013c), and triangles represent 3σ upper limits. Open symbols indicate data that are not included in the fit, and shaded regions represent variability due to scintillation. The inset shows the model K_s -band and H -band light curves (solid lines) as well as the non-extinguished models (dashed lines), indicating $A_{V,GRB} \gtrsim 5.0$ mag to explain the upper limits.

REFERENCES

- Alam, S., Albareti, F. D., Allende Prieto, C., et al. 2015, *ApJS*, 219, 12
- Alexander, K. D., Laskar, T., Berger, E., et al. 2017, *ApJ*, 848, 69
- Anderson, G. E., Fender, R. P., Staley, T. D., & van der Horst, A. J. 2014, GRB Coordinates Network, 16603, 1
- Anderson, G. E., Staley, T. D., van der Horst, A. J., et al. 2018, *MNRAS*, 473, 1512
- Balázs, L. G., Bagoly, Z., Horváth, I., Mészáros, A., & Mészáros, P. 2004, *Baltic Astronomy*, 13, 207
- Beardmore, A. P., Evans, P. A., Goad, M. R., & Osborne, J. P. 2014, GRB Coordinates Network, 16585, 1
- Berger, E., Kulkarni, S. R., Bloom, J. S., et al. 2002, *ApJ*, 581, 981
- Bertin, E., & Arnouts, S. 1996, *A&AS*, 117, 393
- Blain, A. W., & Natarajan, P. 2000, *MNRAS*, 312, L35
- Blanton, M. R., & Roweis, S. 2007, *AJ*, 133, 734
- Bloom, J. S., Kulkarni, S. R., & Djorgovski, S. G. 2002, *AJ*, 123, 1111

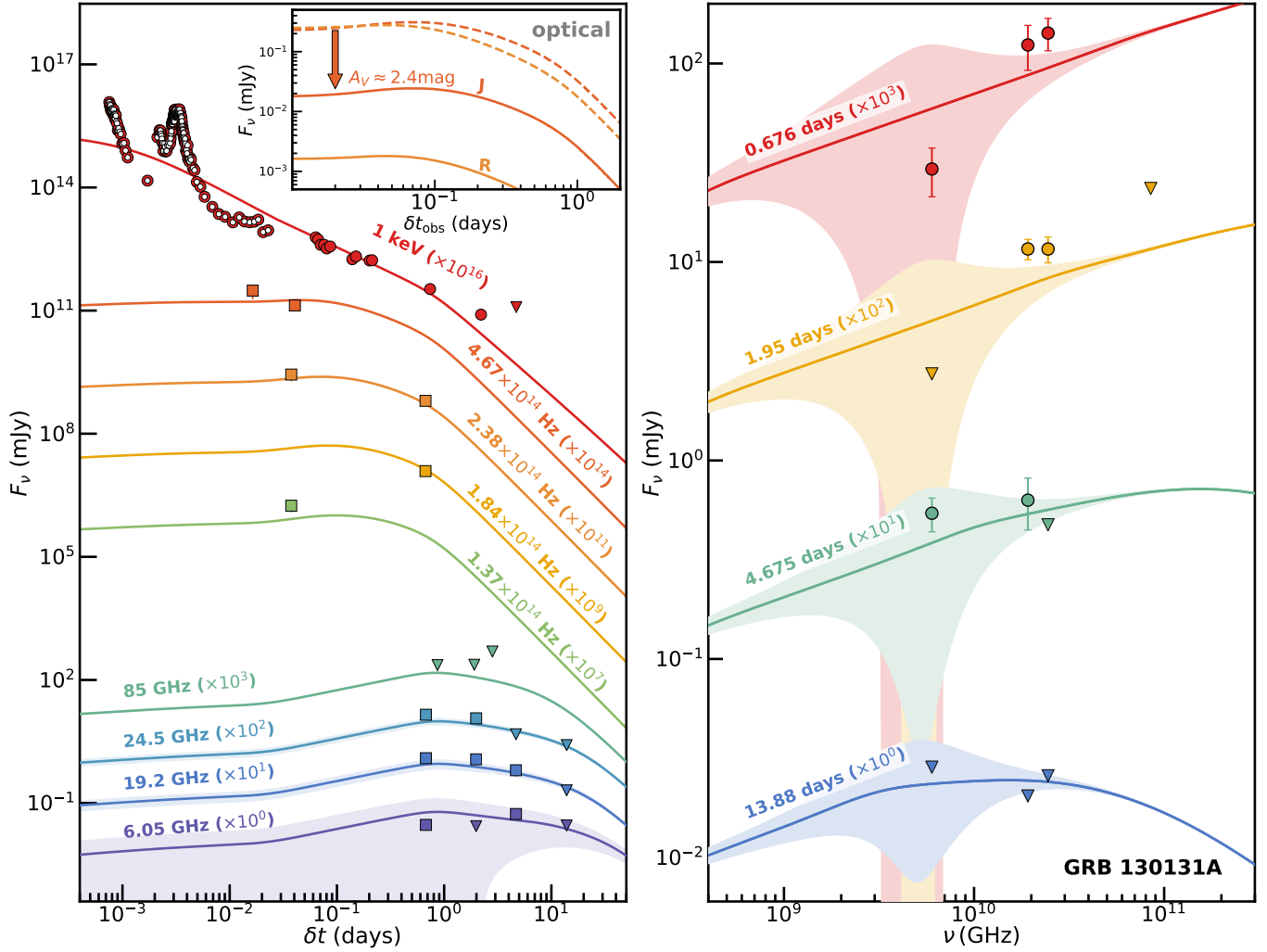


Figure B2. *Left:* X-ray, optical, millimeter and radio afterglow light curves of GRB 130131A, together with the best-fit forward shock model in an ISM environment (lines). Squares represent data newly reported here, and triangles represent 3σ upper limits. Open symbols indicate data that are not included in the fit, and shaded regions represent variability due to scintillation. The inset shows the model J - and R -band light curves (solid lines) as well as the non-extinguished models (dashed lines), indicating $A_{V,GRB} \approx 2.4$ mag to explain the detections. *Right:* Radio and millimeter spectral energy distributions (SEDs) of the afterglow of GRB 130131A from $\delta t \approx 0.7$ -13.9 days, together with the best-fit forward shock model (lines).

Burrows, D. N., Falcone, A., Chincarini, G., et al. 2007, *Philosophical Transactions of the Royal Society of London Series A*, 365, 1213
 Butler, N., Watson, A. M., Kutryev, A., et al. 2013, *GRB Coordinates Network*, 14831, 1
 Calura, F., Pozzi, F., Cresci, G., et al. 2017, *MNRAS*, 465, 54
 Calzetti, D., Armus, L., Bohlin, R. C., et al. 2000, *ApJ*, 533, 682
 Cano, Z., Malesani, D., Nielsen, M., & Planck, M. 2014, *GRB Coordinates Network*, 16587, 1
 Cardelli, J. A., Clayton, G. C., & Mathis, J. S. 1989, *ApJ*, 345, 245

Carilli, C. L., McKinnon, M., Ott, J., et al. 2015, arXiv e-prints, arXiv:1510.06438
 Casali, M., Adamson, A., Alves de Oliveira, C., et al. 2007, *A&A*, 467, 777
 Castro-Tirado, A. J., Jeong, S., Gorosabel, J., & Reverte, D. 2014, *GRB Coordinates Network*, 16602, 1
 Castro-Tirado, A. J., Bremer, M., McBreen, S., et al. 2007, *A&A*, 475, 101
 Castro-Tirado, A. J., Sanchez-Ramirez, R., Gorosabel, J., et al. 2013, *GRB Coordinates Network*, 14796, 1
 Cenko, S. B., Kelemen, J., Harrison, F. A., et al. 2009, *ApJ*, 693, 1484
 Cenko, S. B., Frail, D. A., Harrison, F. A., et al. 2010, *ApJ*, 711, 641

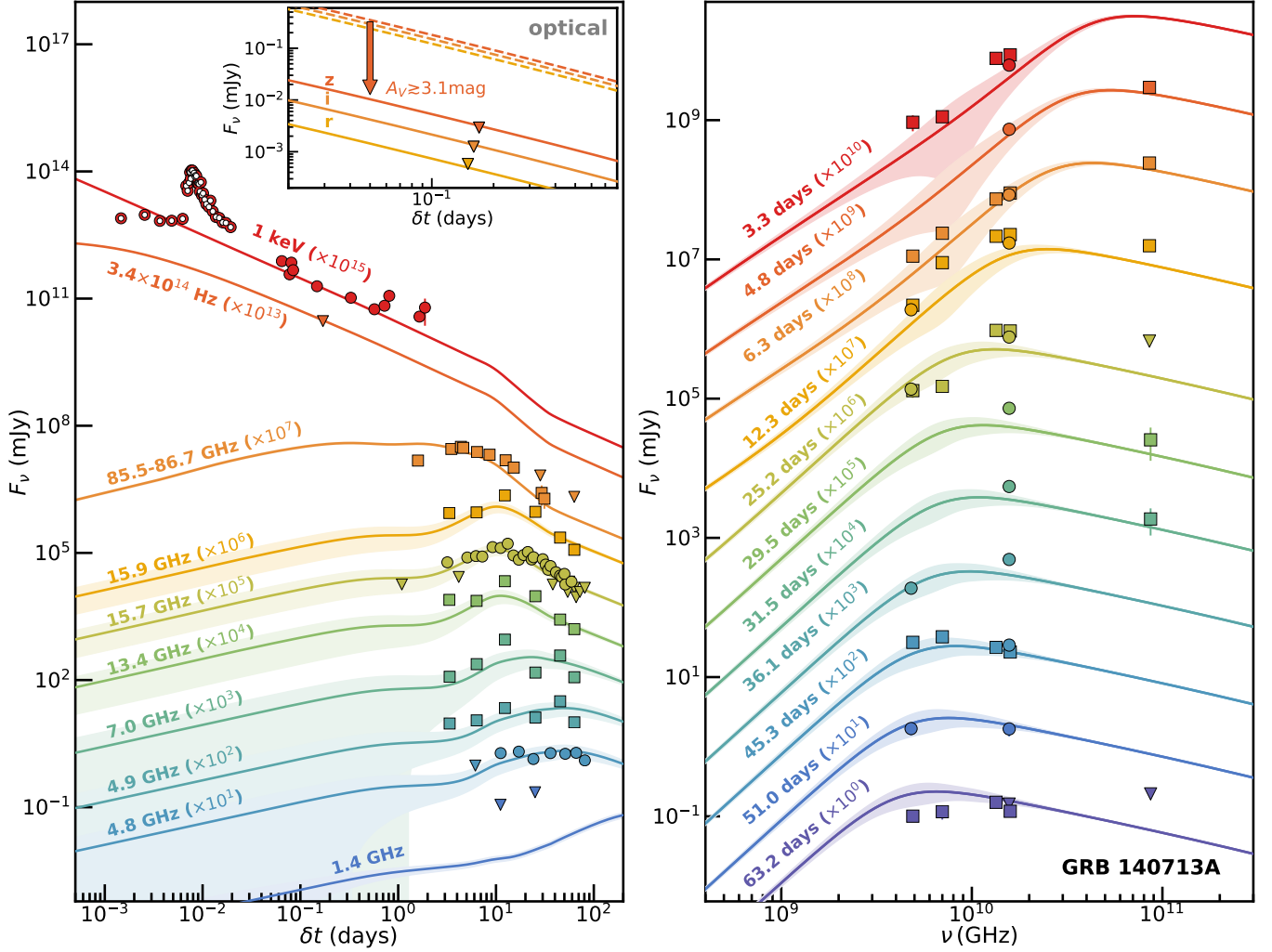


Figure B3. *Left:* X-ray, optical, millimeter and radio afterglow light curves of GRB 140713A, together with the best-fit forward shock model in an ISM environment (lines). Squares represent data newly reported here, circles represent literature data (Higgins et al. (2019)), and triangles represent 3σ upper limits. Open symbols indicate data that are not included in the fit, and shaded regions represent variability due to scintillation. The inset shows the model r -, i -, and z -band light curves (solid lines) as well as the non-extinguished models (dashed lines), indicating $A_{V,GRB} \gtrsim 3.1$ mag to explain the upper limits. *Right:* Radio and millimeter spectral energy distributions (SEDs) of the afterglow of GRB 140713A from $\delta t \approx 3.0$ -31.5 days, together with the best-fit forward shock model (lines).

— 2011, ApJ, 732, 29

Chabrier, G. 2003, PASP, 115, 763

Chambers, K. C., Magnier, E. A., Metcalfe, N., et al. 2016, ArXiv e-prints, arXiv:1612.05560

Chandra, P., & Frail, D. A. 2012, ApJ, 746, 156

Chandra, P., & Nayana, A. J. 2014a, GRB Coordinates Network, 16641, 1

— 2014b, GRB Coordinates Network, 16641, 1

Chandra, P., Cenko, S. B., Frail, D. A., et al. 2008, ApJ, 683, 924

Chevalier, R. A., & Li, Z.-Y. 2000, ApJ, 536, 195

Chornock, R., Berger, E., Fox, D. B., et al. 2013a, ApJ, 774, 26

Chornock, R., Fong, W., & Berger, E. 2013b, GRB Coordinates Network, 15637, 1

Chrimes, A. A., Levan, A. J., Stanway, E. R., et al. 2019, MNRAS, 486, 3105

Christensen, L., Hjorth, J., & Gorosabel, J. 2004, A&A, 425, 913

Conroy, C., & Gunn, J. E. 2010, ApJ, 712, 833

Conroy, C., Gunn, J. E., & White, M. 2009, ApJ, 699, 486

Covino, S., Melandri, A., Salvaterra, R., et al. 2013, MNRAS, 432, 1231

Cucchiara, A., Levan, A. J., Fox, D. B., et al. 2011, ApJ, 736, 7

- Cummings, J. R., Baumgartner, W. H., Gehrels, N., et al. 2013, GRB Coordinates Network, 14828, 1
- Djorgovski, S. G., Kulkarni, S. R., Bloom, J. S., et al. 1998, *ApJL*, 508, L17
- Eftekhari, T., Margalit, B., Omand, C. M. B., et al. 2021, *ApJ*, 912, 21
- Evans, P. A., Goad, M. R., Osborne, J. P., & Beardmore, A. P. 2013, GRB Coordinates Network, 14160, 1
- Evans, P. A., Beardmore, A. P., Page, K. L., et al. 2009, *MNRAS*, 397, 1177
- Fong, W., Berger, E., Metzger, B. D., et al. 2014, *ApJ*, 780, 118
- Frail, D. A., Kulkarni, S. R., Nicastro, L., Feroci, M., & Taylor, G. B. 1997, *Nature*, 389, 261
- Frail, D. A., Soderberg, A. M., Kulkarni, S. R., et al. 2005, *ApJ*, 619, 994
- Fynbo, J. P. U., Jakobsson, P., Prochaska, J. X., et al. 2009, *ApJS*, 185, 526
- Gallazzi, A., Charlot, S., Brinchmann, J., White, S. D. M., & Tremonti, C. A. 2005, *MNRAS*, 362, 41
- Gatkine, P., Vogel, S., & Veilleux, S. 2020, *ApJ*, 897, 9
- Gehrels, N., Barthelmy, S. D., Burrows, D. N., et al. 2008, *ApJ*, 689, 1161
- Granot, J., & Sari, R. 2002, *ApJ*, 568, 820
- Greiner, J., Krühler, T., Klose, S., et al. 2011, *A&A*, 526, A30
- Greiner, J., Michałowski, M. J., Klose, S., et al. 2016, *A&A*, 593, A17
- Groot, P. J., Galama, T. J., van Paradijs, J., et al. 1998, *ApJL*, 493, L27
- Grupe, D., Barlow, B. N., Barthelmy, S. D., et al. 2013, GRB Coordinates Network, 14156, 1
- Hack, W. J., Cara, M., Sosey, M., et al. 2021, *spacetelescope/drizzlepac: Drizzlepac v3.3.0, v.3.3.0*, Zenodo, doi:10.5281/zenodo.5534751
- Haislip, J. B., Nysewander, M. C., Reichart, D. E., et al. 2006, *Nature*, 440, 181
- Hamly, N. C., Collins, R. S., Cross, N. J. G., et al. 2008, *MNRAS*, 384, 637
- Higgins, A. B., van der Horst, A. J., Starling, R. L. C., et al. 2019, *MNRAS*, 484, 5245
- Hjorth, J., Sollerman, J., Møller, P., et al. 2003, *Nature*, 423, 847
- Horesh, A., Cenko, S. B., Perley, D. A., et al. 2015, *ApJ*, 812, 86
- Hunt, L. K., Palazzi, E., Michałowski, M. J., et al. 2014, *A&A*, 565, A112
- Hunter, J. D. 2007, *Computing in Science Engineering*, 9, 90
- Jakobsson, P., Hjorth, J., Fynbo, J. P. U., et al. 2004, *ApJL*, 617, L21
- Jakobsson, P., Frail, D. A., Fox, D. B., et al. 2005, *ApJ*, 629, 45
- Japelj, J., Vergani, S. D., Salvaterra, R., et al. 2016, *A&A*, 590, A129
- Jeong, S., Castro-Tirado, A. J., Bremer, M., et al. 2014, *A&A*, 569, A93
- Kangas, T., & Fruchter, A. S. 2021, *ApJ*, 911, 14
- Kangas, T., Fruchter, A. S., Cenko, S. B., et al. 2020, *ApJ*, 894, 43
- Kann, D. A., Klose, S., & Zeh, A. 2006, *ApJ*, 641, 993
- Kann, D. A., Klose, S., Zhang, B., et al. 2010, *ApJ*, 720, 1513
- Kilpatrick, C. D. 2021, *charliekilpatrick/hst123: hst123, v.v1.0.0*, Zenodo, doi:10.5281/zenodo.5573941
- Kilpatrick, C. D., Foley, R. J., Drout, M. R., et al. 2018, *MNRAS*, 473, 4805
- Kilpatrick, C. D., Fong, W.-f., Blanchard, P. K., et al. 2022, *ApJ*, 926, 49
- Krühler, T., Greiner, J., Schady, P., et al. 2011, *A&A*, 534, A108
- Krühler, T., Malesani, D., Milvang-Jensen, B., et al. 2012, *ApJ*, 758, 46
- Krühler, T., Malesani, D., Fynbo, J. P. U., et al. 2015, *A&A*, 581, A125
- Lacy, M., Baum, S. A., Chandler, C. J., et al. 2020, *PASP*, 132, 035001
- Laskar, T., Berger, E., Chornock, R., et al. 2018a, *ApJ*, 858, 65
- Laskar, T., Berger, E., Margutti, R., et al. 2015, *ApJ*, 814, 1
- Laskar, T., Zauderer, A., & Berger, E. 2013a, GRB Coordinates Network, 14817, 1
- Laskar, T., Zauderer, B. A., & Berger, E. 2013b, GRB Coordinates Network, 14171, 1
- Laskar, T., Berger, E., Zauderer, B. A., et al. 2013c, *ApJ*, 776, 119
- Laskar, T., Berger, E., Tanvir, N., et al. 2014, *ApJ*, 781, 1
- Laskar, T., Alexander, K. D., Berger, E., et al. 2016, *ApJ*, 833, 88
- Laskar, T., Berger, E., Margutti, R., et al. 2018b, *ApJ*, 859, 134
- Laskar, T., Alexander, K. D., Berger, E., et al. 2018c, *ApJ*, 862, 94
- Laskar, T., van Eerten, H., Schady, P., et al. 2019, *ApJ*, 884, 121
- Leibler, C. N., & Berger, E. 2010, *ApJ*, 725, 1202
- Leja, J., Johnson, B. D., Conroy, C., Dokkum, P. G. v., & Byler, N. 2017, *The Astrophysical Journal*, 837, 170
- Liang, S. L., & Li, A. 2010, *ApJ*, 710, 648

- Lien, A., Sakamoto, T., Barthelmy, S. D., et al. 2016, *ApJ*, 829, 7
- Littlejohns, O. M., Butler, N. R., Cucchiara, A., et al. 2015, *MNRAS*, 449, 2919
- Longo, F., Bissaldi, E., Bregeon, J., et al. 2016, *GRB Coordinates Network*, 19403, 1
- MacFadyen, A. I., & Woosley, S. E. 1999, *ApJ*, 524, 262
- Mangano, V., Barthelmy, S. D., Chester, M. M., et al. 2014, *GRB Coordinates Network*, 16581, 1
- Margutti, R., Guidorzi, C., Chincarini, G., et al. 2010, *MNRAS*, 406, 2149
- Margutti, R., Guidorzi, C., Lazzati, D., et al. 2015, *ApJ*, 805, 159
- Mckinney, W. 2010, *Proceedings of the 9th Python in Science Conference*
- McMullin, J. P., Waters, B., Schiebel, D., Young, W., & Golap, K. 2007, in *Astronomical Society of the Pacific Conference Series*, Vol. 376, *Astronomical Data Analysis Software and Systems XVI*, ed. R. A. Shaw, F. Hill, & D. J. Bell, 127
- Melandri, A., Sbarufatti, B., D'Avanzo, P., et al. 2012, *MNRAS*, 421, 1265
- Nakar, E., Ando, S., & Sari, R. 2009, *ApJ*, 703, 675
- Nousek, J. A., Kouveliotou, C., Grupe, D., et al. 2006, *ApJ*, 642, 389
- Nugent, A. E., Fong, W.-f., Dong, Y., et al. 2020, *arXiv e-prints*, arXiv:2007.10372
- Oates, S. R., Baumgartner, W. H., Burrows, D. N., et al. 2013, *GRB Coordinates Network*, 14411, 1
- Osborne, J. A., Bagheri, F., & Shahmoradi, A. 2021, *MNRAS*, 502, 5622
- Page, M. J., Barthelmy, S. D., Gehrels, N., et al. 2013, *GRB Coordinates Network*, 15627, 1
- Palmerio, J. T., Vergani, S. D., Salvaterra, R., et al. 2019, *A&A*, 623, A26
- Panaitescu, A., & Kumar, P. 2000, *ApJ*, 543, 66
- . 2002, *ApJ*, 571, 779
- Perley, D. A. 2013, *GRB Coordinates Network*, 15638, 1
- Perley, D. A., & Cenko, S. B. 2013, *GRB Coordinates Network*, 14830, 1
- Perley, D. A., Hjorth, J., Tanvir, N. R., & Perley, R. A. 2017, *MNRAS*, 465, 970
- Perley, D. A., & Perley, R. A. 2013, *ApJ*, 778, 172
- Perley, D. A., Levan, A. J., Tanvir, N. R., et al. 2013, *ApJ*, 778, 128
- Perley, D. A., Perley, R. A., Hjorth, J., et al. 2015, *ApJ*, 801, 102
- Perley, D. A., Krühler, T., Schulze, S., et al. 2016a, *ApJ*, 817, 7
- Perley, D. A., Tanvir, N. R., Hjorth, J., et al. 2016b, *ApJ*, 817, 8
- Perley, R. A., Chandler, C. J., Butler, B. J., & Wrobel, J. M. 2011, *ApJL*, 739, L1
- Piranomonte, S., Japelj, J., Vergani, S. D., et al. 2015, *MNRAS*, 452, 3293
- Price, P. A., Berger, E., Reichart, D. E., et al. 2002, *ApJL*, 572, L51
- Price, S. H., Kriek, M., Brammer, G. B., et al. 2014, *ApJ*, 788, 86
- Racusin, J. L., Karpov, S. V., Sokolowski, M., et al. 2008, *Nature*, 455, 183
- Ramirez-Ruiz, E., Trentham, N., & Blain, A. W. 2002, *MNRAS*, 329, 465
- Rest, A., Stubbs, C., Becker, A. C., et al. 2005, *ApJ*, 634, 1103
- Rhoads, J. E. 1999, *ApJ*, 525, 737
- Rickett, B. J. 1990, *ARA&A*, 28, 561
- Rol, E., van der Horst, A., Wiersema, K., et al. 2007, *ApJ*, 669, 1098
- Rossi, A., Klose, S., Ferrero, P., et al. 2012, *A&A*, 545, A77
- Salvaterra, R., Della Valle, M., Campana, S., et al. 2009, *Nature*, 461, 1258
- Salvaterra, R., Campana, S., Vergani, S. D., et al. 2012, *ApJ*, 749, 68
- Santini, P., Maiolino, R., Magnelli, B., et al. 2014, *A&A*, 562, A30
- Sari, R., & Esin, A. A. 2001, *ApJ*, 548, 787
- Sari, R., Piran, T., & Halpern, J. P. 1999, *ApJL*, 519, L17
- Sari, R., Piran, T., & Narayan, R. 1998, *ApJL*, 497, L17
- Sault, R. J., Teuben, P. J., & Wright, M. C. H. 1995, in *Astronomical Society of the Pacific Conference Series*, Vol. 77, *Astronomical Data Analysis Software and Systems IV*, ed. R. A. Shaw, H. E. Payne, & J. J. E. Hayes, 433
- Savaglio, S., Glazebrook, K., & Le Borgne, D. 2009, *ApJ*, 691, 182
- Schady, P., Savaglio, S., Müller, T., et al. 2014, *A&A*, 570, A52
- Schechter, P. L., Mateo, M., & Saha, A. 1993, *PASP*, 105, 1342
- Schlaflly, E. F., & Finkbeiner, D. P. 2011, *ApJ*, 737, 103
- Schultz, G. V., & Wiemer, W. 1975, *A&A*, 43, 133
- Selsing, J., Malesani, D., Goldoni, P., et al. 2019, *A&A*, 623, A92
- Smolčić, V., Delvecchio, I., Zamorani, G., et al. 2017, *A&A*, 602, A2
- Speagle, J. S. 2020, *MNRAS*, 493, 3132
- Stanway, E. R., Levan, A. J., & Davies, L. J. M. 2014, *MNRAS*, 444, 2133

- Tanvir, N. R., Levan, A. J., & Wold, T. 2013a, GRB Coordinates Network, 14157, 1
- . 2013b, GRB Coordinates Network, 14175, 1
- Tanvir, N. R., Fox, D. B., Levan, A. J., et al. 2009, *Nature*, 461, 1254
- Tanvir, N. R., Laskar, T., Levan, A. J., et al. 2018, *ApJ*, 865, 107
- Tody, D. 1986, in *Proc. SPIE*, Vol. 627, Instrumentation in astronomy VI, ed. D. L. Crawford, 733
- Tody, D. 1993, in *Astronomical Society of the Pacific Conference Series*, Vol. 52, Astronomical Data Analysis Software and Systems II, ed. R. J. Hanisch, R. J. V. Brissenden, & J. Barnes, 173
- Tonry, J. L., Stubbs, C. W., Lykke, K. R., et al. 2012, *ApJ*, 750, 99
- van der Horst, A. J., Kouveliotou, C., Gehrels, N., et al. 2009, *ApJ*, 699, 1087
- van der Horst, A. J., Levan, A. J., Pooley, G. G., et al. 2015, *MNRAS*, 446, 4116
- van der Walt, S., Colbert, S. C., & Varoquaux, G. 2011, *Computing in Science Engineering*, 13, 22
- Veres, P., Corsi, A., Frail, D. A., Cenko, S. B., & Perley, D. A. 2015, *ApJ*, 810, 31
- Vergani, S. D., Salvaterra, R., Japelj, J., et al. 2015, *A&A*, 581, A102
- Virtanen, P., Gommers, R., Oliphant, T. E., et al. 2020, *Nature Methods*, 17, 261
- Volnova, A., Korobtsev, I., Klunko, E., & Pozanenko, A. 2013, GRB Coordinates Network, 14182, 1
- Williams, P. K. G., Clavel, M., Newton, E., & Ryzhkov, D. 2017a, *pwkit: Astronomical utilities in Python*, Astrophysics Source Code Library, , ascl:1704.001
- Williams, P. K. G., Clavel, M., Newton, E., & Ryzhkov, D. 2017b, *pwkit: Astronomical utilities in Python*, Astrophysics Source Code Library, record ascl:1704.001, , ascl:1704.001
- Woolley, S. E., & Bloom, J. S. 2006, *ARA&A*, 44, 507
- Yost, S. A., Harrison, F. A., Sari, R., & Frail, D. A. 2003, *ApJ*, 597, 459
- Zafar, T., Watson, D., Fynbo, J. P. U., et al. 2011, *A&A*, 532, A143
- Zauderer, A., & Berger, E. 2012, GRB Coordinates Network, 12895, 1
- Zauderer, B. A., & Berger, E. 2013, GRB Coordinates Network, 14444, 1
- Zauderer, B. A., Berger, E., & Laskar, T. 2013a, GRB Coordinates Network, 14172, 1
- Zauderer, B. A., Fong, W., & Berger, E. 2014, GRB Coordinates Network, 16593, 1
- Zauderer, B. A., Fong, W., Berger, E., & Laskar, T. 2013b, GRB Coordinates Network, 14863, 1
- Zauderer, B. A., Berger, E., Margutti, R., et al. 2013c, *ApJ*, 767, 161
- Zhang, B., Fan, Y. Z., Dyks, J., et al. 2006, *ApJ*, 642, 354
- Zhao, X.-H., Mao, J., & Bai, J.-M. 2013, GRB Coordinates Network, 14423, 1